Summer 2015

The radiation physics, mitigation approaches and design guidelines of high-speed connectors and cables analyzed with numerical modeling, analytical formulation and measurements

Jing Li

Department: Electrical and Computer Engineering

THE RADIATION PHYSICS, MITIGATION APPROACHES AND DESIGN GUIDELINES OF HIGH-SPEED CONNECTORS AND CABLES ANALYZED WITH NUMERICAL MODELING, ANALYTICAL FORMULATION AND MEASUREMENTS

by

JING LI

A DISSERTATION

Presented to the Faculty of the Graduate School of the

MISSOURI UNIVERSITY OF SCIENCE AND TECHNOLOGY

In Partial Fulfillment of the Requirements for the Degree

DOCTOR OF PHILOSOPHY

in

ELECTRICAL ENGINEERING

2015

Approved by:

Dr. Jun Fan, Advisor
Dr. James L. Drewniak
Dr. Alpesh Bhobe
Dr. Daryl Beetner
Dr. David J. Pommerenke
Dr. Matt Okeefe

PUBLICATION DISSERTATION OPTION

This dissertation consists of the following three papers, formatted in the style used by the Missouri University of Science and Technology, listed as follows:

Paper 1, Jing Li, Xiao Li, Sukhjinder Toor, Hongmei Fan, Alpesh Bhobe, Jun Fan, James Drewniak, "EMI Coupling Paths and Mitigation in a Board-to-Board Connector," submitted to IEEE Trans. on EMC., 2014.

Paper 2, Jing Li, Jun Fan, "Radiation Physics and Design Guidelines of High-Speed Connectors," to be submitted to IEEE Trans. on EMC., 2015.

Paper 3, Jing Li, Yao-Jiang Zhang, Shenhui Jing, James L. Drewniak, Jun Fan, "EMI Reduction Evaluation for Absorbing Materials on Cables with a 2D Finite Element Approach," submitted to IEEE Trans. on EMC., 2015.

ABSTRACT

The dissertation is composed of three papers, which cover the radiation and mitigation of high-speed connectors and cables analyzed with full wave simulation, numerical modeling, analytical formulation and measurements.

In the first paper, the radiation from the optical cage connector in the frequency range of 4-28 GHz is analyzed with validated full-wave simulation model and analytical formulas. The radiation from the optical cage connector is suppressed with absorbing materials, and the coupling path in optical link is verified, together with the optical cage and module enclosure.

In the second paper, radiation from antenna-mode current and TL-mode current is briefly reviewed with backplane connector and optical cage connector. The radiation from the high-speed connector with TL-mode current is analyzed in detail. The possible radiation mechanisms are analyzed through Green's function method, steepest descent method, and EMC Studio method of moment (MoM). Design guidelines of high-speed connectors for EMI mitigation are proposed based on the analysis of radiation physics.

In the third paper, the 2D finite element method (2D FEM) is developed to analyze electromagnetic interference (EMI) reduction when magneto-dielectric absorbing materials are applied to cables, which is much less time- and memory-consuming compared to a 3D numerical simulation. To give insightful guidelines to the engineers who use absorbing materials as a mitigation approach to suppress the EMI from cables, cables with different absorbing materials, different diameters, lengths, and source impedances are analyzed with the developed 2D FEM.

ACKNOWLEDGMENTS

I would like to express my sincere gratitude to Dr. Jun Fan, my advisor, and Dr. Drewniak for their guidance and instruction on my research work, financial support to my study and direction for this dissertation during my pursuit of the PhD's degree. I learned not only academic knowledge from them, but also the rigorous attitude, good manners, and courage to face difficulties.

I would like to thank Dr. David J. Pommerenke, Dr. Victor Khilkevich and Dr. Daryl Beetner, for their teaching in my courses, discussions related to my research/projects and helpful suggestions on my thesis.

I would like to thank Dr. Alpesh Bhobe for his kind and strict mentoring during my one-year internship in Cisco. Not only did my time at Cisco inspire my dissertation study, it also helped me to develop my communication and team work skills.

I would like to thank Dr. Matt Okeefe for the helpful suggestions on my research.

I would also like to express my thanks to all the other faculty members and students in and out of the EMC lab for their team work and help in my coursework and research.

Finally, I would like to thank to my family for their endless love and endless support in my life.

TABLE OF CONTENTS

LIST OF ILLUSTRATIONS

PAPER III

LIST OF TABLES

1. INTRODUCTION

High-speed connectors are commonly used for transmitting signals between multiple printed circuit boards (PCB) in system level designs, and have been a major factor of radiated emission for systems up to the GHz range. Some board-to-board connectors have signal conductors with different lengths, e.g., edge-coupled PCB backplane connectors, while for optical cage connectors, the signal conductors are typically broad-side coupled, identical in length, and symmetric. The radiation from connectors with different lengths of signal traces has been the subject of previous studies, and the effect of skew compensation on mode conversion and radiation was discussed in many papers. The radiation from the connectors with the same length of the signal traces in the gigahertz range has not been analyzed fully.

As the speed of digital circuits increases to tens of Gbps, the frequency range of EMI problems goes up to tens of GHz. The radiation from high-speed PCB connectors with differential-mode signaling is widely used in digital electronic devices in order to establish a high-speed digital propagation with low-electromagnetic interference (EMI).

In this dissertation, the EMI physics of an optical cage connector (which has equal-length signal conductors) excited with differential mode signals is analyzed through full-wave simulation in the frequency range from 4 to 28GHz. Further, EMI mitigation approaches through a U-channel ground conductor connection, and absorbing material are demonstrated. When the optical cage connector is excited with differential mode signals, the radiation at high frequency is similar to the radiation from two signal conductors, which is equivalent to the radiation from a bent two-wire transmission line with TL-mode current. Despite numerous analytical, experimental, and theoretical works

that has been carried out on radiation from a bent two-wire transmission line, the radiation mechanism has yet to be fully understood. In this dissertation, the radiation physics of a two-wire transmission line is analyzed using the Green's function method, the steepest descent method and EMC Studio's method of moments (MoM) solver in paper 2, and design guidelines of high-speed connector for EMI mitigation are proposed based on the study of radiation physics.

The electromagnetic noise energy that can escape from the system equipment enclosure along cables attached to the system is another system-level EMI contributor. If the shielding of the cable is not good or there is mismatch at two ends of the cable, the currents that go down the cable as conduction currents and their "return" counterparts will radiate as displacement currents. Ferrite cores or flexible absorbing materials can be applied on cables to suppress common mode noise radiation. The radiation from a cable carrying a common mode current is equivalent to the radiation from a monopole antenna over a ground plane. Therefore, the estimation of EMI reduction on cables due to absorbing materials or ferrite cores is converted to the analysis of a monopole antenna with different coating materials. To mesh the thin absorbing materials or the small gap between ferrite cores and cables for the long cable geometry at frequencies up to 10 GHz, it is very time- and memory-consuming for the 3D FEM to evaluate the EMI reduction from the absorbing materials. Taking the advantage of the axially symmetric structure, a 2D FEM method is developed to calculate the radiated power reduction due to the coating materials around a cable in paper 3. To give insightful guidelines to the engineers who use absorbing materials as a mitigation approach to suppress the EMI from cables, cables

with different absorbing materials, different diameters, lengths, and source impedances are analyzed with the developed 2D FEM.

This dissertation consists of three papers. In paper 1, the radiation physics and mitigation approaches of optical cage connectors are analyzed from 4 to 28 GHz. In paper 2, the possible radiation mechanisms of the high-speed connectors with TL-mode current at high frequency are analyzed analytically, and design guidelines are proposed. In paper 3, the 2D FEM is developed to analyze EMI reduction when absorbing materials are applied to cables. The primary contributions of this dissertation include:

The radiation physics and the coupling paths of optical cage connectors (which has equal-length signal conductors) are analyzed from 4 to 28 GHz through full wave simulation (paper 1).

Mitigation approaches on optical cage connectors are demonstrated in both simulation and measurement (paper 1).

The radiation physics from the high-speed connector with TL-mode current is analyzed with Green's function method, steepest descent method, and EMC Studio's method of moments (MoM) solver (paper 2).

Design guidelines of high-speed connector for EMI mitigation are proposed (paper 2).

The radiation from right-angle bent two-wire transmission line with any type of current distribution can be calculated by summing up the radiated fields from all the discontinuities in the structure using steepest descent method, and the small reflection due to the discontinuities at bends does not need to be considered in the current distributions (paper 2).

2D FEM is developed to evaluate EMI reduction when absorbing materials applied to cables, which is less time- and memory-consuming compared to the 3D full wave solver (paper 3).

Design curves and guild lines are developed for the engineers who use absorbing materials as a mitigation approach to suppress the EMI from cables (paper 3).

PAPER

I. EMI Coupling Paths and Mitigation in a Board-to-Board Connector

Jing Li, *Student Member, IEEE,* Xiao Li, Sukhjinder Toor, Hongmei Fan,

Alpesh Bhobe, Jun Fan, *Senior Member, IEEE,* James Drewniak, *Fellow, IEEE*

Abstract— Cage connectors for optical sub-assembly I/O modules have been identified as one of the main coupling paths in an optical link at the front-end of switches and routers. In the study presented herein, the simulation model used to study EMI coupling physics and mitigation of the optical cage connector was corroborated by comparing the measured and simulated results for the total radiated power (TRP). Currents on the adjacent ground references to the differential signal conductors caused half-wave resonant peaks in the TRP response in the frequency range of 4-18 GHz. At frequencies from 18 to 28GHz, both full-wave simulation and analytical formulas indicate that the radiation results primarily from the currents on the signal traces. The radiation from the optical cage connector was suppressed with absorbing materials, and the coupling path was verified, together with the optical cage and module enclosure.

Index Terms—Optical cage connector, total radiated power, radiation mechanism, high frequency, absorbing material, EMI coupling path, mitigation

1. INTRODUCTION

Optical transceiver modules are commonly used in switches and routers, and there is potential to have significant electromagnetic interference (EMI) problems at their operation frequency and/or harmonics. Several papers have discussed EMI issues and solutions for optical transceiver modules [1]- [3]. In addition to these, the EMI coupling paths from the perspective of the entire optical link, including the optical cage connector, the connector housing/cage, the transceiver module, and the optical cable, have been addressed experimentally [4]. The optical cage connector has been identified as one of the major EM coupling paths, and it contributes to the leakage at the front of the system [4].

For a complex, high-speed system, printed circuit board (PCB) connectors are commonly used to transmit signals between multiple boards. Some board-to-board connectors have the signal traces with different lengths, e.g., edge-coupled PCB backplane connectors [5], while for optical cage connectors, the signal traces are typically broad-side coupled, identical in length, and symmetric. The radiation from connectors with different lengths of signal traces has been the subject of previous studies [6]-[11], and the effect of skew compensation on mode conversion and radiation was discussed in [12]-[14]. The radiation from the connectors with the same length of the signal traces in the gigahertz range has not been analyzed fully. The simplified connectors discussed in reference [15] have the same length of signal traces, but the analysis was still based on the signal-trace length mismatch due to the different trace lengths on the PCB connected to the connector. The fields from the currents on the differential signal traces are nearly canceling in the far field, however, when the frequency becomes high, the field cancelation lessens, as will be discussed in Section IV. References [15]-[16] also report the effect of different ground pin

configurations on mode conversion and radiation, and the best ground pin configuration was used in the connector structure in the study presented in this paper. However, the current on the ground pins still contributed to the radiation at the half-wavelength resonances of the ground conductor geometry. Adding a partial U-channel ground connection in the connector structure eliminated the resonances, as discussed in Section IV. The objective of the current study was to achieve an understanding of the radiation physics of optical cage connectors from 4 to 28GHz, and to quantify the coupling paths of an optical cage connector through full-wave simulation. Further, mitigation approaches through a U-channel ground conductor connection, and absorbing material are demonstrated.

The coupling paths proposed in the previous study are briefly outlined in Section II [4]. The optical cage connector structure is detailed in Section III, and the model corroboration through TRP measurement in a reverberation chamber is presented. The analysis of the EMI physics of an optical cage connector through full-wave simulation in the frequency range from 4 to 28GHz is presented in Section IV. Finally, EMI mitigation with absorbing material on the optical cage connector is demonstrated in Section V.

2. EMI COUPLING PATH DETERMINATION FOR OPTICAL LINKS

Two EMI coupling paths from the entire link from the connector to the host board through the optical sub-assembly and out the optical cable were proposed from the critical experiments detailed in [4], as shown in Fig. 1. In Fig. 1 (a), the leakage points for the monopole excitation (optical cable ferrule conductor) are the front slots of the module enclosure. When better contact existed between the optical sub-assembly (OSA) enclosure and the module enclosure, the antenna current coupled to the monopole antenna (Al ferrule in optical cable) decreased dramatically. Fig. 1 (b) illustrates the proposed coupling path for the optical cage connector. The leakage occurred primarily from the gap between the module enclosure and the cage. The shielding performance of the gasket between the module enclosure and the cage determines the leakage from the gap. Due to the deterioration of gasket performance at high frequencies, the EMI analysis of the optical cage connector is necessary for quantifying the coupling physics and identifying potential EMI mitigation approaches beyond shielding.

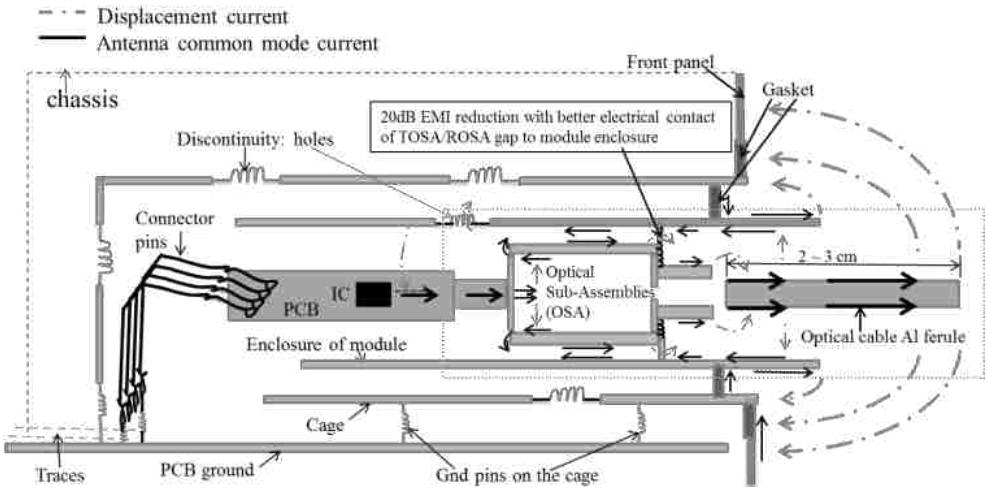

(a)

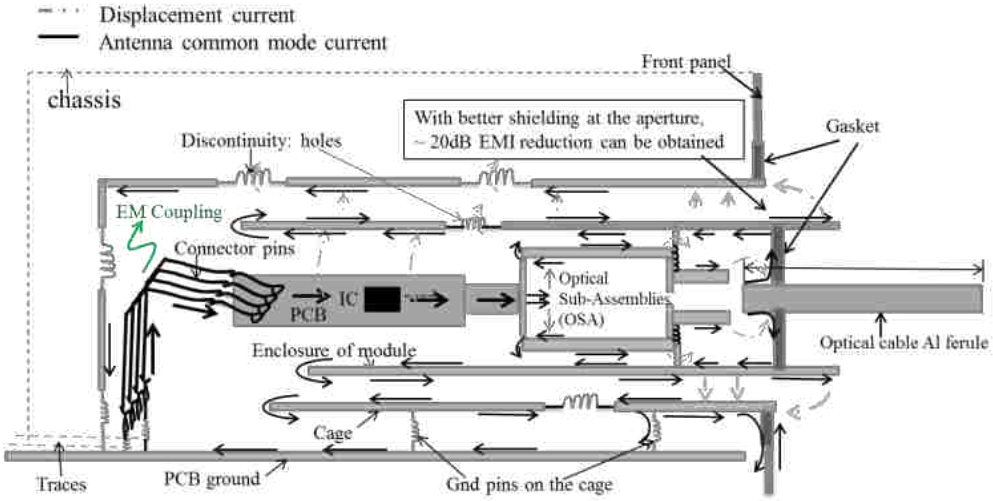

(b)

Fig. 1. Diagram of coupling paths. (a) Coupling path for monopole excitation. (b) Coupling path for optical cage connector.

3. OPTICAL CAGE CONNECTOR AND SIMULATION MODEL

3.1 Optical Cage Connector Structure

The optical cage connector was housed inside the back of the optical cage, as shown in Fig. 2. It connected the signal traces directly from the network ASIC or from the PHY (physical layer of the open system interconnect (OSI) model) on the host board line card to the traces on the PCB inside the optical module. Test boards were designed for the excitation and termination of the connector, as shown in Fig. 3. Simulation model in Fig. 3(a) was in CST Microwave Studio. The small board inserted into the connector was used to terminate the connector, mimicking the PCB inside the optical module, and was denoted the "module board". The layout of the pins on the top layer of module board, as shown in Fig. 3 (a), is the same as in a production version of the design. The board on which the connector was mounted was used for the excitation. The routing of test boards was stripline to allow top and bottom ground reference planes, edge via stitching to have a good enclosure for the PCB, and so as to not get PCB radiation artifacts. The connectors were 2.4mm, and back-drilling was used in the design for the board to work up to 30GHz. This board mimicked the line card with electrical signals on the traces, and it was termed the "host board". Basic design rules were considered in the simplified test boards for good signal transmission and minimal influence on TRP. The contribution of the different test board designs can be analyzed with the corroborated simulation model of the connector.

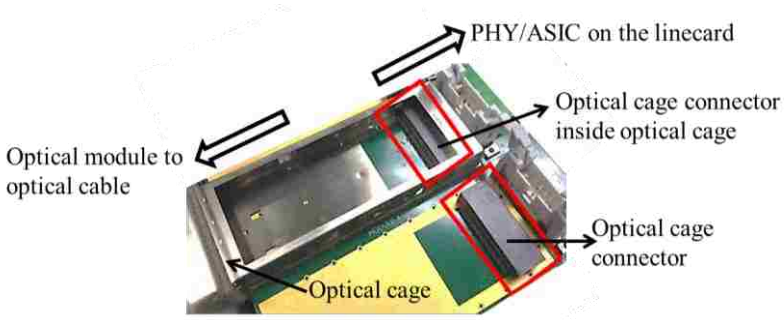

Fig. 2. Optical cage connector in the back of optical cage.

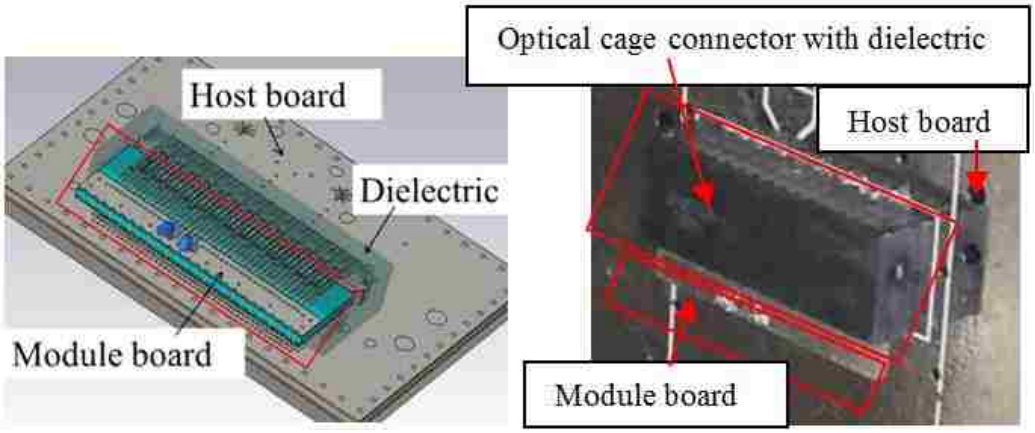

(a) (b)

Fig. 3. Optical cage connector with test boards. (a) Simulation model in CST Microwave Studio. (b) Test vehicle in the receiving side of reverberation chamber.

One pair of signal and ground reference pins of the optical cage connector is shown in Fig. 4. The two pins in the middle were signal traces having identical lengths. The other two conductors adjacent to the signal conductors were connected to a ground. The distance between the two signal traces was approximately 0.425mm, and the distance between the signal trace and the nearby ground pin was 0.4125mm, so that the EM signal coupling between the differential pair conductors, and the coupling of each signal conductor to the adjacent ground were comparable. The length of the connector was approximately 12.3mm. A dielectric with relative permittivity of 3.3 filled most of the volume around

these connector pins, as shown in Fig. 3 (a). The dielectric is hidden in most figures to provide a clear picture of the connector structure. There was a partial U-channel ground connection piece under these four conductors connecting the two ground pins at two points, as shown in Fig. 4 (b). The module board in the simulation was limited to only one pair of pins to save simulation time.

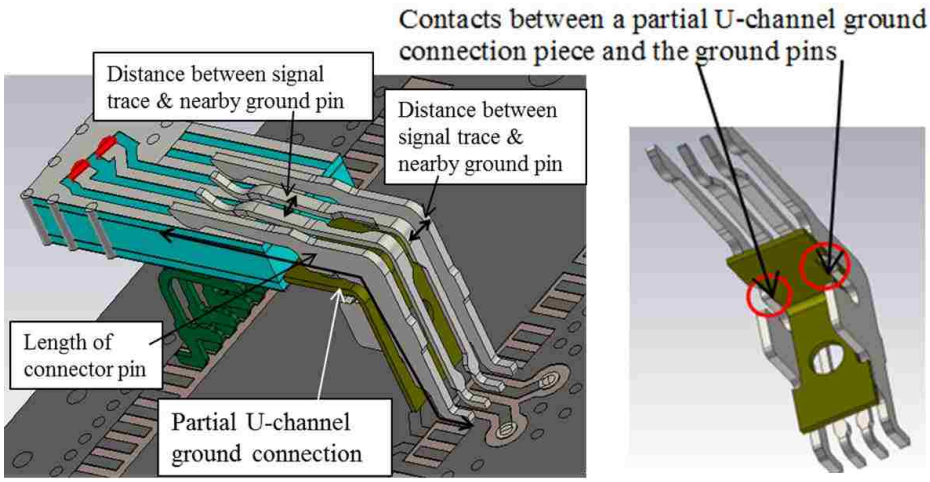

(a) (b)

Fig. 4. Optical cage connector structure of one pair of signal and ground pins. (a) One differential pair of the connector with test boards. (b) Partial U-channel ground connection under the four pins connecting two ground pins at two points.

3.2 **Simulation Model Validation (TRP)**

A mode-stirred dual reverberation chamber (RC) was used to evaluate the total radiated power (TRP) from the optical cage connector [17]-[24]; and, only the connector was in the receiving side of the chamber as shown in Fig. 3 (b). The data rate for the connector was 25Gbps, and in the commercial product testing the second harmonic was particularly troublesome, so the working frequency of this study was up to 28GHz. Due to equipment and set-up limitations at high frequencies, a single port excitation was used in

the RC measurement to validate the simulation model. Throughout this paper, simulated and measured results are compared for this single-ended excitation. Fig. 3 (a) depicts the simulation model in CST Microwave Studio. Only a small portion of the host board around the connector was modeled to reduce the simulation burden. The difference between the measurement and the simulation, as shown in Fig. 5, was within 5dB.

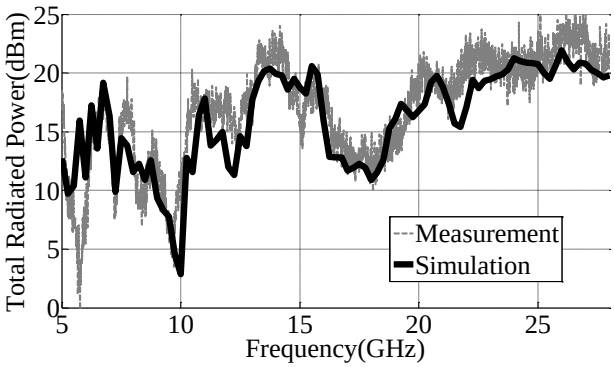

Fig. 5. TRP comparison between simulation and measurement.

After corroborating the simulation model with single-ended excitation, the TRP with differential- and common-mode signal excitations were compared and are shown in Fig. 6. The TRP from the common-mode excitation was approximately 3dB higher than that from single-ended excitation because the input power was 1W for the former and 0.5W for the latter. For the differential-mode signal excitation, radiation was significantly lower than the common-mode signal excitation below 18GHz, but above 18GHz, it was comparable. The product uses differential signaling, and EMI problems were more severe at high frequencies due to the limitations of the shielding, so a differential-mode signal excitation was used to analyze the radiation physics of the optical cage connector.

To make the simulation more time efficient during the discovery process, the simulation model was reduced to one pair of signal and ground pins, as shown in Fig. 4 (a). The comparison of TRP with the complete connector model having four differential signal pairs with the two ground reference blades is shown in Fig. 7. The overall trends agree, and the difference was caused by the scattering from nearby conductors in the complete connector model.

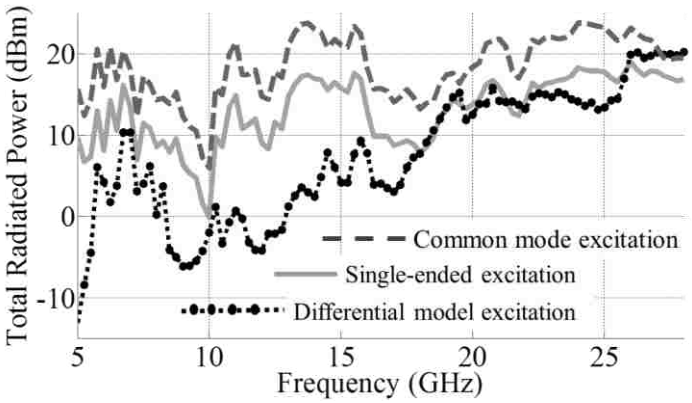

Fig. 6. TRP with single-ended, differential-mode, and common-mode excitations.

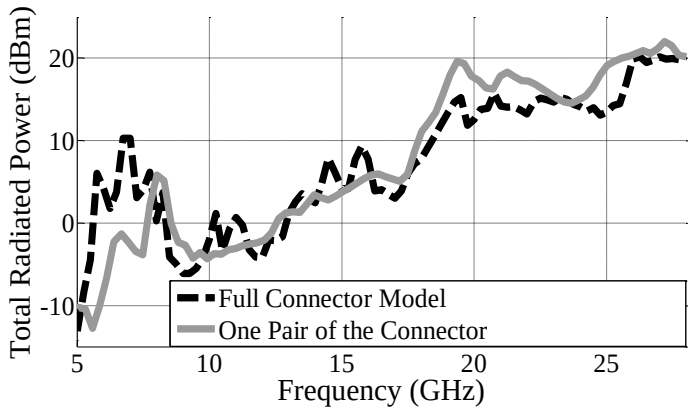

Fig. 7. TRP comparison between the complete connector model and the model with only one pair of signal and ground pins, with differential-mode excitation.

4. RADIATION MECHANISM OF OPTICAL CAGE CONNECTOR

4.1 Impact of Termination Board Design on Radiation

The traces on the module board shown in Fig. 8 (a) had the same lengths and were connected with a 100 Ω resistor to match the differential signals. To minimize the influence from the module board, and focus on the radiation from the connector structure, the module board was modified in the simulation model, as shown in Fig. 8 (c). The TRP comparison between different module board designs is shown in Fig. 9. With well-connected return conductors in the modified small module board, the TRP was greater than 10 dB less at approximately 8GHz, which corresponded to a λ/2 length of the ground pins. No radiation peaks occurred at one wavelength or one and a half wavelengths due to the contribution of the partial U-channel ground connection under the connector pins, as will be discussed in the next section.

Due to the discontinuity and parasitic inductance of the return conductors in the original module board, a sharp valley existed in $|S_{dd21}|$ at approximately 8 GHz as shown in Fig. 10 (a), and the mode conversion from differential mode to common mode was much higher than with the small module board, as shown in Fig. 10 (b).

The surface currents at 8 GHz are shown in Fig. 11. Comparing Fig. 11 (a) to (b) and (c), the currents on the two adjacent ground conductors were excited with the original module board design due to the higher differential- to common-mode conversion, and contributed to the TRP at the λ/2 resonance.

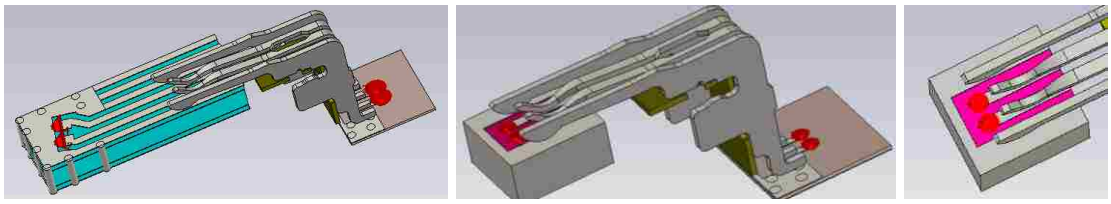

(a) (b) (c)

Fig. 8. Simulation model of one pair of signal and ground pins. (a) With original module board design. (b) With smaller module board design, and (c) symmetric termination layout on the smaller module board.

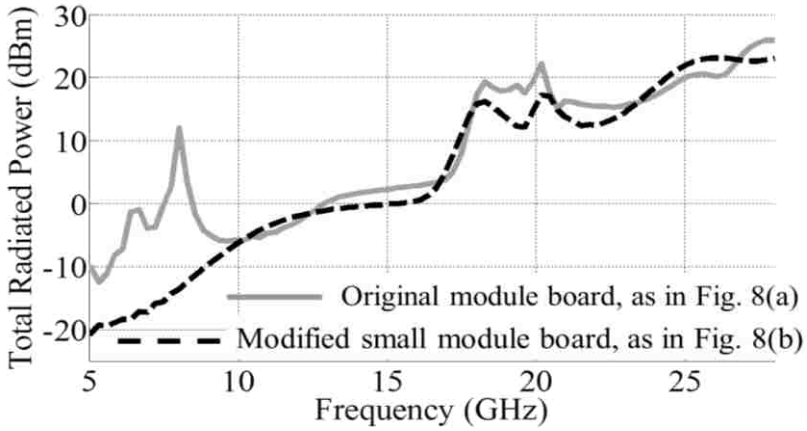

Fig. 9. TRP comparison between different module board designs.

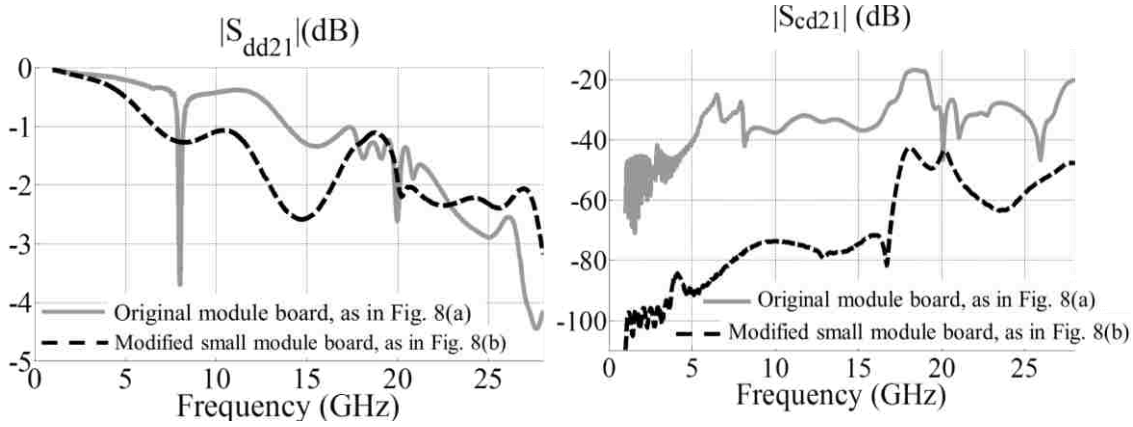

(a) (b)

Fig. 10. Mixed-mode S parameter comparison between different module board designs. (a) |Sdd21|, transmission coefficient for differential signals. (b) |Scd21|, transmission coefficient for mode conversion from differential mode to common mode.

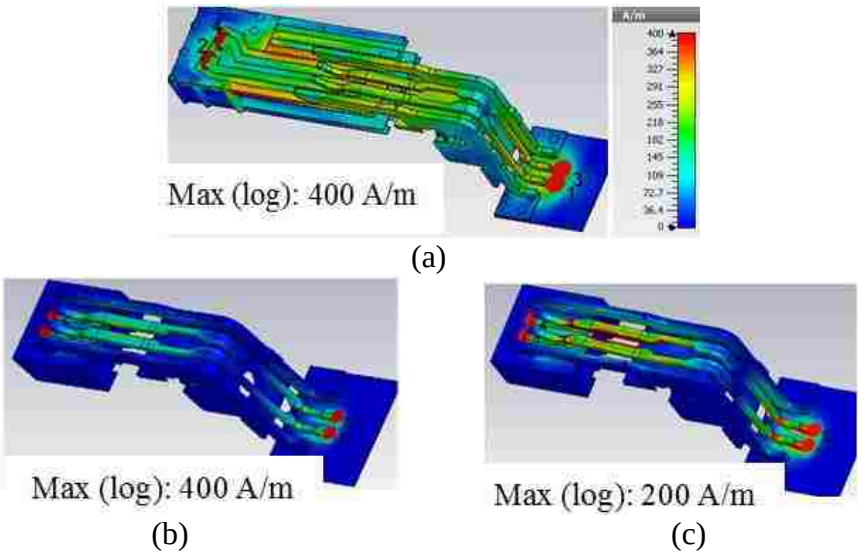

(a)

(b) (c)

Fig. 11. Surface currents with different module board designs at 8GHz. (a) Original module board design as in Fig. 8a. (b) Modified small module board design as in Fig. 8b/c. (c) Modified small module board design with smaller max value of color map.

4.2 **EMI Suppression with Partial U-Channel Ground**

The small module board was used in the simulations for the termination of the connector to minimize its effect on the TRP. The EMI performance of two connector structures shown in Fig. 12 was analyzed. One of the structures did not have the partial U-channel ground conductor under the four connector pins; the other one had a partial U-channel ground connection connecting the two ground pins on the two sides. Fig. 12 (b) is the same as Fig. 8 (b), and it is shown here for the comparison with Fig. 12 (a).

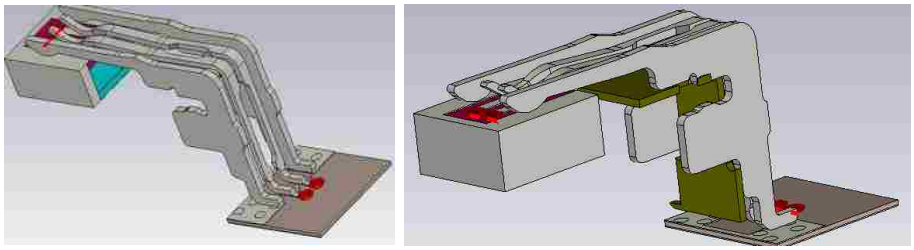

(a) (b)

Fig. 12. Simulation model of one pair of signal and ground pins with a small module board, (a) without a partial U-channel ground connection under the four connector pins, and, (b) with a partial U-channel ground connection piece under these four conductors connecting the two ground pins at two points, as shown in Fig. 4 (b).

The TRP comparison in Fig. 13 illustrates that the radiation at half-wavelength resonances was suppressed with the partial U-channel ground connection, which occurred because the common-mode conversion was dramatically suppressed at these resonances, as shown in Fig. 14. Without the partial U-channel ground connection, the highest $|S_{cd21}|$ was approximately -30dB, as shown in Fig. 14 (b), due to the design of the ground pins [15]-[16]. However, with the partial U-channel ground connection, $|S_{cd21}|$ was reduced by approximately 40 dB at these resonances.

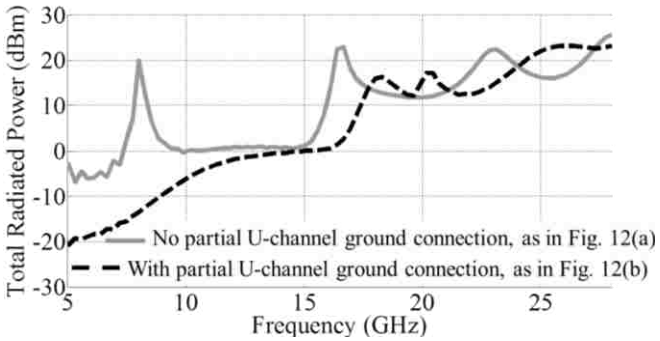

Fig. 13. TRP comparison for the simulation models with and without partial U-channel ground connection under the 4 connector pins (in Fig. 12).

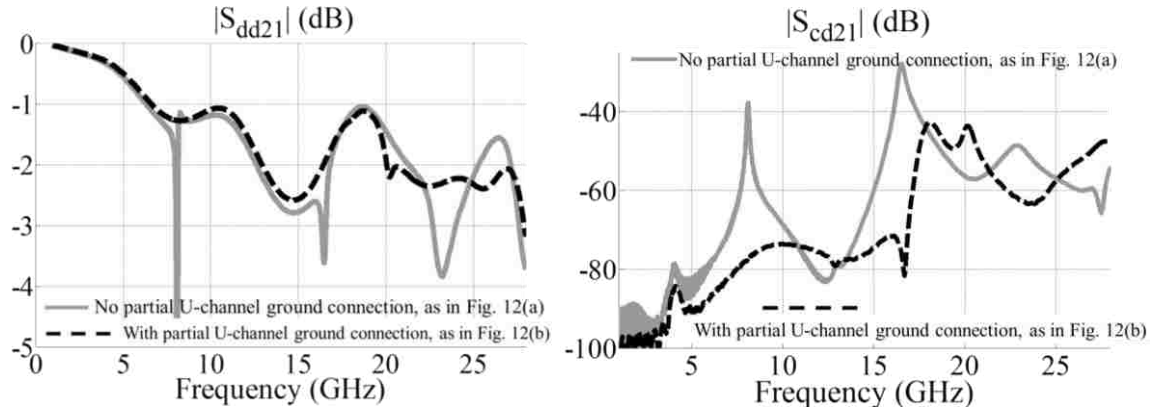

Fig. 14. Mixed-mode S parameter comparison with and without partial U-channel ground connection under the four connector pins. (a) |Sdd21|, transmission coefficient of differential signals. (b) |Scd21|, mode conversion from differential mode to common mode.

The comparison of surface currents in Fig. 15 (a)-(b) shows that the currents on the ground pins were suppressed with the partial U-channel ground connection at the half-wavelength resonance of 8GHz. For the four connector pins without the partial U-channel ground connection, the currents on the ground pins radiated at the half-wavelength resonances. When the frequency was not at the resonance, the currents on the ground pins were less, as shown in Fig. 15 (c). The partial U-channel ground connection between the two ground conductors suppressed the radiating currents. At 16.4 GHz, the same conclusion was drawn from the current distribution in Fig. 16.

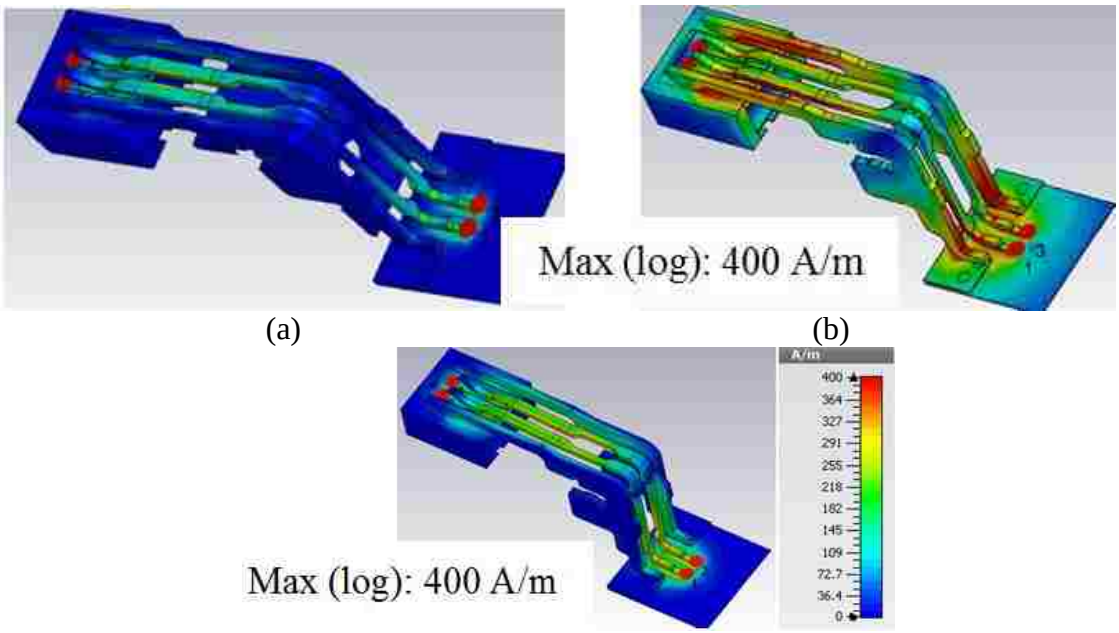

(a) (b)

(c)

Fig. 15. Surface currents of one pair of signal and adjacent ground conductors with a small module board. (a) with a partial U-channel ground connection under the four connector pins at 8 GHz, (b) without a partial U-channel ground connection under the four connector pins at 8GHz, and, (c) without a partial U-channel ground connection under the four connector conductors at a non-resonant frequency 11GHz.

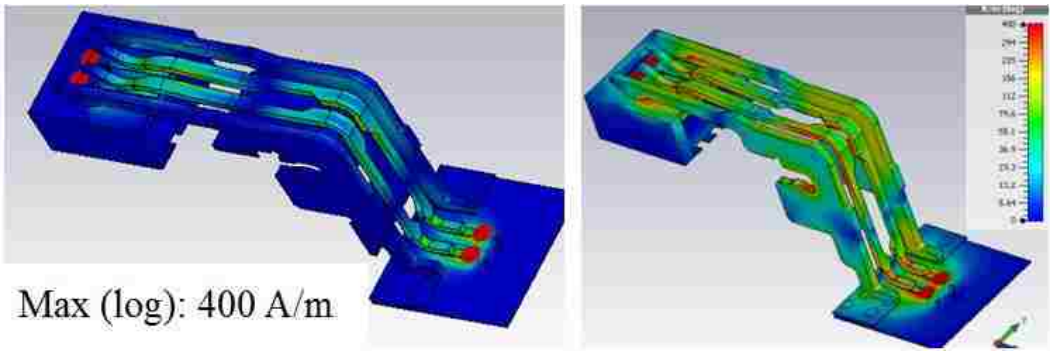

(a) (b)

Fig. 16. Surface currents of one pair of signal and adjacent ground conductors with a small module board at 16.4 GHz. (a) with a partial U-channel ground connection under the four connector pins, and, (b) without a partial U-channel ground connection under the four connector pins.

4.3 **Radiation Physics above 18GHz**

Figs. 6, 9, and 13 illustrate that radiation above 18 GHz with differential signal excitation was comparable to that with common-mode signal excitation. Further, the partial U-channel connection of the adjacent ground conductors had little impact as well. The simulation model of the connector structure was simplified further by reducing it to only two traces, as shown in Fig. 17 (a).

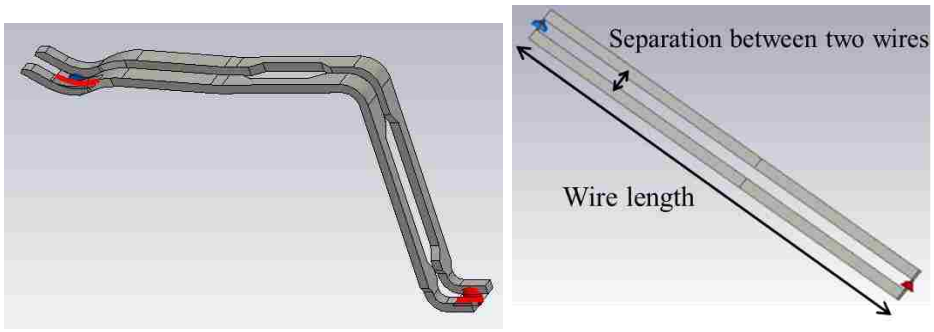

(a) (b)

Fig. 17. Two conductors with 100 Ω resistor as termination and lumped port as excitation. (a) Two signal traces from the original connector structure. (b) Two straight conductors with approximately the same separation and length as the signal traces in the original connector structure.

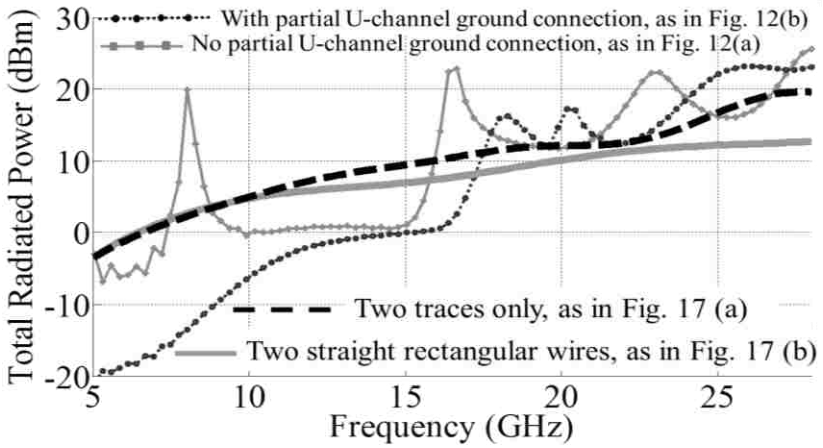

Fig. 18. TRP comparison for the simulation models in Figs. 12 and 17.

The TRP is shown in Fig. 18 from the two traces with the results of Fig. 13 from four conductors with differential excitation also shown. Above approximately 18 GHz, the radiated power from the two signal traces was similar to the radiated power from the four conductors shown in Fig. 12. Two straight conductors with the same length and approximately the same separation of the signal traces in the original connector structure, as shown in Fig. 17 (b), was introduced to investigate the bend effect. The cross-section of each conductor is 0.2mm by 0.2mm, which is approximately the same as the thickness of the conductors in the connector. Comparing the TRP for two bent signal traces with the two straight conductors as shown in Fig.18 indicates that the TRP is increased 3-7 dB with the bend. The two conductors shown in Fig. 17 were excited by a lumped port; thus, the currents on the two conductors had the exact same magnitude and opposite directions. However, at high frequency, the radiation from these current segments does not cancel each other well. The TRP from two straight wires is calculated over a spherical surface S from [25]-[27]:

$$TRP = \eta \frac{{I_0}^2}{2\pi^2} \oiint_S \frac{\sin^2\theta}{\left(\cos\theta - 1\right)^2 r^2} \sin^2\left[kl\left(\cos\theta - 1\right)\right] \sin^2\left(kh\sin\theta\right) ds \qquad (1)$$

where η is wave impedance in free space, (r, θ, φ) are the spherical coordinates of observation pint, $k = 2\pi/\lambda$ is wave number, l is the wire length and h is the separation distance between two wires, and I_0 is the current magnitude on the wire.

The TRP from two thin straight wires with traveling wave currents increases if the frequency, wire length, or separation between the two wires increases. The effect of the conductor length, separation between the two conductors, and frequency on the TRP was studied, and shown in Figs. 19 and 20. The initial conductor length was 12.3mm, and the separation between the conductors was 0.526mm. The radiated power increased by

approximately 15dB, from 10GHz to 30GHz, as shown in Figs. 19 (a) and 20 (a). The relationship between the TRP and *kl* or *kh* is shown in Figs. 19 (b) and 20 (b), respectively. TRP varies linearly as 20dB/decade until $l = \lambda/2$. Increasing the wire length did not increase the TRP significantly after approximately $l = \lambda/2$. Similarly, when *kh* is small, TRP varies linearly as 20dB/decade until $h = \lambda/2$. The TRP increased by approximately 13dB when kh increases approximately from 0.1 to 0.5. Therefore, the TRP is more sensitive to the wire separation than to the wire length, when $l = \lambda/2$ and $h = \lambda/2$.

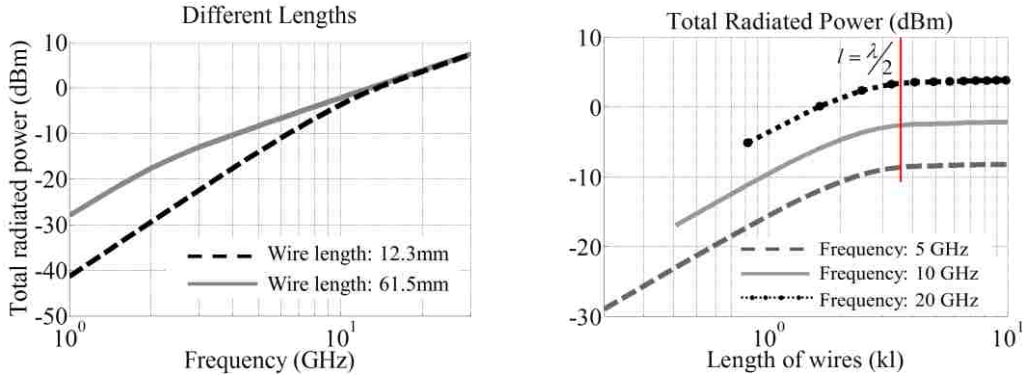

(a) (b)

Fig. 19. TRP calculated with (1) for different conductor lengths. (a) TRP vs. frequency from 1 to 30GHz. (b) TRP vs. kl at 5, 10, 20 GHz.

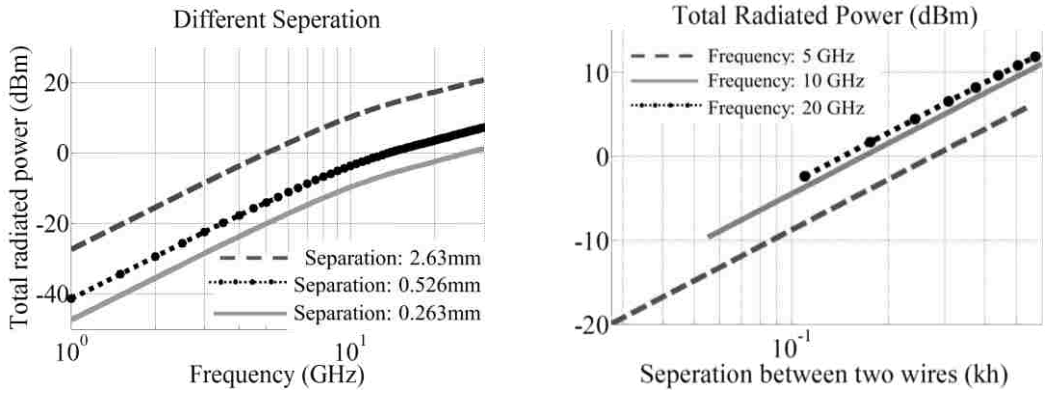

(a) (b)

Fig. 20. TRP calculated with (1) for different separation between the two conductors. (a) TRP vs. frequency from 1 to 30GHz. (b) TRP vs. kh at 5, 10, 20GHz.

5. EMI MITIGATION AND VERIFICATION OF COUPLING PATH

5.1 EMI Mitigation with Absorbing Material

An absorbing material ECCOSORB BSR-2 with 1 mm thickness from Laird Technology was applied around the connector to reduce the TRP as shown in Fig. 21. The material parameters of the absorbing material are shown in Fig. 22. The material parameters from 18GHz to 28GHz used in the simulation were curve-fitted with a general polynomial formulation in CST Microwave Studio. The TRP for the simulation and measurement are compared in Fig. 23, showing agreement within 3dB. The TRP from the optical cage connector was reduced approximately 4 to 10 dB from 10 GHz to 30GHz with the application of the absorbing material in both the simulation and the measurement.

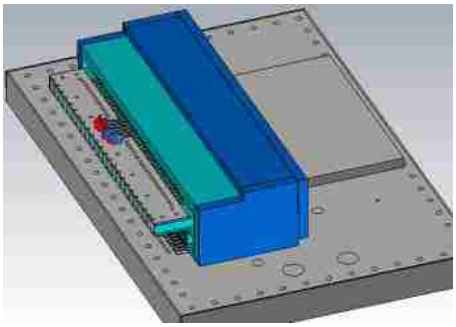

Fig. 21. Simulation model with 1mm thickness of absorbing material around the connector.

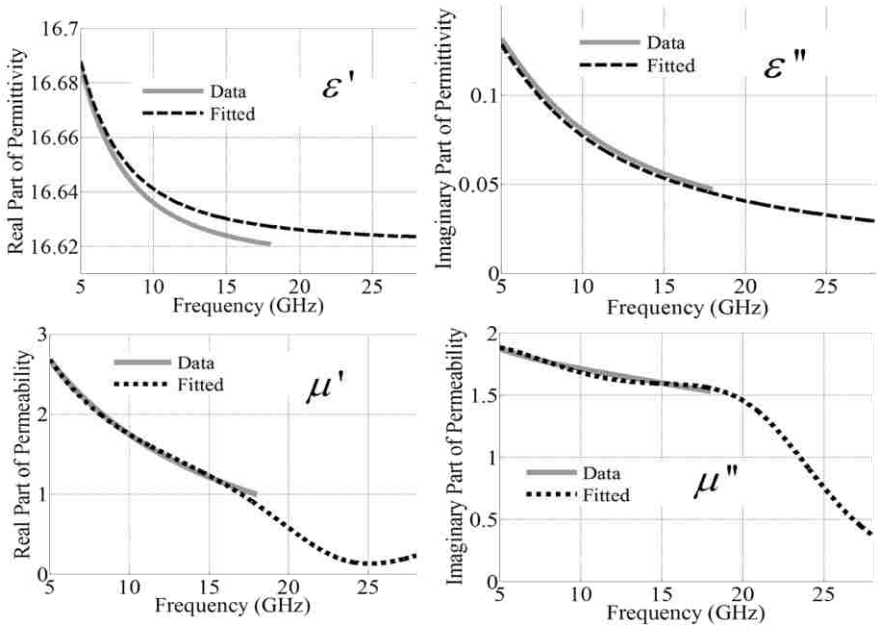

Fig. 22. Material parameters (relative permittivity and permeability) for the Liard Technology ECCOSORB BSR-2 absorbing material.

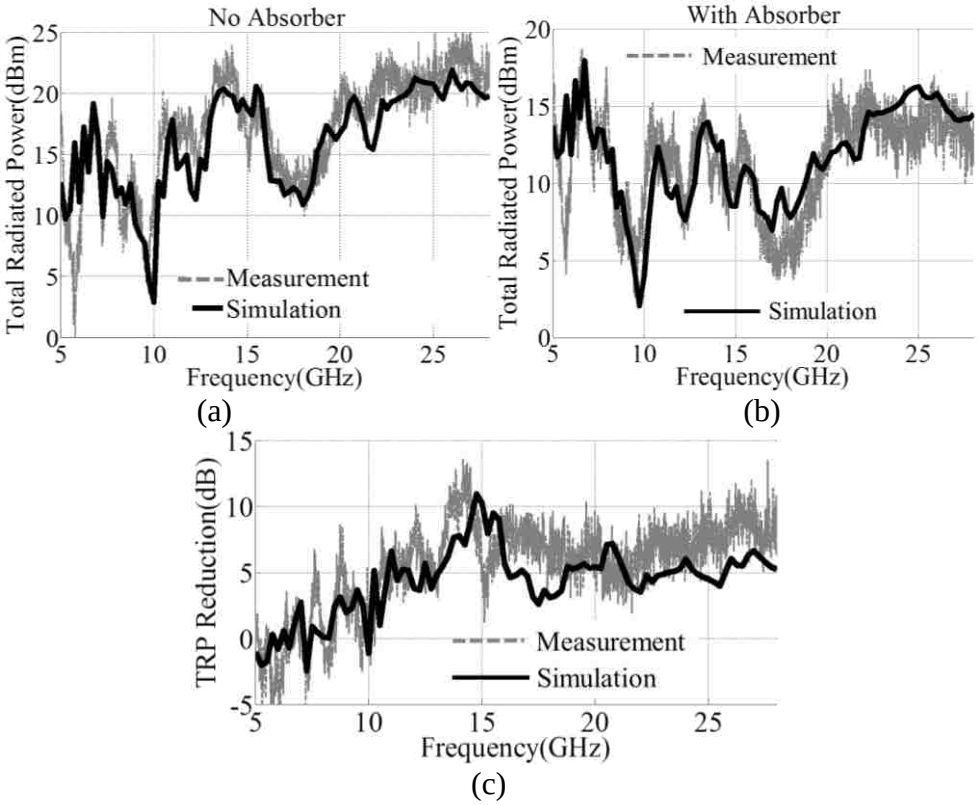

Fig. 23. Comparison of TRP from the optical cage connector between simulation and measurement, (a) without absorbing material, (b) with 1mm thickness of absorbing material around the connector, and, (c) TRP reduction (TRP without absorber minus TRP with absorber).

5.2 Verification of the EMI Coupling Physics

An optical cage connector has been proposed as one of the main coupling paths in the link through the optical sub-assembly [4], with the leakage point being the gap between the optical cage and the optical module enclosure. Before verifying the coupling path, a simulation model of the optical cage connector with the optical cage and module enclosure was verified. The simulation model is shown in Fig. 24 (a-c), and the test vehicle of the TRP in the reverberation chamber is shown in Fig. 24(d). The test vehicle was enclosed in copper tape, leaving only the end into which the optical cables are connected open. The absorber inside the optical cage only covered the top and back sides of the connector (Fig. 24 (a)) due to the mechanical design in the product. The frequency range considered was from 8 GHz to 28 GHz, which covers the fundamental and second harmonics of the 25 Gbps data rate.

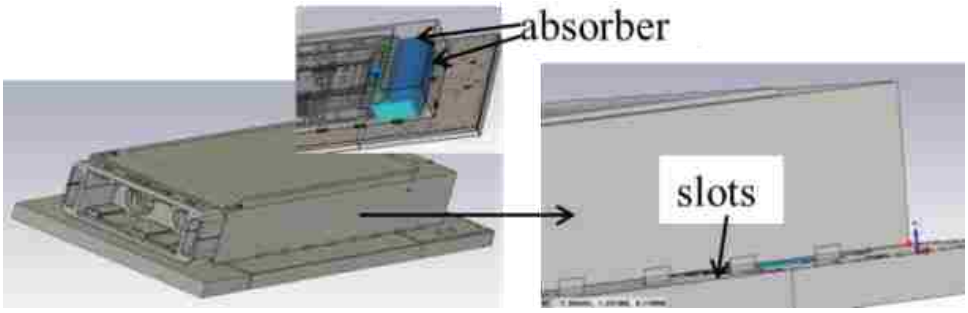

(a) (b)

Fig. 24. Connector with optical cage and optical module enclosure. (a) Simulation model with absorber only on the top and back sides of the connector.

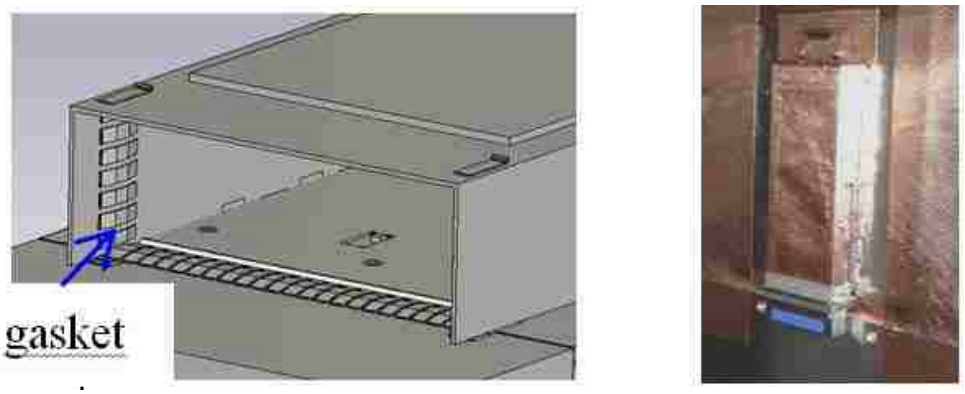

(c) (d)

Fig. 24. Connector with optical cage and optical module enclosure. (c) Gasket inside of optical cage to contact the optical module sub-assembly enclosure. (d) Test vehicle in reverberation chamber. (Cont.)

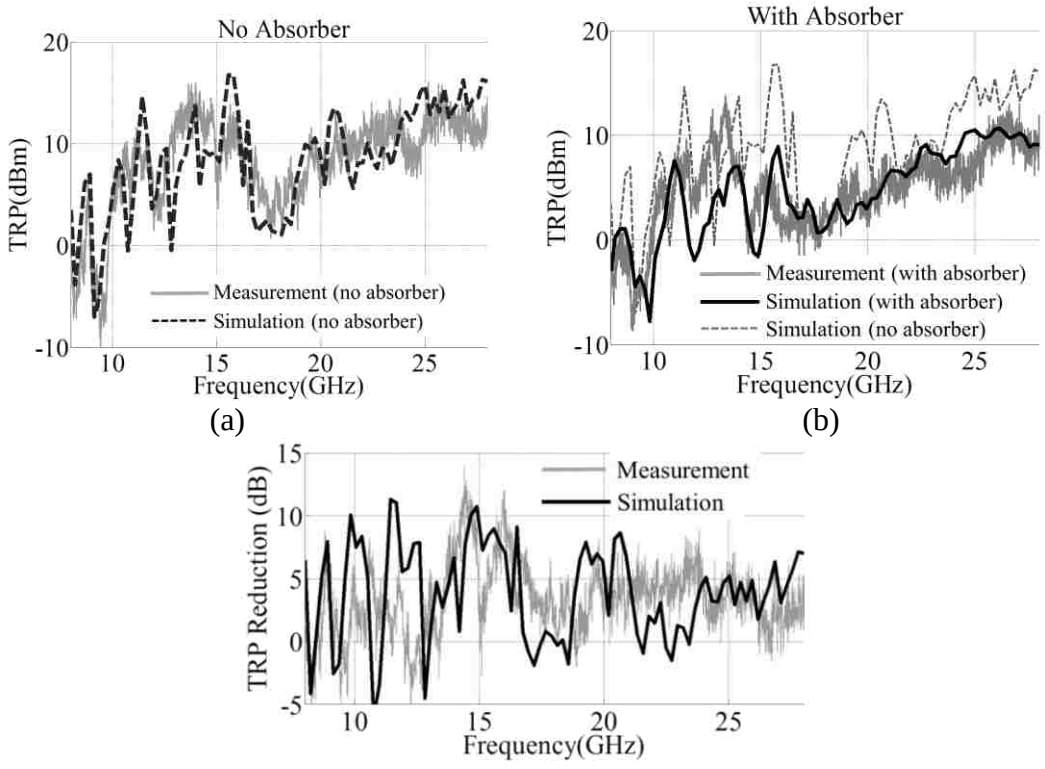

(a) (b)

(c)

Fig. 25. Comparison of TRP from optical cage connector, optical cage, and module enclosure between simulation and measurement, (a) without absorbing material, (b) with 1mm thickness of absorbing material on the top and back surfaces of the connector, and, (c) TRP reduction (TRP without absorber minus TRP with absorber).

The TRP with and without the absorbing material was compared between the simulation and the measurement in the reverberation chamber, and is shown in Fig. 25 (a-b), and the TRP reduction is shown in Fig. 25 (c). Several possible reasons exist for the discrepancy between the simulation and measurement results. The TRP is very sensitive to the conducting connections and resulting slots between the optical cage and the PCB, shown in Fig. 24 (b), especially the slots near the optical cage connector. A 10 dB variance was observed at some frequencies when the slot spacing between the cage shield and the PCB (with top layer GND plane) changed by 0.25mm. In the measurement, the slots were not easily kept the same every time when the cage was assembled to the PCB, and the cage needed to be reassembled to the PCB after the absorbing material was added. The contact between the optical module sub-assembly enclosure and the cage introduced another uncertainty. However, for most frequencies, the discrepancy was within 5dB, indicating that the simulation model can be used for further analysis.

The EMI coupling physics were investigated in simulation. The front opening of the module enclosure was completely sealed as shown in Fig. 26 (a), the slots between the optical cage and PCB were eliminated, and the gasket between the optical cage and the module enclosure, as shown in Fig. 24 (c), was removed. The leakage was then confined to the gap between the cage conductor and the optical sub-assembly module enclosure. Then, the simulated TRP was compared for the cases with and without absorbing material around the connector, as shown in Fig. 26 (b). The leakage from the gap between the optical cage and the module enclosure decreased by 5 to 10 dB with absorber applied around the connector, as shown in Fig. 27, demonstrating the coupling path from the optical cage connector.

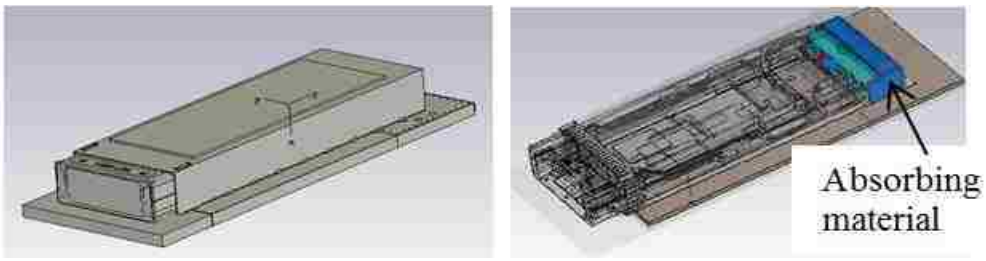

(a) (b)

Fig. 26. Simulation model of the optical cage connector with optical cage and optical module enclosure. (a) Front of the module enclosure shielded with a PEC block. (b) 1 mm thickness of absorbing material around the connector.

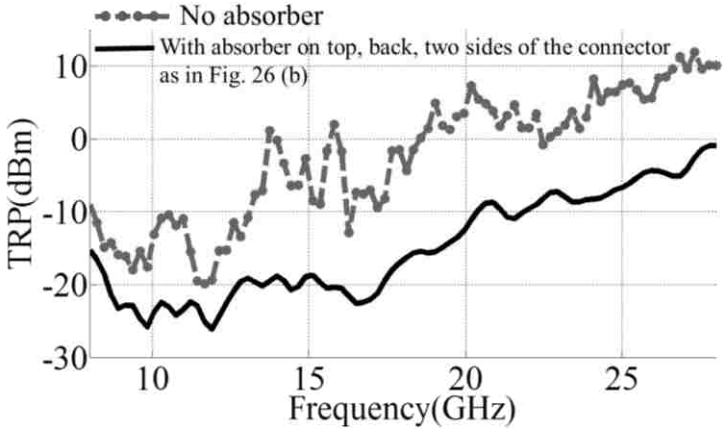

Fig. 27. Radiated power reduction from the gap between optical cage and module enclosure, with and w/o absorber around the optical cage connector.

6. CONCLUSIONS

An optical cage connector is one of the primary coupling paths in an optical link. The EMI physics of the optical cage connector was analyzed with full-wave simulation from 4GHz to 28GHZ. Below approximately 18GHz, the radiated power was caused by the currents on the ground pins in the connector structure. A termination board with well-connected return conductors and reduced inductance in it, and the partial U-channel ground conductor connection piece connecting the ground conductors adjacent to the differential signal pair conductors, reduced the radiation at half-wavelength resonances. Above 18GHz, the radiation from differential signals on the signal conductors was significant, and was related to the separation between the signal conductors, frequency, and conductor length. One approach for EMI mitigation of the coupling from the connector was an absorbing material partially covering the connector. With a 1mm thickness of absorbing materials around the connector, the radiated power decreased by approximately 4 to 10 dB above 10 GHz.

REFERENCES

[1] T.-L. Wu, W.-S. Jou, S. G. Dai, and W.-H. Cheng, "Effective electromagnetic shielding of plastic packaging in low-cost optical transceiver modules," J. Lightw. Technol., Jun. 2003, vol. 21, no. 6, pp. 1536–1543.
[2] H. Oomori, M. Shiozaki, and H. Kurashima, "Development of a practical electro-magnetic interference (EMI) simulation in high speed optical transceivers," in Electronic Components and Technology Conference, San Diego, CA, USA, 2009, pp. 1908-1913.
[3] D. Kawase, H. Oomori, M. Shiozaki, and H. Kurashima, "EMI suppression of 10Gbit/s optical transceiver by using EBG structure," in Proc. 2011 IEEE Int. Symp. Electromagn. Compat., Long Beach, CA, USA, Aug. 2011, pp. 33-38.
[4] J. Li, S. Toor, A. Bhobe, J. L. Drewniak, J. Fan, "Radiation physics and EMI coupling path determination for optical links," in Proc. 2014 IEEE Int. Symp. Electromagn. Compat., Raleigh, NC, USA, Aug. 2014, pp. 576-581.
[5] X. Tian, M. S. Halligan, X. Li, K. Kim, H.-C. Chen, S. Connor, B. Archambeault, M. Cracraft, A. E. Ruehli, and J. L. Drewniak, "Modeling electromagnetic radiation at high-density PCB/connector interfaces," in Proc. 2011 IEEE Int. Symp. Electromagn. Compat., Raleigh, NC, USA, Aug. 2014, pp. 97-102.
[6] M. Leone, and V. Navrátil, "On the electromagnetic radiation of printed-circuit-board interconnections," IEEE Trans. Electromagn. Compat., vol. 47, no. 2, pp. 219-226, May 2005.
[7] M. Torigoe, A. Sadatoshi, Y. Toyota, K. Iokibe, R. Koga, T. Watanabe, and O. Wada, "Prediction of the common-mode radiated emission from the board to board interconnection through common-mode antenna model," in Proc. 2008 IEEE Int. Symp. Electromagn. Compat., Detroit, MI, USA, Aug. 2008, pp. 1- 4.
[8] Y. Toyota, A. Sadatoshi, T. Watanabe, K. Iokibe, R. Koga, and O. Wada, "Prediction of electromagnetic emissions from PCBs with interconnections through common-mode antenna model," in 2007 Int. Zurich Symp. Electromagn. Compat., Munich, Germany, Sept. 2007, pp.107-110.
[9] B. Archambeault, S. Connor, M. S. Halligan, J. L. Drewniak, and A. E. Ruehli, "Electromagnetic radiation resulting from PCB/high-density connector interfaces," IEEE Trans. Electromagn. Compat., vol. 55, no.4, pp. 614-623, Aug. 2013.
[10] L. K. C. Wong, "Backplane connector radiated emission and shielding effectiveness," in Proc. 1992 IEEE Int. Symp. Electromagn. Compat., Aug. 1992, pp. 346–351.
[11] Z. Li, P. Yu, and C.-P. Chua, "The EMI characteristics of high speed backplane connector," in Proc. 2012 Int. Symp. Electromagn. Compat., Rome, Italy, Sep. 2012, pp. 1-4.
[12] H. C. Chen, S. Connor, T. L. Wu, B. Archambeault, "The effect of various skew compensation strategies on mode conversion and radiation from high-speed connectors," in Proc. 2013 IEEE Int. Symp. Electromagn. Compat., Denver, CO, USA, Aug. 2013, pp. 328–332.
[13] H. Fan; X. Zhou; A. Bhobe, J. Yu; H. Zhang, and P. Sochoux, "An analytical approximation for evaluating impact of skew length on radiated emission from

differential signal pairs," in Proc. 2012 Asia-Pacific Symp. Electromagn. Compat. (APEMC), Singapore, May 2012, pp. 673-676.
[14] P. Sochoux, M. Hsu, A. Bhobe, and J. Yu, "EMI from SerDes differential pairs," Designcon 2009, Santa Clara, CA, USA, Jan., 2009.
[15] X. Duan, B. Archambeault, H.-D. Bruens, C. Schuster, "EM emission of differential signals across connected printed circuit boards in the GHz range," in Proc. 2003 IEEE Int. Symp. Electromagn. Compat., Austin, TX, USA, Aug. 2009, pp. 50-55.
[16] C.-Y. Hsiao, T.-L. Wu, C.-N. Chiu, S.-H. Wang; C.-C. Wang, W.-S. Wang, and Y.-H. Lin, "Radio-frequency interference mitigation strategies for high speed connector," in Proc. 2013 IEEE Electrical Design of Advanced Packaging and Systems Symposium (EDAPS), Nara, Japan, Dec. 2013, pp. 56-59.
[17] X. Zhou, J. Li, H. Fan, A. Bhobe, P. Sochoux, J. Yu, "High-frequency EMC design verification through full-wave simulations and measurements in reverberation chamber," in Proc. 2013 IEEE Int. Symp. Electromagn. Compat., Denver, CO, USA, Aug. 2013, pp. 299-305.
[18] D. Hill, Electromagnetic Fields in Cavities: Deterministic and Statistical Theories, Wiley, 2009.
[19] H.G.Krauthauser, "On the Measurement of Total Radiated Power in Uncalibrated Reverberation Chambers," IEEE Trans. Electromagn. Compat., vol.49, no.2, pp.270-279, May 2007.
[20] Wilson, P.F., Hill, D.A., Holloway, C.L., "On determining the maximum emissions from electrically large sources," IEEE Trans. Electromagn. Compat., vol.44, no.1, pp.79-86, Feb 2002.
[21] Holloway, C.L., Wilson, P.F., Koepke, G., Candidi, M., "Total radiated power limits for emission measurements in a reverberation chamber," in Proc. 2003 IEEE Int. Symp. Electromagn. Compat., Boston, MA, USA, Aug. 2003, vol.2, 18-22, pp.838-843.
[22] Holloway, C.L., Hill, D.A., Sandroni, M., Ladbury, J.M., Coder, J., Koepke, G., Marvin, A.C., Yuhui He, "Use of Reverberation Chambers to Determine the Shielding Effectiveness of Physically Small, Electrically Large Enclosures and Cavities," IEEE Trans. Electromagn. Compat., vol.50, no.4, pp.770-782, Nov. 2008.
[23] Holloway, C.L.; Hill, D.A.; Ladbury, J.; Koepke, G.; Garzia, R., "Shielding effectiveness measurements of materials using nested reverberation chambers," IEEE Trans. Electromagn. Compat., vol.45, no.2, pp.350-356, May 2003.
[24] Holloway, C.L.; Shah, H.A.; Pirkl, R.J.; Young, W.F.; Hill, D.A.; Ladbury, J., "Reverberation Chamber Techniques for Determining the Radiation and Total Efficiency of Antennas," IEEE Trans. Antennas and Propagation, vol.60, no.4, pp.1758-1770, April 2012.
[25] C. Balanis, Antenna Theory, Analysis, and Design, 2nd ed. New York: Wiley, 1997.
[26] C. H. Walter, Traveling Wave Antennas, McGraw-Hill, New York, 1965.
[27] Nakamura, T.; Hayashi, N.; Fukuda, H.; Yokokawa, S., "Radiation from the transmission line with an acute bend," IEEE Trans. Electromagn. Compat., vol.37, no.3, pp.317-325, Aug 1995.

II. Radiation Physics and Design Guidelines of High-Speed Connectors

Jing Li, *Student member, IEEE,* and Jun Fan, *Senior member, IEEE*

***Abstract*—**High-speed connectors contribute to system level EMI. Radiation from antenna mode current and TL mode current is briefly reviewed with a backplane connector and an optical cage connector. The radiation from the high-speed connector with TL-mode current is analyzed in detail. The possible radiation mechanisms are analyzed respectively through Green's function method, steepest descent method, and EMC Studio method of moment (MoM). Design guidelines of high-speed connectors for EMI mitigation are proposed based on the analysis of radiation physics.

Index Terms—High-speed connectors, EMI, radiation mechanism, steepest descent method, Green's function method, high frequency, design guideline.

1. INTRODUCTION

High-speed connectors are commonly used for transmitting signals between multiple printed circuit boards (PCB) in system level designs, as shown in Fig.1, and have been a major factor of radiated emission for systems up to the GHz range. Some board-to-board connectors have signal conductors with different lengths such as edge-coupled PCB backplane connectors 0 as shown in Fig. 2 (a), while optical cage connectors are typically broad-side coupled, identical in length, and symmetric [2] as shown in Fig. 2 (b). Currents along the connector structure can be decomposed into "antenna mode" current and "transmission line mode" (TL mode) current [3]-[10]. If the sum of all the currents crossing a plane perpendicular to the direction of the line is not zero, then it is the so-called "antenna mode" currents; otherwise, one can consider the "transmission line mode" currents only. The mechanism of antenna mode current is briefly illustrated with a backplane connector in section II, but is not the focus of the study in this paper because the radiation from connectors with different lengths of signal conductors has been the subject of previous studies [10]-[16], and the effect of skew compensation on mode conversion and radiation was discussed in [17]-[19]. As the speed of digital circuits increases to tens of Gbps, the frequency range of EMI problems goes up to tens of GHz and covers at least two harmonics of the system operation frequency. The radiation from high-speed PCB connectors with differential mode signaling is widely used in digital electronic devices in order to establish a high-speed digital propagation with low electromagnetic interference (EMI) [18]-[20]. However, the ability of the fields to cancel each other deteriorates as the frequency increases [22]-[27], even if the lengths of the differential signal conductors are exactly the same. When the optical cage connector

(which has equal length signal conductors) was excited with differential mode signals, the radiation at high frequency was similar to the radiation from two signal conductors, which is equivalent to the radiation from a bent two-wire transmission line with TL mode current [2], [27]. Despite numerous analytical, experimental, and theoretical [28]-[38] work that has been carried out on radiation from a bent two-wire transmission line, the radiation mechanism has yet to be fully understood. In this paper, the radiation physics of a two-wire transmission line was analyzed using the Green's function method, the steepest descent method [32], and EMC Studio's method of moments (MoM) solver. The objective of this study was to understand the radiation physics of high-speed connectors and to propose design guidelines for EMI mitigation.

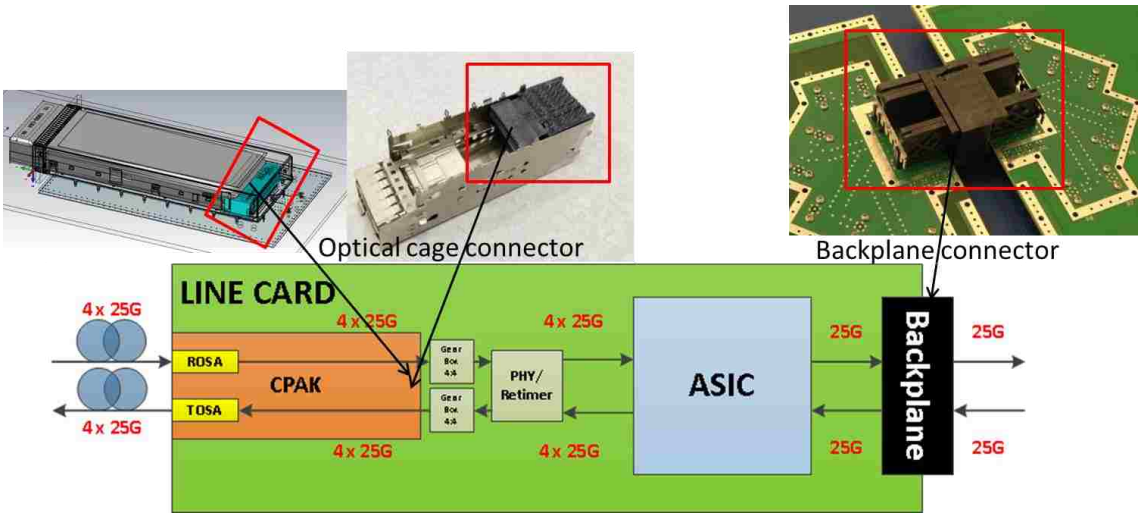

Fig. 1. High-speed connectors on a line card: optical cage connector and backplane connector.

(a)

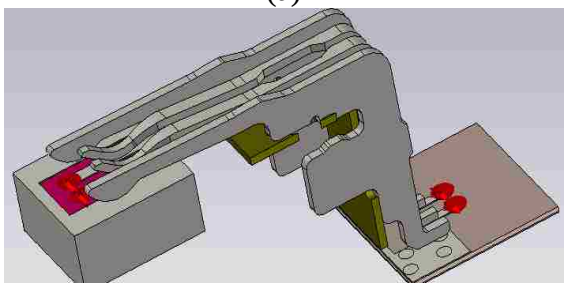

(b)

Fig. 2. Detailed structure of the connectors. (a) One slice of backplane connector, (b) one pair of signal conductors and adjacent reference ground conductors of optical cage connector.

Radiation from antenna mode current and TL mode current is illustrated with a backplane connector and an optical cage connector in Section II and III, respectively. The radiation from the high-speed connector with TL mode current is the focus of the study here. The possible radiation mechanisms and the quantification approaches are described in Section IV. The radiation physics of straight and bent two-wire transmission line is analyzed with Green's function method and steepest descent method in Sections V and VI. With discontinuities on the two ends of the connector, the contribution of standing wave currents to radiation is presented in Section VII. Based on the understanding of the radiation physics of the high-speed connectors, design guidelines for EMI mitigation are proposed in Section VIII.

2. EMI FROM CONNECTORS WITH ANTENNA MODE CURRENT

2.1 Radiation due to Antenna Mode Current

The simulation model of the backplane connector in CST Microwave Studio is shown in Fig. 3. One model is shown with 4000 mil by 4000 mil PCB planes on the two ends, while the other one is shown with two small PCBs on the two ends for excitation and termination of the connector. The total radiated power (TRP) is compared in Fig. 4. Below 1 GHz, the radiation is due to the antenna mode currents on the big PCB planes and the connector. The resonances at higher frequencies in TRP are due to the antenna mode currents along the connector, as shown in Fig. 5 [1], [14]-[17].

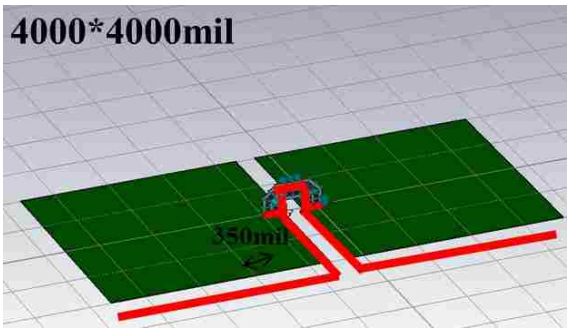

(a)

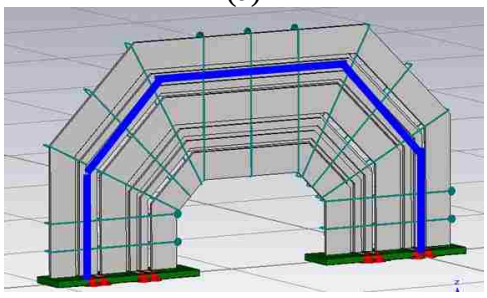

(b)

Fig. 3. Backplane connector models. (a) With large PCB plane, (b) with small PCB on the two ends of the connector for excitation and termination.

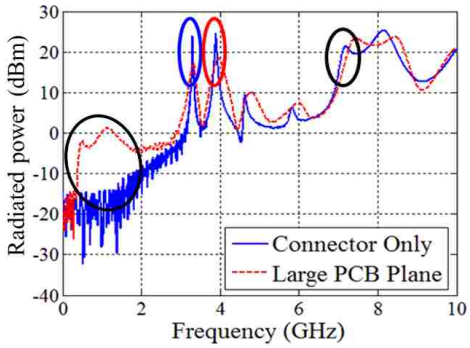

Fig. 4. Radiated power comparison of backplane connector with and without big PCB plane.

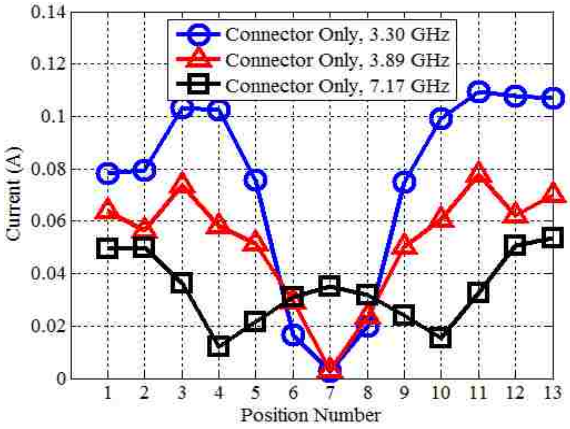

Fig. 5. Antenna current along the backplane connector at resonant frequencies in TRP, from the simulation model in Fig. 3 (b).

2.2 **Possible Mechanisms of Antenna Mode Current**

There are two possible mechanisms that generate antenna-mode currents on the connectors. One is the skew in signal conductors when two differential signal conductors have different lengths, or they are skewed in time, or the rise and/or fall time on the two signal conductors is different [18], [24], [38]. The other mechanism is due to the change of the imbalance factor. The antenna mode signals that arise from the conversion of TL mode signals at the interface of two structures can be quantified by the difference of the imbalance factor and the TL mode signals at the interface [30]-[49]:

$$V_{AntennaMode} = \triangle h \times V_{TL-M}(x) \quad (1)$$

where

$$\Delta h = h_2 - h_1 \quad (2)$$

and h_1, h_2 are the imbalance factor of two structures, respectively. V_{TL-M} is the TL mode voltage at the interface.

The imbalance factor h of each structure can be calculated by self-capacitance or inductance [39], [49]-[50].

Therefore, two design guidelines are proposed to reduce radiation caused by the antenna mode current. The signal conductors should have well-referenced nearby ground conductors for the return currents. The antenna mode current on the connector structure can be reduced proportionally to the decrease in the difference of the imbalance factor of the PCB connected to the connector and the imbalance factor of the connector, when the TL mode current does not change.

3. EMI FROM CONNECTORS WITH TL MODE CURRENT

Optical cage connectors for optical subassembly I/O modules on a line card were identified as one of the main coupling paths in an optical link at the front end of switches and routers [2], [27]. CST Microwave Studio was used to simulate the optical cage connector with test boards on the two ends for excitation and termination, as shown in Fig. 6 (a). The simulation model was corroborated by comparing the measured and simulated results for TRP [2]. The TRP for differential and common mode signal excitations is compared in Fig. 7. Below 18 GHz the differential mode signal excitation radiation was significantly lower than the common mode signal excitation, but above 18 GHz it was comparable. The product uses differential signaling, and EMI problems are more severe at high frequencies because of the limitations of the shielding, so a differential mode signal excitation was used to analyze the radiation physics of the optical cage connector at high frequencies.

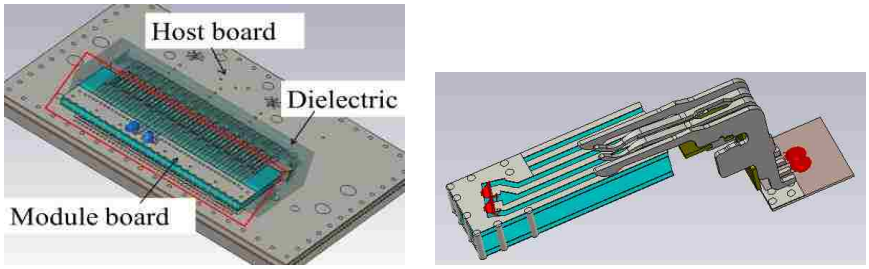

(a) (b)

Fig. 6. Optical cage connector models with test boards on the two ends for excitation and termination. (a) The complete connector, (b) one pair of signal conductors and the adjacent reference ground conductors.

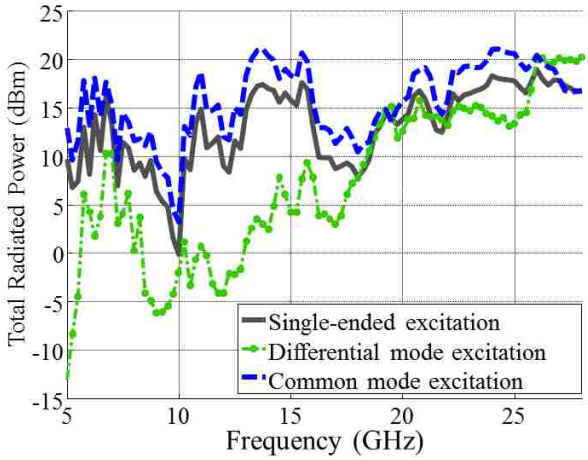

Fig. 7. TRP simulation results of the complete connector structure, as in Fig. 6 (a), with single-ended, differential mode, and common mode excitations.

The simulation model of one pair of signal conductors and the adjacent ground conductor is shown in Fig. 6 (b). The comparison of TRP with the complete connector model having four differential signal pairs with two ground reference blades for each pair is shown in Fig. 8. The overall trends agree, and the difference was caused by the scattering from nearby conductors in the complete connector model. The radiation from the optical cage connector is similar to the radiation from the excited signal pair and the adjacent reference ground conductors. The simulation model was further reduced to be two signal conductors excited with a lumped port and terminated with a lumped element, as shown in Fig. 9 (a), with currents on the signal conductors having the same magnitude, but opposite directions. The TRP was compared to the results of the simulation models described in Fig. 6, and as shown in Fig. 8.

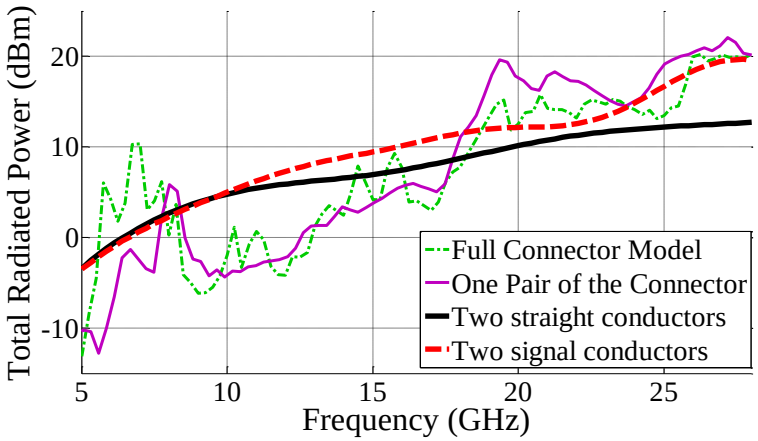

Fig. 8. TRP comparison from the simulation models in Fig. 6 and Fig. 9.

Above 18 GHz, the radiation from two signal conductors with TL mode currents is similar to the radiation from the complete connector structure with a differential mode excitation. TRP from two straight conductors (Fig. 9 (b)), with dimensions similar to the signal conductors of the connector, was also compared in Fig. 8. The TRP increased 3-7 dB with the presence of bends in the signal conductors. Therefore, to understand the radiation from optical cage connectors, the radiation physics of a two-wire transmission line with TL mode currents was analyzed. Two basic structures are shown in Fig. 10, a straight two-wire transmission line and a two-wire transmission line with a right-angle bend. Bent wires with other angles are not considered in this paper because two wires with right-angle bends have the highest radiation loss at high frequency [31]. As shown in Fig. 10, the length of the wires is 100 mm, and the separation between the two wires is 1.5 mm. For the bent wires, the right-angle bends are at mid-point of the wires. The frequency range for this study is from 0.1 GHz to 10 GHz.

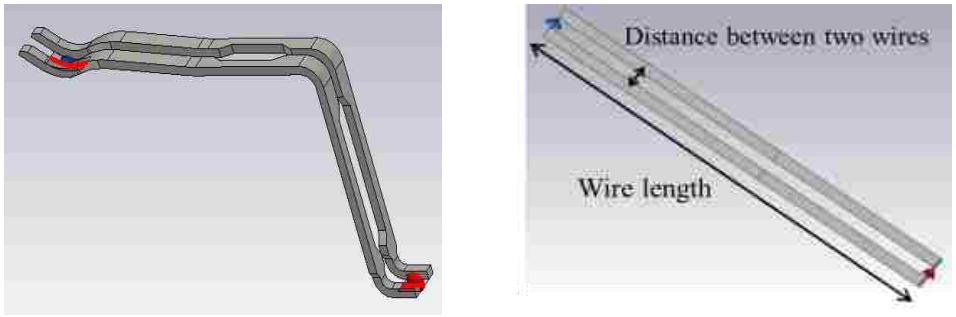

(a) (b)

Fig. 9. Two conductors with 100 Ω resistor as termination and lumped port as excitation. (a) Two signal traces from the original connector structure, (b) two straight conductors with approximately the same separation and length as the signal conductors in the original connector structure.

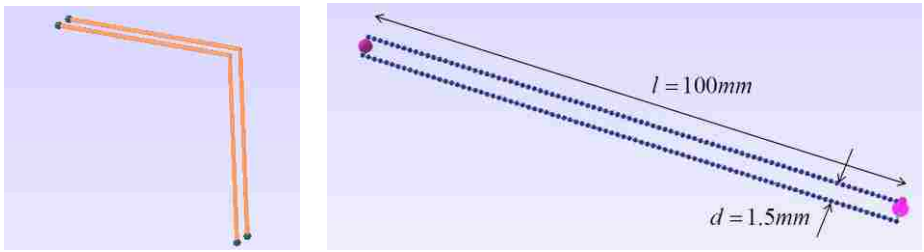

(a) (b)

Fig. 10. Extracted two-wire transmission line model considering the differential excitation in the connector structure. (a) Bent wires, (b) straight wires.

4. POSSIBLE MECHANISMS AND QUANTIFICATION APPROACHES

4.1 Possible Mechanisms of Antenna Mode Current

With the currents having the same magnitude and opposite directions on the two wires of a two-wire transmission line, the possible radiation mechanisms in the GHz range are the contribution from the vertical segments used to connect the source and load to the two wires (termed "end-wire effect"), the radiation caused by the discontinuities at the two ends of the wires, the bends in the two wires, and the influence of mismatch. The end-wire effect was analyzed in [27], and the contribution to TRP is less than 2 dB when the wire separation is larger than one hundredth of the wavelength. In the analysis of other possible radiation mechanisms, the end-wire effect was not considered. Two wires with travelling wave currents (2) are studied in sections V and VI, and the influence of mismatch at the two ends of the wires is discussed in section VII.

4.2 Quantification Approaches

Three approaches were used to analyze the radiation mechanisms. With EMC studio (MoM), currents along a two-wire transmission line, as well as TRP, can be calculated. Using Green's function in free space, the electric and magnetic fields in the far field region can be calculated analytically from known currents $\boldsymbol{J}(r')$:

$$\boldsymbol{H}(\boldsymbol{r}) \simeq -jk\frac{e^{-jkr}}{4\pi r}\hat{\boldsymbol{r}}\times\int_V\left[\boldsymbol{J}(\boldsymbol{r}')e^{jk\hat{\boldsymbol{r}}\cdot\boldsymbol{r}'}\right]dV \tag{3}$$

$$\boldsymbol{E}(\boldsymbol{r}) \simeq jk\eta\frac{e^{-jkr}}{4\pi r}\hat{\boldsymbol{r}}\times\hat{\boldsymbol{r}}\times\int_V\left[\boldsymbol{J}(\boldsymbol{r}')e^{jk\hat{\boldsymbol{r}}\cdot\boldsymbol{r}'}\right]dV \tag{4}$$

where r is the observation point, r' is the source location, η is the wave impedance in free space, $k = 2\pi/\lambda$ is the wave number, and $\boldsymbol{J}(r')$ is the current vector along wires.

TRP can be calculated over a spherical surface *S* in the far field:

$$\boldsymbol{P} = \oiint_S \boldsymbol{E} \times \boldsymbol{H} \cdot d\boldsymbol{S} \tag{5}$$

A two-wire transmission line can be divided into a number of cascaded short, uniform dipole segments. The fields from the entire wires can be obtained by the integration of the currents on the wires (3)-(4), which was implemented by the summation of all the contributions from each dipole segment on the wires. With Green's function method, the distribution of J and the current segment location $\boldsymbol{r}'$ were manipulated to analyze the radiation mechanisms in section VI.

Another approach is the steepest descent method [32], which shows the radiation physics in the expression. The radiated field is the summation of the contribution from all the discontinuities in the two-wire transmission line structure:

$$\boldsymbol{H}^{rad} \approx \sum_{i=1}^{N} \frac{\boldsymbol{j}_i \times \boldsymbol{j}_r}{\beta/k - \boldsymbol{j}_i \cdot \boldsymbol{j}_r} e^{-j\beta\xi_i} \frac{e^{-jkr} e^{jk(\boldsymbol{d}_i \cdot \boldsymbol{j}_r)}}{4\pi r} U_i I_i \tag{6}$$

where *N* is the total number of discontinuities, $U_0 = \pm 1$ with the positive sign for the generation of the traveling wave currents and the negative sign for the vanishing ones. $\boldsymbol{j}_i$ is the unit vector of current discontinuity $\#i$, and $\boldsymbol{j}_r$ is the unit vector in the *r* direction. $\boldsymbol{d}_i$ is the distance vector from the origin to the point $\#i$, as shown in Fig. 13. $I_i = I_0$ is the right going wave (RGW) current at discontinuity $\#i$.

Green's function method and steepest descent method were verified using the following procedure. TRP was calculated with Green's function method, for both straight and bent wires, using the current distribution, $\boldsymbol{J}$, exported from EMC Studio, as shown in Fig 11. TRP calculated with steepest descent method was compared to the results calculated from Green's function method in Fig. 12 for straight wires and bent wires.

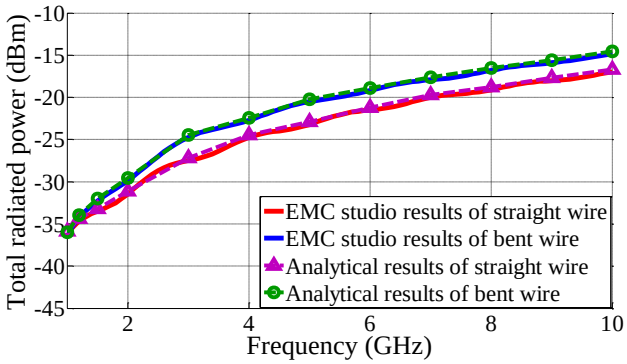

Fig. 11. Verification of Green's function method by comparing to the results from EMC studio for bent wire and straight wire.

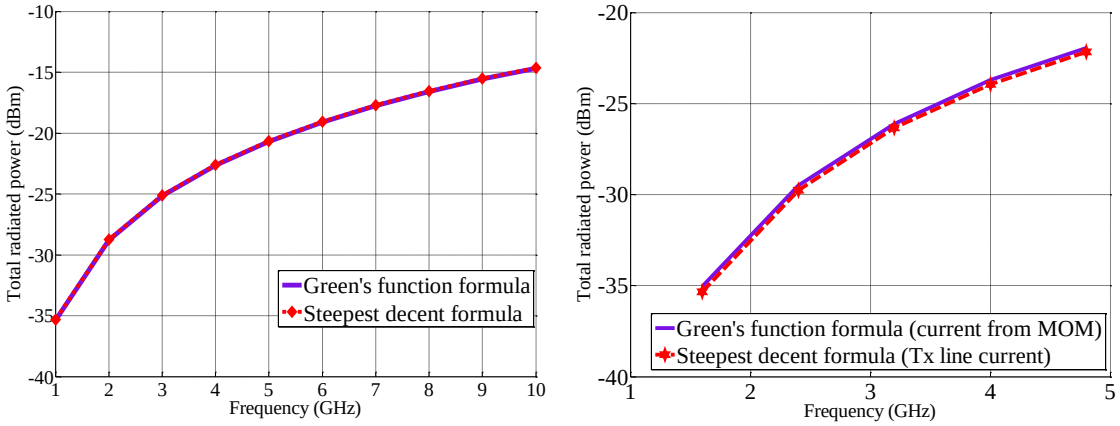

(a) (b)

Fig. 12. Verification of steepest descent method by comparing to the results from Green's function method. (a) Bent wire, (b) straight wire.

5. RADIATION PHYSICS OF STRAIGHT WIRES

For an ideal, infinitely long, straight two-wire transmission line, there is no radiation. But in reality, the lengths of the wires are finite so they radiate with/without the end-wire effect. Considering two straight wires without end-wire effect, there are four discontinuities at the two ends due to the finite length. The vector and coefficients in (6) become:

$$
\begin{aligned}
&\boldsymbol{j}_1 = \boldsymbol{j}_2 = \boldsymbol{j}_3 = \boldsymbol{j}_4 = \boldsymbol{j}_z \\
&\boldsymbol{j}_r = \boldsymbol{j}_x \sin\theta\cos\varphi + \boldsymbol{j}_y \sin\theta\sin\varphi + \boldsymbol{j}_z \cos\theta \\
&\boldsymbol{d}_1 = \boldsymbol{j}_x h - \boldsymbol{j}_z \xi_1, \boldsymbol{d}_2 = \boldsymbol{j}_x h + \boldsymbol{j}_z \xi_1, \boldsymbol{d}_3 = -\boldsymbol{j}_x h - \boldsymbol{j}_z \xi_2, \boldsymbol{d}_4 = -\boldsymbol{j}_x h + \boldsymbol{j}_z \xi_2 \\
&-\xi_1 = \xi_2 = \xi \\
&I_1 = I_2 = -I_3 = -I_4 = I_0 \\
&U_1 = U_3 = -U_2 = -U_4 = 1
\end{aligned}
\tag{7}
$$

where $2h$ is the separation distance of the two wires, and ξ is the half wire length, as shown in Fig. 13. (r, θ, φ) are the spherical coordinates of the observation point.

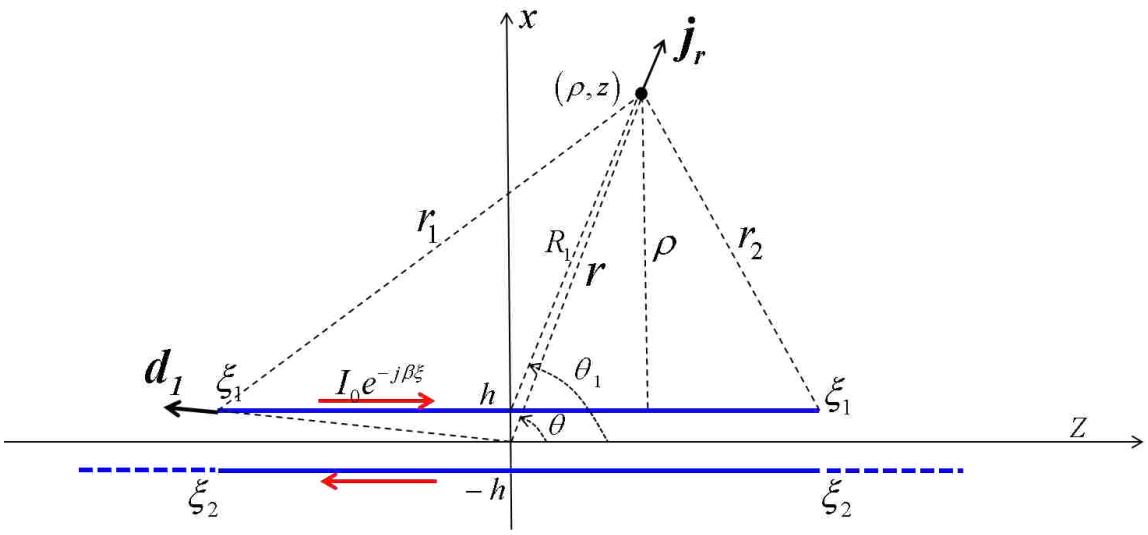

Fig. 13. Coordinate system and vectors for two straight wires calculated with steepest descent method.

TRP calculated with the steepest descent method is shown in Fig. 12 (a). It shows that the radiation from a straight two-wire transmission line is due to the finite length of the wires, which brings in the four discontinuities at the two ends of the wires.

The TRP expression of a straight two-wire transmission line was derived with (5) [51]-[52] to obtain:

$$TRP = \eta \frac{{I_0}^2}{2\pi^2} \oiint_S \frac{\sin^2\theta}{\left(\cos\theta - 1\right)^2 r^2} \sin^2\left[kl\left(\cos\theta - 1\right)\right] \sin^2\left(kh\sin\theta\right) ds \qquad (8)$$

The relationship between TRP and kl or kh are shown in Fig. 14 (a) and (b), respectively. TRP varies linearly as 20 dB/decade until $l = \lambda/2$. Increasing the wire length does not increase the TRP significantly after approximately $l = \lambda/2$. Similarly, when kh is small, TRP varies linearly as 20 dB/decade until $h = \lambda/2$. Considering the real connector design, the wire length is longer than $\lambda/2$ in most cases, which is in the constant/flat region of the relationship with TRP; the separation of the two wires, however, is smaller than $\lambda/2$, which is in the linear region of the relationship with TRP. The TRP increased by approximately 13 dB when the separation h increased from 0.016λ to 0.08λ.

Therefore, the first connector design guideline for EMI suppression from TL mode current is proposed: TRP decreases 20 dB/decade when the separation of the two wires is smaller than $\lambda/2$.

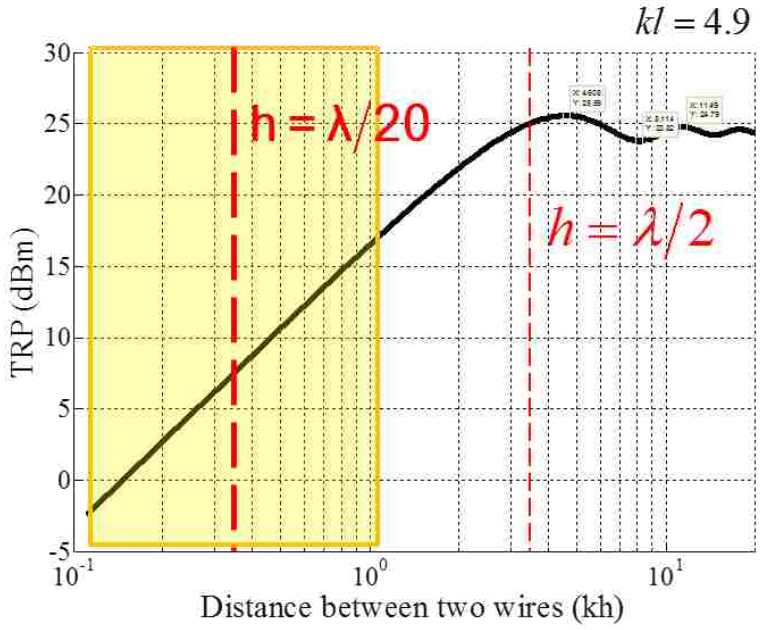

(a)

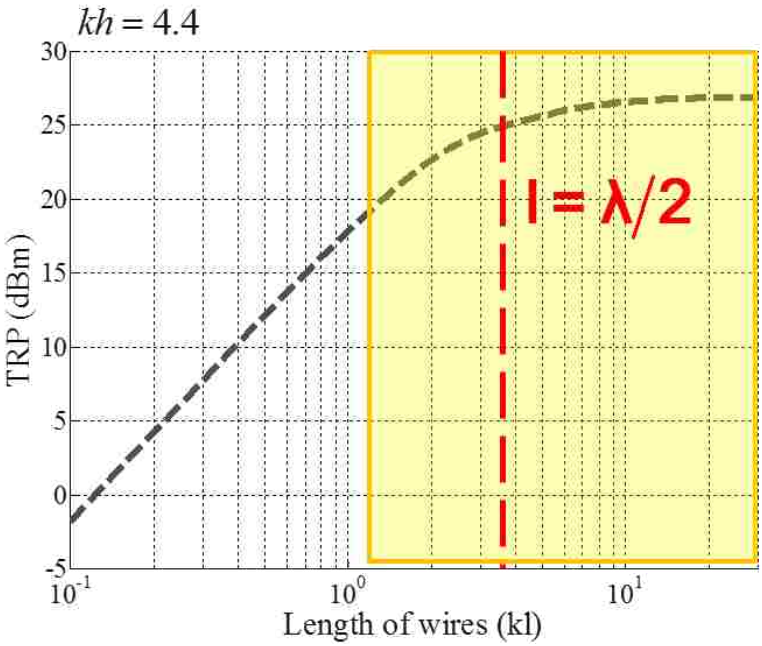

(b)

Fig. 14. TRP calculated with (8) for two straight wires. (a) TRP vs. ***kh***, (b) TRP vs. ***kl***.

6. RADIATION PHYSICS OF BENT WIRES

The current distributions on the straight wire and bent wire were extracted from EMC Studio and compared in Fig. 15. The frequency is at 3 GHz. For the bent wires, the small variations and kinks in the current distribution are caused by the discontinuities and reflections at the bends. The phases of the currents are almost the same and indicate travelling wave behavior. With the extracted current distributions, TRP was calculated with Green's function formula, and compared in Fig. 8. It is shown that as frequency increases, bent wires radiate more because of the discontinuities at the bends. More discontinuities at the bends result in more radiation [27].

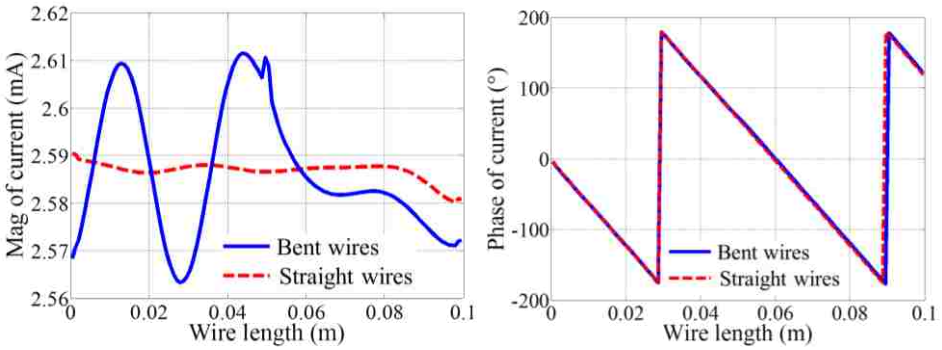

(a) (b)

Fig. 15. Current distribution at 3 GHz from straight wires and bent wires. (a) Current magnitude comparison, (b) current phase comparison.

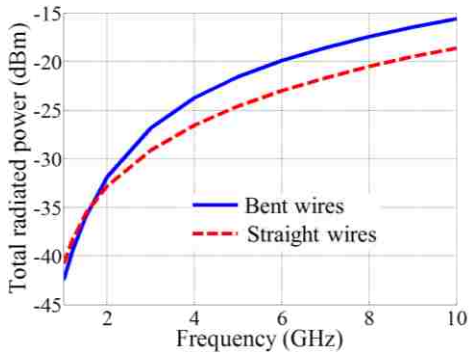

Fig. 16. TRP comparison between the straight wire and bent wires.

6.1 **Green's Function Method**

There are two possible reasons causing the increase of TRP from bent wires: the small variance in the current distributions because of the reflection at bends, or the changing of the location of current segments on the bent wires in reference to the straight wires. The radiation mechanism was analyzed with Green's function method by manipulating the current distributions and locations on the straight wires and bent wires. First, TRP was compared when the current distributions were different. In Fig. 17 (a), all current segments were set on the location of the straight wires, and the TRP was calculated with the current distributions of straight wire and bent wire in Fig. 15. Similarly, in Fig. 17 (b), the current segments were set on the location of the bent wires, and the TRP was calculated with the current distribution of straight wire and bent wire in Fig. 15. Fig. 17 illustrates that the small variance in the current distribution of the bent wires makes no difference on TRP. On the other hand, TRP was compared when the source locations $\boldsymbol{r}'$ of the current segments were different. In Fig. 18 (a), the current distribution of the straight wire was extracted from EMC Studio (MoM), and TRP was compared when the current distribution was on the segments of the straight wires and bent wires. Similarly, the current distribution of the bent wire extracted from EMC Studio (MoM) was set on the segments at the locations of the straight wires and bent wires, and the TRP was compared in Fig. 18 (b). Fig. 18 illustrates that TRP increased when the current segments were at the locations of the bent wire.

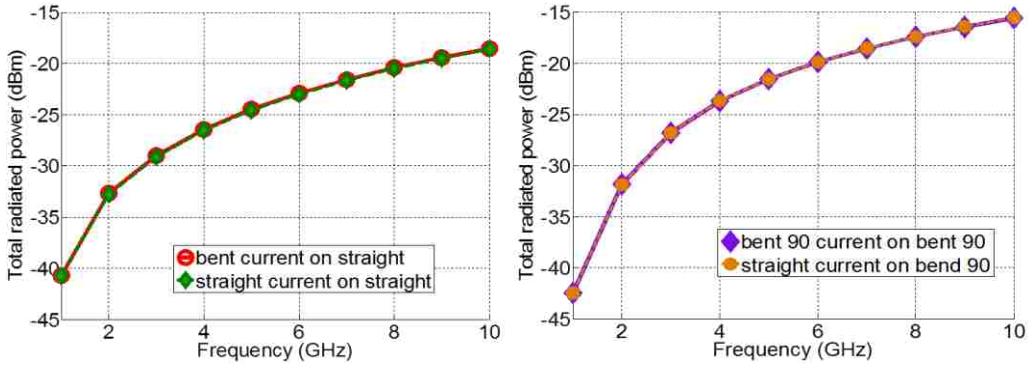

(a) (b)

Fig. 17. TRP comparison with current distributions from the straight wire and the bent wire. (a) Current segments located on the straight wire, (b) current segments located on the bent wire.

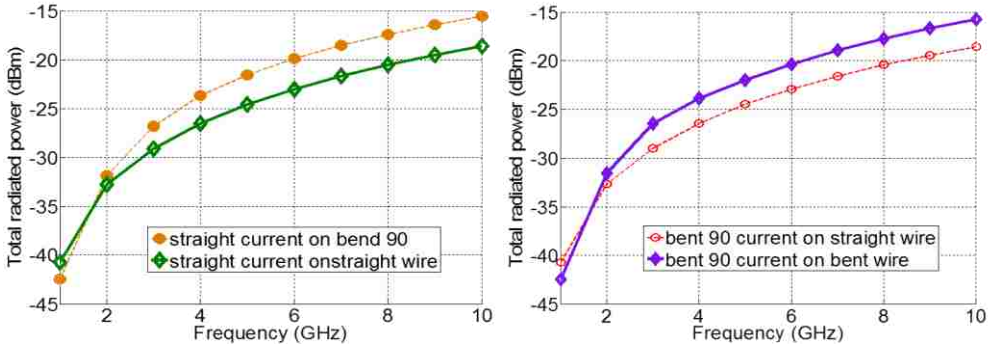

(a) (b)

Fig. 18. TRP comparison with current segments located on the straight wire and the bent wire. (a) Current distribution from the straight wire, (b) current distribution from the bent wire.

Unlike the common understanding of bent wires, the increase of radiation is not due to the reflection at the bends, as long as the current distribution is not significantly changed. Rather, the increase of TRP from the bent wire is due to the change of the current locations in reference to the straight wires.

6.2 **Steepest Descent Method**

Radiation from the bent wire can be calculated with steepest descent method [33]. For two infinitely long bent wires, there are two physical discontinuities at the bends. At each bend, there are three current discontinuities: the incident current (I_i), reflected current (I_r) and transmitted current (I_t), as shown in Fig. 19.

$$I_i = I_0,\ I_r = \Gamma I_0,\ I_t = \mathrm{T} I_0 \tag{9}$$

where Γ is reflection coefficient, and T is the transmission coefficient.

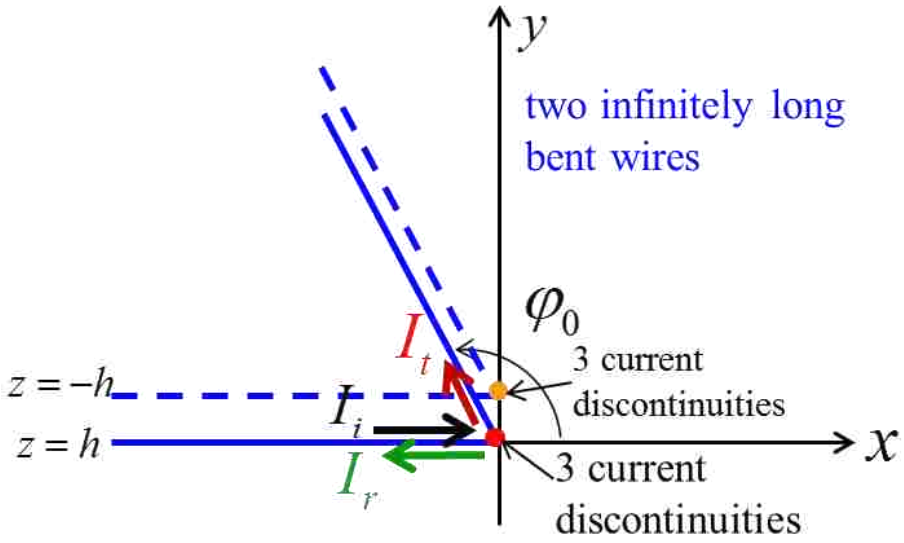

Fig. 19. Current discontinuities at the bends.

The vector and coefficients in (6) for the six current discontinuities at the two bends become:

$$
\begin{aligned}
&\boldsymbol{j_1} = \boldsymbol{j}_x, \boldsymbol{j_2} = -\boldsymbol{j}_x, \boldsymbol{j_3} = \boldsymbol{j}_x \cos\varphi_0 + \boldsymbol{j}_y \sin\varphi_0 \\
&\boldsymbol{j}_r = \boldsymbol{j}_x \sin\theta\cos\varphi + \boldsymbol{j}_y \sin\theta\sin\varphi + \boldsymbol{j}_z \cos\theta \\
&\boldsymbol{d_1} = \boldsymbol{d_2} = \boldsymbol{d}_3 = \boldsymbol{j}_z h \\
&U_1 = -1, U_2 = U_3 = 1 \\
&I_4 = -I_0, I_5 = -\Gamma I_0, I_6 = -\mathrm{T} I_0 \\
&\boldsymbol{j}_4 = \boldsymbol{j}_x, \boldsymbol{j}_5 = -\boldsymbol{j}_x, \boldsymbol{j}_6 = \boldsymbol{j}_x \cos\varphi_0 + \boldsymbol{j}_y \sin\varphi_0 \\
&\boldsymbol{j}_r = \boldsymbol{j}_x \sin\theta\cos\varphi + \boldsymbol{j}_y \sin\theta\sin\varphi + \boldsymbol{j}_z \cos\theta \\
&\boldsymbol{d}_4 = \boldsymbol{d}_5 = \boldsymbol{d}_6 = -\boldsymbol{j}_z h \\
&U_4 = -1, U_5 = U_6 = 1
\end{aligned}
\tag{10}
$$

The reflection and transmission coefficients related to the current distributions can be calculated with the travelling wave method (TWM) [4], [32]-[34]. However, from the conclusion in section VI-A that the small variance of current distribution caused by the reflection at the bends contributes little to TRP, the reflection coefficient can be set to approximately zero, and the transmission coefficient can be set to approximately one:

$$T \approx 1, \Gamma \approx 0 \tag{11}$$

In paper [32], the reflection and transmission coefficients at right-angle bends were calculated with TWM, and the 3D radiated field pattern $|E_\theta|$ and $|E_\varphi|$ are shown in Fig. 20 (a) and (b). The 3D field pattern $|E_\theta|$ and $|E_\varphi|$ from the right-angle bends calculated with (6), (10) and (11) are shown in Fig. 20 (c) and (d).

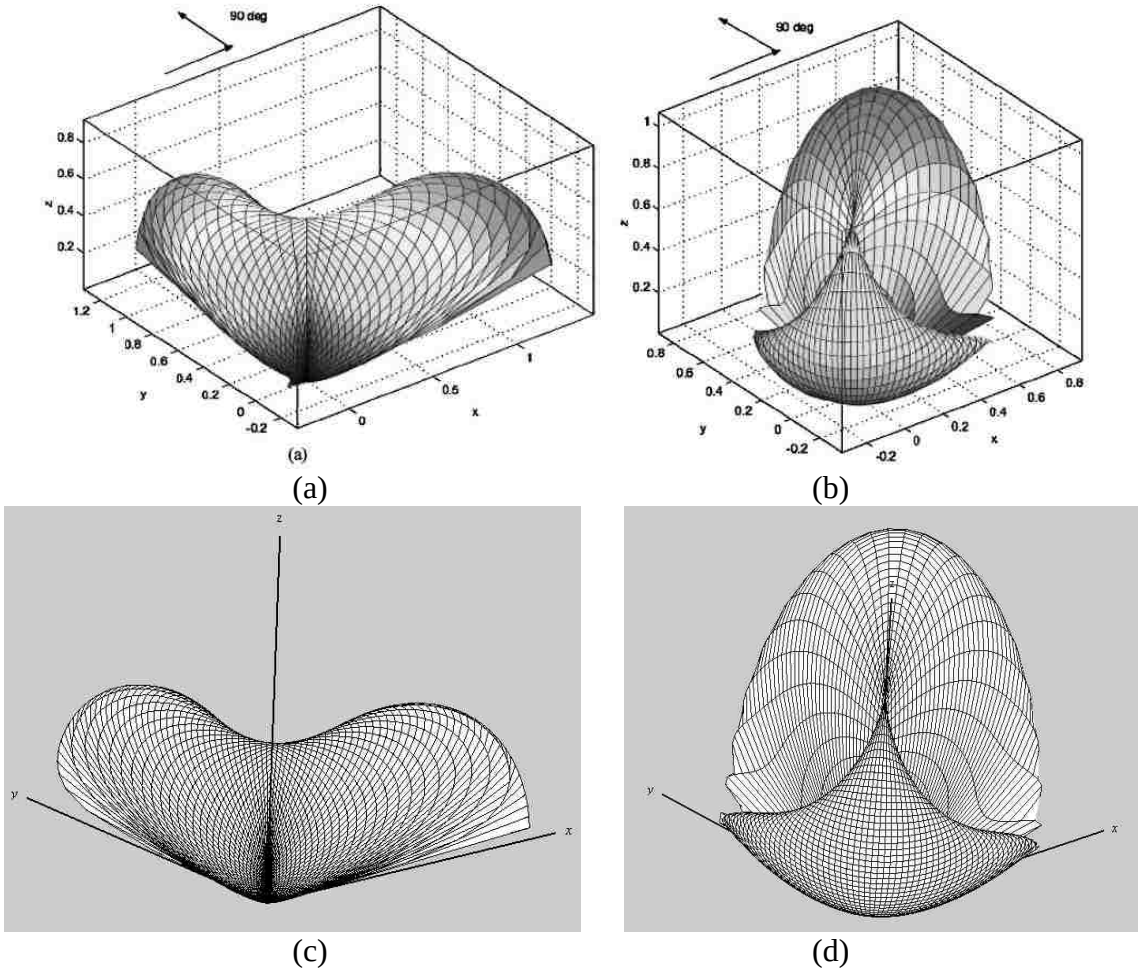

Fig. 20. Comparison of 3D radiation pattern contributed by 90 °bends at 1 GHz. (a) $|\boldsymbol{E}_{\theta}|$ in paper [32], (b) $|\boldsymbol{E}_{\varphi}|$ in paper [32], (c) $|\boldsymbol{E}_{\theta}|$ calculated in this paper with (6), (10) and (11), (d) $|\boldsymbol{E}_{\varphi}|$ caclulated in this paper with (6), (10) and (11).

2D views of the radiated field pattern from the 90 °bends in paper [33] are shown in Fig. 21 (a) and (b) using the reflection and transmission coefficients calculated with TWM. The results were reproduced in this paper, as shown in Fig. 21 (c). When the reflection coefficient was set to be zero, and the transmission coefficient was set to be one (11), the 2D radiated field pattern is shown in Fig. 21 (d).

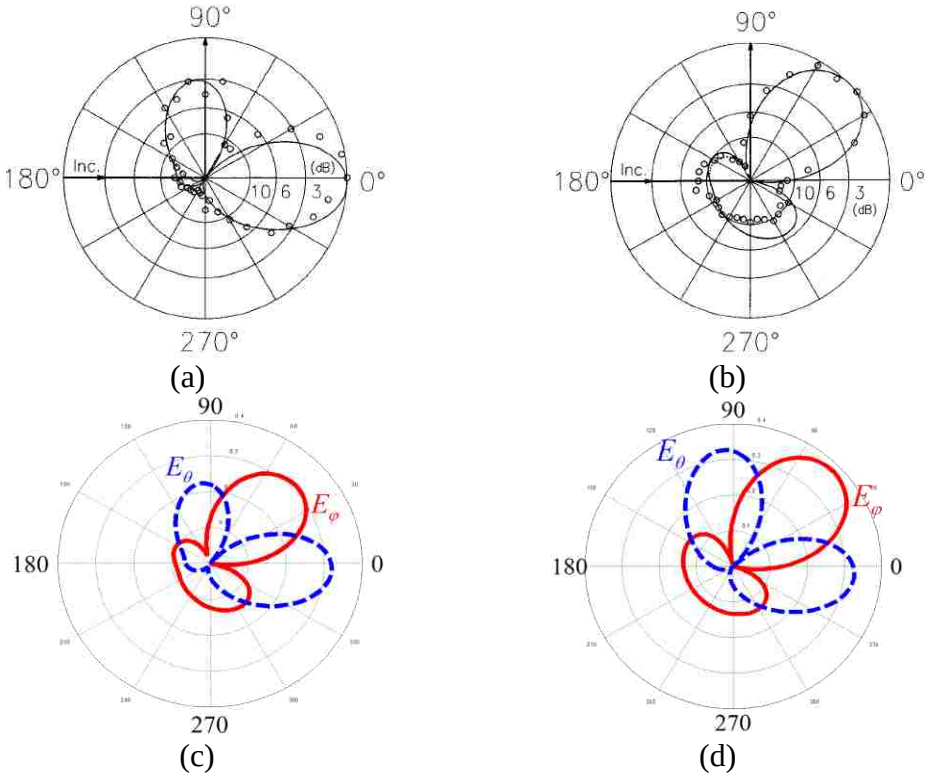

Fig. 21. Comparison of 2D radiation pattern contributed by 90 °bends at 2 GHz. (a) $|\boldsymbol{E}_\theta|$ in paper [33], (b) $|\boldsymbol{E}_\varphi|$ in paper [33], (c) $|\boldsymbol{E}_\theta|$ and $|\boldsymbol{E}_\varphi|$ reproduced with the method in paper [33], (d) $|\boldsymbol{E}_\theta|$ and $|\boldsymbol{E}_\varphi|$ caclulated in this paper with (6), (10) and (11).

With the approximation of reflection and transmission coefficients in (11), there is almost no difference in radiated field patterns compared to the results calculated with the actual current distributions on the wires with right-angle bends.

For two finitely long bent wires, there are six physical discontinuities, four at the ends of the wires and two at the bends. With the approximation in (11), there are eight current discontinuities that need to be summed up in the calculation with the steepest descent method, four at the two bends and four at the ends of the wires, as shown in Fig. 22. TRP was calculated and compared to the results with the Green's function method, as shown in Fig. 12 (b). The current distributions used in the Green's function method were extracted from EMC studio (MoM). There is almost no difference in TRP comparison.

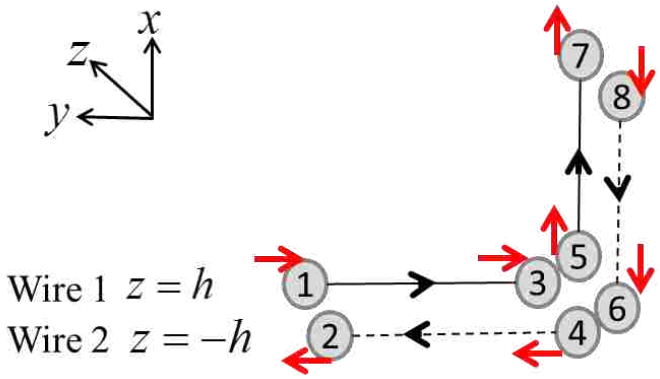

Fig. 22. Eight current discontinuities in the 90 °bent wire for the calculation of TRP with steepest descent method.

Therefore, from a radiation point of view, it is not necessary to calculate the reflection and transmission coefficients at the bends.

The analysis of radiation from bent wires with the Green's function method and the steepest descent method illustrate that the increased radiated power from bent wires is because of the location change of the current discontinuities at bends in reference to the straight wires, and that the contribution from the small variance in the current distribution caused by the reflection at the bends can be neglected. The calculation of radiated power with the steepest descent method is more efficient because it only needs to sum up several discontinuities in the structure, yet the calculation with Green's function method is the integration of the currents along the entire length of the wires.

Based on the physics of radiation from bent wires, the second connector design guideline for EMI suppression from TL mode current is proposed: Optimization of the reflection at the bends does not help to reduce radiation, and TRP decreases approximately 3 dB with the bend feature removed.

7. MISMATCH INFLUENCE ON TRP

Radiation from a two-wire transmission line with travelling wave currents was analyzed in the previous sections. In real world designs, it is difficult to have a good match for the transmission line over a broadband frequency range because of via transitions and discontinuities in the structure. Radiation contributed by mismatch at the two ends of the straight wires is analyzed in this section. The configuration and the coordinates are shown in Fig. 23.

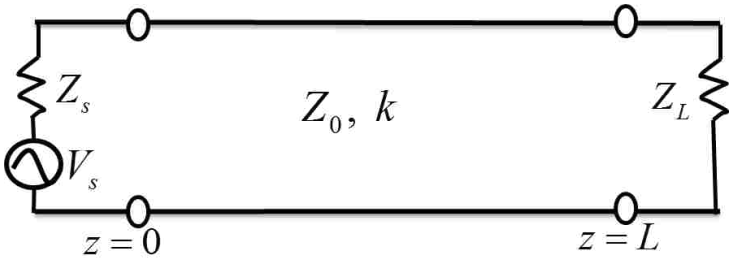

Fig. 23. Straight two-wire transmission line and the coordinates.

The source impedances Z_S and load impedances Z_L were chosen to be 10 Ω as an example. The characteristic impedance of the wires, Z_0, is 192.5 Ω. The TRP result calculated with Green's function method was compared to the case when the source and load impedance matched Z_0, as shown in Fig. 24. TRP increased dramatically at $\lambda/2$ resonances when there was a mismatch at both ends of the two-wire transmission line because of the significantly increased current magnitude, as shown in Fig. 25, of the current comparison at 3 GHz which corresponds to one wavelength of the wire.

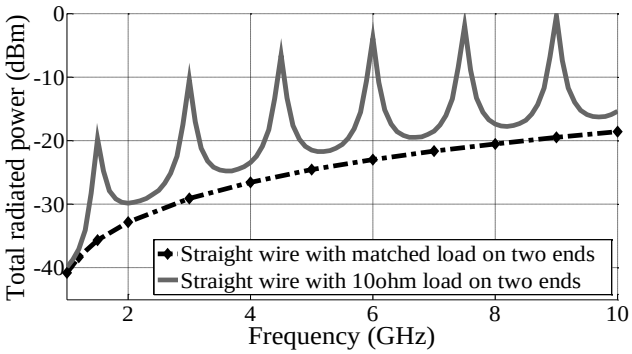

Fig. 24. TRP comparison with mismatched source and load (10 Ω) impedances and matched source and load impedances.

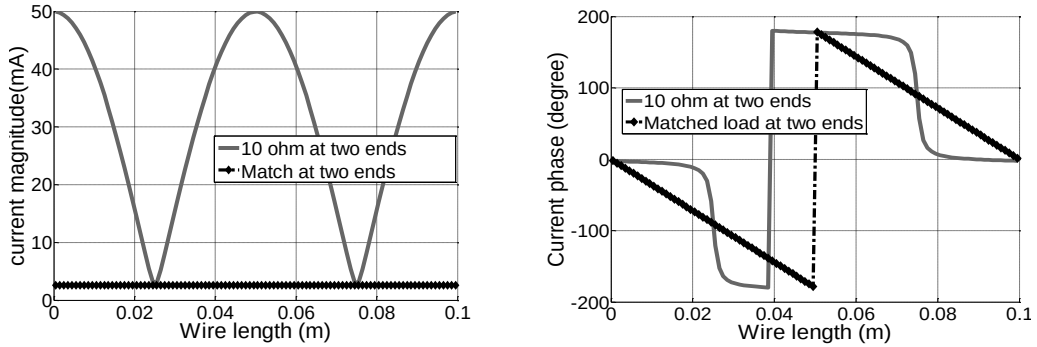

(a) (b)

Fig. 25. Current distribution at 3 mismatched source and load (10 Ω) impedances and matched source and load impedances. (a) Current magnitude comparison, (b) current phase comparison.

The current and voltage distributions on the two-wire transmission line are

$$I(z) = I^{+}e^{-jkz}(1-\Gamma_L e^{-2jk(L-z)}) \tag{12}$$

$$V(z) = V^{+}e^{-jkz}(1+\Gamma_L e^{-2jk(L-z)}) \tag{13}$$

where

$$\Gamma_L = \frac{Z_L - Z_0}{Z_L + Z_0} \tag{14}$$

and L is the wire length, V_S is a constant source voltage, I is the total current on the transmission line, I^+ is the RGW current, and Γ_L is reflection coefficient looking into the load.

The voltage at source end of the line is

$$V_0 = V(z=0) = V^+(1+\Gamma_L e^{-2jkL}) = \frac{Z_{in}}{Z_{in}+Z_s}V_s \tag{15}$$

At $\lambda/2$ resonances,

$$Z_{in} = Z_L,\ kL = n\pi \tag{16}$$

Then the RGW voltage and current waves are

$$V^+ = \frac{Z_L}{(Z_L+Z_s)(1+\Gamma_L)}V_s \tag{17}$$

$$I^+ = \frac{V^+}{Z_0} = \frac{V_s}{Z_0}\frac{1}{\left(1+\frac{Z_s}{Z_L}\right)}\frac{1}{(1+\Gamma_L)} \tag{18}$$

where Γ_S is the reflection coefficient looking into the source:

$$\Gamma_s = \frac{Z_s - Z_0}{Z_s + Z_0} \tag{19}$$

From (12) and (18), it is shown that the total current on the transmission line is related to both Z_L and Z_S. TRP changes with different Z_L and Z_S, which determines Γ_L and Γ_S. At 9 GHz, which is one of the $\lambda/2$ resonances, the radiation was calculated with different Γ_L, as shown in Fig. 26 (a). The different curves show the different Γ_S. TRP is determined by I^+, which is dominated by two factors: $1/\left(1+\frac{Z_S}{Z_L}\right)$ and $\frac{1}{1+\Gamma_L}$. When $Z_S < Z_0$, TRP is dominated by $\frac{1}{1+\Gamma_L}$ and decreases when Γ_L increases approximately; when $Z_S \geq Z_0$, TRP is dominated by $1/\left(1+\frac{Z_S}{Z_L}\right)$, TRP increases as Z_L increases. In real product design, normally $|\Gamma_L|$ and $|\Gamma_S|$ are smaller than 0.5. At 8.25 GHz, which is odd harmonics of the $\lambda/4$ resonances, the radiation was calculated with different Γ_L and Γ_S, as shown in Fig. 26 (b). A similar analysis can be performed, and the relationship of TRP to Γ_L and Z_L is opposite, since

$$Z_{in} = Z_0^2 / Z_L \ , \ kL = (2n+1)\pi \tag{20}$$

and

$$I^+ = \frac{V^+}{Z_0} = \frac{V_s}{Z_0} \frac{1}{\left(1+\frac{Z_s Z_L}{Z_0^2}\right)} \frac{1}{(1-\Gamma_L)} \tag{21}$$

Therefore, the third connector design guideline is proposed to suppress radiation at $\lambda/2$ resonances: when$Z_S \geq Z_0$, it is not necessary to consider EMI problems; when $-0.5 < \Gamma_S \leq 0$ and $|\Gamma_L| < 0.5$, the change of TRP is less than 5 dB. Similar conclusions can be drawn at odd harmonics of the $\lambda/4$ resonances, however, the trend of TRP to Γ_L and Z_L is opposite.

Considering the mismatch at the ends of the two-wire transmission line, the standing wave currents on the wires can be decomposed into RGW and left going waves (LGW):

$$I = AI_0 e^{-j\beta\xi}(RGW) + BI_0 e^{j\beta\xi}(LGW) \tag{22}$$

where *A* and *B* are the coefficients determined by the load and source impedances.

The radiated fields caused by the LGW currents on the wires were derived with the steepest descent method:

$$\boldsymbol{H}^{rad} \approx \sum_{i=1}^{N} \frac{\boldsymbol{j}_i \times \boldsymbol{j}_r}{\beta/k + \boldsymbol{j}_i \cdot \boldsymbol{j}_r} e^{j\beta\xi_i} \frac{e^{-jkr} e^{jk(\boldsymbol{d}_i \cdot \boldsymbol{j}_r)}}{4\pi r} U_i I_i \tag{23}$$

TRP from the standing wave current was calculated with (6) and (22)-(23), and was then compared to the results calculated with Green's function method, as shown in Fig. 27. $A = B = 1$ is assumed here as an example. So with any type of currents on the wires, the radiation can be calculated from the discontinuities in the two-wire transmission line with the steepest descent method.

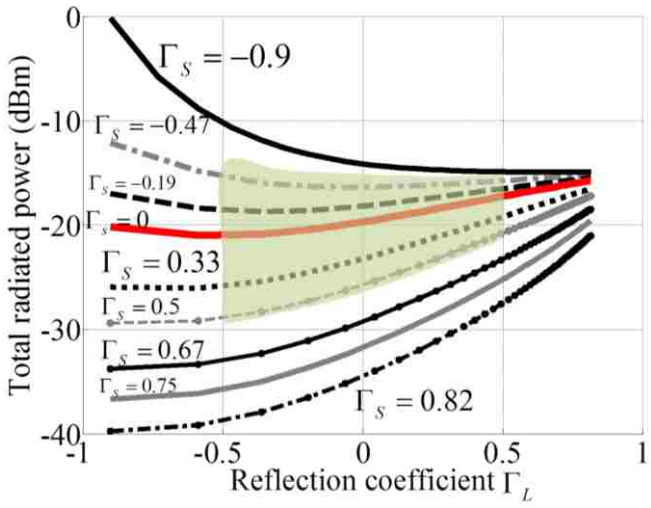

(a)

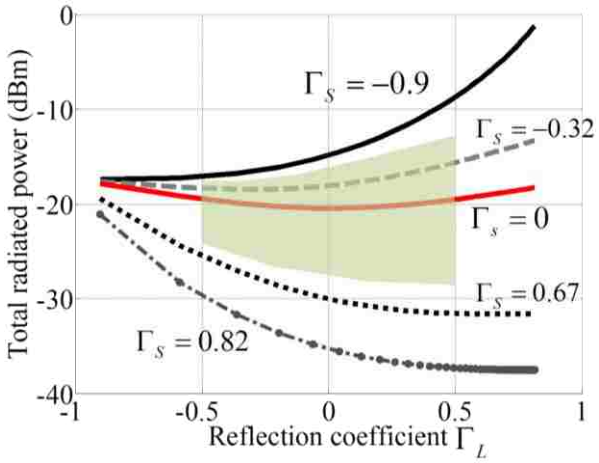

(b)

Fig. 26. The change of TRP with different load and source impedances of straight two-wire transmission line (a) At 9 GHz, (b) at 8.25 GHz.

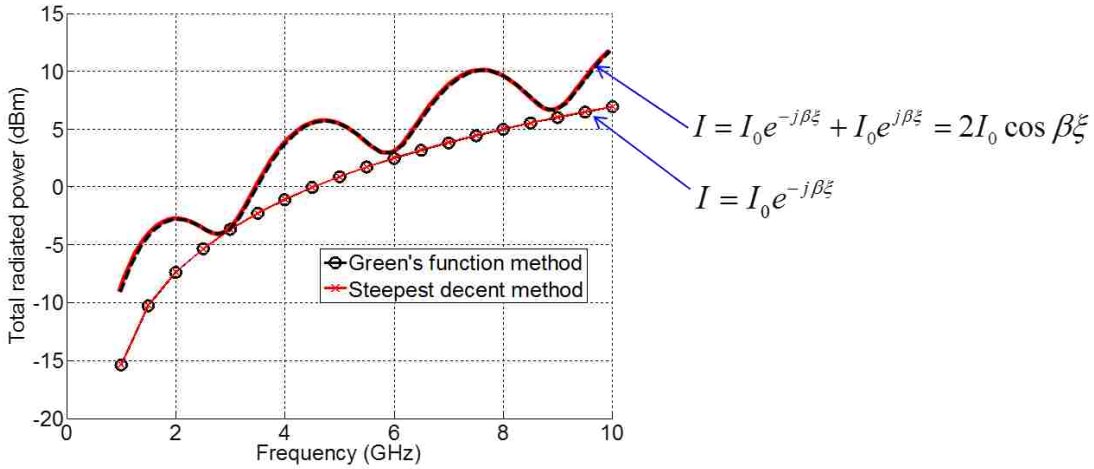

Fig. 27. TRP comparison of steepest descent method and Green's function method with travelling wave current and standing wave currents.

8. CONNECTOR DESIGN GUIDELINES FOR EMI MITIGATION

Based on the analysis of radiation physics of high-speed connectors, several connector design guidelines for EMI mitigation were proposed. To suppress radiation caused by the antenna mode current, the signal conductors should have well-referenced nearby ground conductors for the return currents. The antenna mode current on the connector structure can be reduced proportionally to the decrease of the difference of the imbalance factor of the PCB connected to the connector and the imbalance factor of the connector, when the TL mode current does not change. To suppress the radiation from TL mode currents, TRP decreases 20 dB/decade when the separation of two wires decreases in the range of less than $\lambda/2$. Optimization of the reflection at bends does not help to reduce radiation, TRP decreases approximately 3 dB with the bend feature removed. With mismatch at both ends of the transmission line, it is not necessary to consider EMI problems when$Z_S \geq Z_0$; if $-0.5 < \Gamma_S \leq 0$ and $|\Gamma_L| < 0.5$, the change of TRP is less than 5 dB at $\lambda/2$ resonances. Similar conclusions can be drawn at odd harmonics of the $\lambda/4$ resonances, however, the trend of TRP to Γ_L and Z_L is opposite.

9. CONCLUSIONS

Radiation from antenna mode current and TL mode current was illustrated with backplane connectors and optical cage connectors. The radiation from the high-speed connector with TL mode current was analyzed in detail. The possible radiation mechanisms were analyzed with the Green's function method, the steepest descent method, and EMC studio (MoM). The contribution of end-wire effect to TRP is less than 2 dB when the wire separation is larger than one hundredth of the wavelength. The radiation from straight two-wire transmission line is due to the finite length, which brings in the four discontinuities at two ends of the wires. TRP decreases 20 dB/decade when the separation of two wires is smaller than $\lambda/2$, TRP does not change much as the wire length is larger than $\lambda/2$. The increased radiated power from bent wires is because of the location change of the current discontinuities at the bends in reference to the straight wires, while the contribution from the small variance in the current distribution caused by the reflection at bends can be neglected. Because of via transitions and discontinuities at two ends of the transmission line, the radiation contributed by mismatch effect was analyzed at harmonics of quarter-wavelengths. The steepest descent method revealed the radiation physics, and it is an efficient way to calculate radiation from two-wire transmission line with any type of current distribution, since it only sums up the radiated fields from the discontinuities in the structure. To suppress the radiation from antenna mode current and TL mode current on the structure, EMI design guidelines for high-speed connectors were proposed, based on the analyzed radiation physics.

REFERENCES

[1] X. Tian, M. S. Halligan, X. Li, K. Kim, H.-C. Chen, S. Connor, B. Archambeault, M. Cracraft, A. E. Ruehli, and J. L. Drewniak, "Modeling electromagnetic radiation at high-density PCB/connector interfaces," in Proc. 2014 IEEE Int. Symp. Electromagn. Compat., Raleigh, NC, USA, Aug. 2014, pp. 97-102.
[2] Jing Li, Xiao Li, Sukhjinder Toor, Hongmei Fan, Alpesh Bhobe, Jun Fan, James L. Drewniak, " EMI Coupling Paths and Mitigation in a Board-to-Board Connector," to be published IEEE Trans. Electromagn. Compat., vol., no., pp., 2015.
[3] Vukicevic, A., Rachidi, F., Rubinstein, M., Tkachenko, S.V., "On the Evaluation of Antenna-Mode Currents Along Transmission Lines," IEEE Trans. Electromagn. Compat., vol.48, no.4, pp.693-700, Nov. 2006.
[4] Khee, Y.S.; Zarar Mohamed Jenu, M., "Radiated emission of bent microstrip line using Hertzian dipole method," in Proc. 2008 IEEE Int. Symp. Electromagn. Compat., Detroit, MI, USA, Aug. 2008, pp.1-6.
[5] Toki, H., Sato, K., "Multiconductor Transmission-Line Theory with Electromagnetic Radiation", Trans. Physical Society of Japan, vol. 81, no. 1, pp.014-201, 2012.
[6] F. M. Tesche, M. V. Ianoz, and T. Karlsson, EMC Analysis Methods and Computational Models. New York: Wiley, 1997.
[7] C. R. Paul, Analysis of Multiconductor Transmission Lines. NewYork: Wiley, 1994.
[8] S. Frankel, Quasi-TEM Transmission Line Theory, Interaction Note 135, Nov. 1972.
[9] K. S. H. Lee, "Two parallel terminated conductors in external fields," IEEE Trans. Electromagn. Compat., vol. EMC-20, no. 2, May 1978.
[10] C. R. Paul, "A comparison of the contributions of common-mode and differential-mode currents in radiated emissions," IEEE Trans. Electromagn. Compat., vol. 31, no. 2, pp. 189–193, May 1989.
[11] M. Leone, and V. Navrátil, "On the electromagnetic radiation of printed-circuit-board interconnections," IEEE Trans. Electromagn. Compat., vol. 47, no. 2, pp. 219-226, May 2005.
[12] M. Torigoe, A. Sadatoshi, Y. Toyota, K. Iokibe, R. Koga, T. Watanabe, and O. Wada, "Prediction of the common-mode radiated emission from the board to board interconnection through common-mode antenna model," in Proc. 2008 IEEE Int. Symp. Electromagn. Compat., Detroit, MI, USA, Aug. 2008, pp. 1- 4.
[13] Y. Toyota, A. Sadatoshi, T. Watanabe, K. Iokibe, R. Koga, and O. Wada, "Prediction of electromagnetic emissions from PCBs with interconnections through common-mode antenna model," in 2007 Int. Zurich Symp. Electromagn. Compat., Munich, Germany, Sept. 2007, pp.107-110.
[14] B. Archambeault, S. Connor, M. S. Halligan, J. L. Drewniak, and A. E. Ruehli, "Electromagnetic radiation resulting from PCB/high-density connector interfaces," IEEE Trans. Electromagn. Compat., vol. 55, no.4, pp. 614-623, Aug. 2013.
[15] L. K. C. Wong, "Backplane connector radiated emission and shielding effectiveness," in Proc. 1992 IEEE Int. Symp. Electromagn. Compat., Anaheim, CA, USA, Aug. 1992, pp. 346–351.

[16] Z. Li, P. Yu, and C.-P. Chua, “The EMI characteristics of high speed backplane connector,” in Proc. 2012 Int. Symp. Electromagn. Compat., Rome, Italy, Sep. 2012, pp. 1-4.
[17] H. C. Chen, S. Connor, T. L. Wu, B. Archambeault, “The effect of various skew compensation strategies on mode conversion and radiation from high-speed connectors,” in Proc. 2013 IEEE Int. Symp. Electromagn. Compat., Denver, CO, USA, Aug. 2013, pp. 328–332.
[18] H. Fan; X. Zhou; A. Bhobe, J. Yu; H. Zhang, and P. Sochoux, “An analytical approximation for evaluating impact of skew length on radiated emission from differential signal pairs,” in Proc. 2012 Asia-Pacific Symp. Electromagn. Compat. (APEMC), Singapore, May 2012, pp. 673-676.
[19] P. Sochoux, M. Hsu, A. Bhobe, and J. Yu, “EMI from SerDes differential pairs,” Designcon 2009, Santa Clara, CA, USA, Jan., 2009.
[20] X. Duan, B. Archambeault, H.-D. Bruens, C. Schuster, “EM emission of differential signals across connected printed circuit boards in the GHz range,” in Proc. 2009 IEEE Int. Symp. Electromagn. Compat., Austin, Tx, USA, Aug. 2009, pp. 50-55.
[21] Liu, Y.W.; Mei, K.K.; Hong, J.S., “Radiation extraction for transmission-line interconnects,” in Proc. 2001 IEEE Int. Symp. Antennas and Propagation Society, Boston, MA, July 2001, vol.1, pp.580-583.
[22] Nitsch J, Gronwald F,Wollenberg G, “Radiating nonuniform transmission-line systems and the partial element equivalent circuit method,” Wiley, Chichester, 2009.
[23] Sungkyu Lee, Hayakawa, M., “A study on the radiation loss from a bent transmission line,” IEEE Trans. Electromagn. Compat., vol.43, no.4, pp.618-621, Nov 2001.
[24] Kayano, Y.; Tsuda, Y.; Inoue, H., “Identifying EM radiation from asymmetrical differential-paired lines with equi-distance routing,” in Proc. 2012 IEEE Int. Symp. Electromagn. Compat., Pittsburgh, PA, USA, Aug. 2012, pp.311-316.
[25] Nitsch, J.B., Tkachenko, S.V., “Complex-valued transmission-line parameters and their relation to the radiation resistance,” IEEE Trans. Electromagn. Compat., vol.46, no.3, pp.477-487, Aug. 2004.
[26] Maffucci, A.; Miano, G.; Villone, F., “An enhanced transmission line model for conducting wires,” IEEE Trans. Electromagn. Compat., vol.46, no.4, pp.512-528, Nov. 2004.
[27] Jing Li, Yaojiang Zhang, Dazhao Liu, Alpesh Bhobe, James L. Drewniak, Jun Fan “Radiation Physics from Two-Wire Transmission Line,” in Proc. 2015 IEEE Int. Symp. Electromagn. Compat., Santa Clara, CA, USA, Mar. 2015, pp.160-164.
[28] Wang, H.; Ji, Y.; Hubing, T.H.; Drewniak, J.L.; Van Doren, T.P.; DuBroff, R.E., “Experimental and numerical study of the radiation from microstrip bends,” in Proc. 2000 IEEE Int. Symp. Electromagn. Compat., Washington, DC, USA, Aug. 2000, vol.2, pp.739-741.
[29] Liu, Y.W and Zhao, D.S., “Generalized non-uniform transmission-line models for local radiation from microstrip bends in MMICs,” Int. J. Numer. Model: Electronic Networks, Devices and Fields, vol.16, no. 3, pp.261-269, Jun. 2003.
[30] Leone, M., “Closed-Form Expressions for the Electromagnetic Radiation of Microstrip Signal Traces,” IEEE Trans. Electromagn. Compat., vol.49, no.2, pp.322-328, May 2007.

[31] Xilei Liu, Christopoulos, C., Thomas, D.W.P., "Prediction of radiation losses and emission from a bent wire by a network model," IEEE Trans. Electromagn. Compat., vol.48, no.3, pp.476-484, Aug. 2006.
[32] Nakamura, T., Hayashi, N., Fukuda, H., Yokokawa, S., "Radiation from the transmission line with an acute bend," IEEE Trans. Electromagn. Compat., vol.37, no.3, pp.317-325, Aug 1995.
[33] Nakamura, T., Yokokawa, S., Kamiya, S., "Transmission and radiation properties of a surface wave transmission line with a bend," Electronics and Communications, Japan, vol.77, no.5, part 1, 1994.
[34] Tomiyasu, K., "The Effect of a Bend and Other Discontinuities on a Two-Wire Transmission Line," in Proc. of the IRE, June 1950, vol.38, no.6, pp.679-682.
[35] Lin-Sheng Wu, Jun-Fa Mao, Wen-Yan Yin, "Slow-wave structure to suppress differential-to-common mode conversion for bend discontinuity of differential signaling," in Proc. 2012 IEEE Electrical Design of Advanced Packaging and Systems Symposium (EDAPS), Taipei, China, Dec. 2012, pp.219-222.
[36] Khee, Y.S., Zarar Mohd Jenu, M., "Magnetic and electric field radiation of bent microstrip line using Hertzian dipole method," in Proc. 2008 IEEE Int. RF and Microwave Conference, Kuala Lumpur, Dec. 2008, pp.31-35.
[37] Guang-Hwa Shiue, Wei-Da Guo, Chien-Min Lin, Wu, Ruey-Beei, "Noise reduction using compensation capacitance for bend discontinuities of differential transmission lines," IEEE Trans. Advanced Packaging, vol.29, no.3, pp.560-569, Aug. 2006.
[38] B. Archambeault, J. C. Diepenbrock, S. Connor., "EMI Emissions from Mismatches in High Speed Differential Signal Traces and Cables," in Proc. 2007 IEEE Int. Symp. Electromagn. Compat., Honolulu, HI, Jul. 2007, pp.1-6.
[39] T. Watanabe, O. Wada, T. Miyashita, and R. Koga, "Common-modecurrent generation caused by difference of unbalance of transmission lines on a printed circuit board with narrow ground pattern," IEICE Trans. Commun., vol. E83-B, no. 3, pp. 593–599, Mar. 2000.
[40] T. Watanabe, S. Matsunaga, O. Wada, M. Kishimoto, T. Tanimoto, A. Namba, and R. Koga, "Equivalence of two calculation methods for common-mode excitation on a printed circuit board with narrow ground plane," in Proc. IEEE Int. Symp. Electromagn. Compat., Boston, MA, Aug. 2003, pp. 22–27.
[41] T. Watanabe, H. Fujihara, O. Wada, and R. Koga, "Prediction method of common-mode excitation on a printed circuit board having a signal trace near the ground edge," IEICE Trans. Commun., vol. E87-B, no. 8, pp. 2327–2334, Aug. 2004.
[42] Y. Toyota, T. Matsushima, K. Iokibe, R. Koga, and T. Watanabe, "Experimental validation of imbalance difference model to estimate commonmode excitation in PCBs," in Proc. IEEE Int. Symp. Electromagn. Compat., Detroit, MI, Aug. 2008, pp. 1–6.
[43] T. Matsushima, T. Watanabe, Y. Toyota, R. Koga, and O. Wada, "Prediction of EMI from two-channel differential signaling system based on imbalance difference model," in Proc. IEEE Int. Symp. Electromagn. Compat., Fort Lauderdale, FL, Jul. 2010, pp. 413–418.

[44] C. Su and T. Hubing, “Imbalance difference model for common-mode radiation from printed circuit boards,” IEEE Trans. Electromagn. Compat., vol. 53, no. 1, pp. 150–156, Feb. 2011.
[45] C. Su and T. Hubing, “Improvements to a method for estimating the maximum radiated emissions from PCBs with cables,” IEEE Trans. on Electromagnetic Compatibility, vol. 53, no. 4, Nov. 2011, pp. 1087- 1091.
[46] Toyota, Y., Iokibe, K., Koga, L.R., “Mode conversion caused by discontinuity in transmission line: From viewpoint of imbalance factor and modal characteristic impedance,” in Proc. 20013 IEEE Electrical Design of Advanced Packaging and Systems Symp. (EDAPS), Nara, Dec. 2013, pp.52-55.
[47] Y. Toyota, K. Iokibe, R. Koga, and T. Watanabe, “Mode-equivalent modelling of system consisting of transmission lines with different imbalance factors,” in Proc. Asia-Pacific Int. Symp. Electromagn. Compat., pp.676-679, May 2011.
[48] Tohlu Matsushima, Tetsushi Watanabe, Yoshitaka Toyota, Ryuji Koga and Osami Wada, “Evaluation of EMI reduction effect of guard traces based on imbalance difference method,” IEICE Trans. Commun., vol. E92-B, no. 6, pp. 2193-2200, Jun. 2009.
[49] Kwak, H., Hubing, T.H., “Investigation of the imbalance difference model and its application to various circuit board and cable geometries,” in Proc. 2012 IEEE Int. Symp. Electromagn. Compat., Pittsburgh, PA, USA, Aug. 2012, pp.273-278.
[50] Hwan W. Shim and Todd H. Hubing, “Derivation of a closed form approximate expression for the self-capacitance of a printed circuit board trace,” IEEE Trans. Electromag. Compat., vol. 47, no. 4, pp. 1004-1008, Nov. 2005.
[51] C. Balanis, Antenna Theory, Analysis, and Design, 2nd ed. New York: Wiley, 1997.
[52] C. H. Walter, Traveling Wave Antennas, McGraw-Hill, New York, 1965.

III. EMI Reduction Evaluation for Absorbing Materials on Cables with a 2D Finite Element Approach

Jing Li, *Student Member, IEEE,* Yaojiang Zhang, Shenhui Jing, Jun Fan, *Senior Member, IEEE,* James Drewniak, *Fellow, IEEE*

Abstract—Taking the advantage of the axially symmetric structure, the 2D finite element method (2D FEM) was developed to analyze electromagnetic interference (EMI) reduction when magneto-dielectric absorbing materials were applied to cables, which is much less time- and memory-consuming compared to a 3D numerical simulation. The 2D FEM formulation was verified by comparison to a 3D full-wave simulation and measurements performed in an anechoic chamber. With the developed 2D FEM, radiated power and input impedance were calculated efficiently to evaluate the EMI reduction with different absorbing materials applied to cables. To give insightful guidelines to the engineers who use absorbing materials as a mitigation approach to suppress the EMI from cables, cables with different diameters, lengths, and source impedances were also analyzed

Index Terms—Two-dimensional finite element method, edge-based element, absorbing materials, cable radiation, EMI reduction

1 INTRODUCTION

Electromagnetic interference (EMI) is a disturbance that affects an electrical circuit because of electromagnetic conduction or electromagnetic radiation emitted from an external source. One of the weakest points in many designs, from an EMI point of view, is the amount of electromagnetic noise energy that can escape from the system equipment enclosure along cables attached to the system [1-4]. Some of the energy will propagate as the differential mode (forth on one cable, back on another), and the rest as the common mode (along all of the cables simultaneously and back via an unknown "ground" return) [5-8]. A well-behaved current on a cable, like the differential mode current, has “balanced” signal direct and return currents. At the same time, if the shielding of the cable is not good or there is mismatch at two ends of the cable, the currents that go down the cable as conduction currents and their “return” counterparts (like the common mode current) will radiate as displacement currents, as shown in Fig. 1. Both propagation mechanisms will radiate in the outside world and can interfere with any other piece of electronic equipment. It has been shown by Delogne [9] that the fields caused by common mode noise are much greater than those from differential mode for the same current.

Ferrite cores or flexible absorbing materials can be applied on cables to suppress common mode noise radiation. The radiation from a cable carrying a common mode current shown in Fig. 1 is equivalent to the radiation from a monopole antenna over a ground plane, as is shown in Fig. 2. Therefore, the estimation of EMI reduction on cables due to absorbing materials or ferrite cores has been converted to the analysis of a monopole antenna with different coating materials.

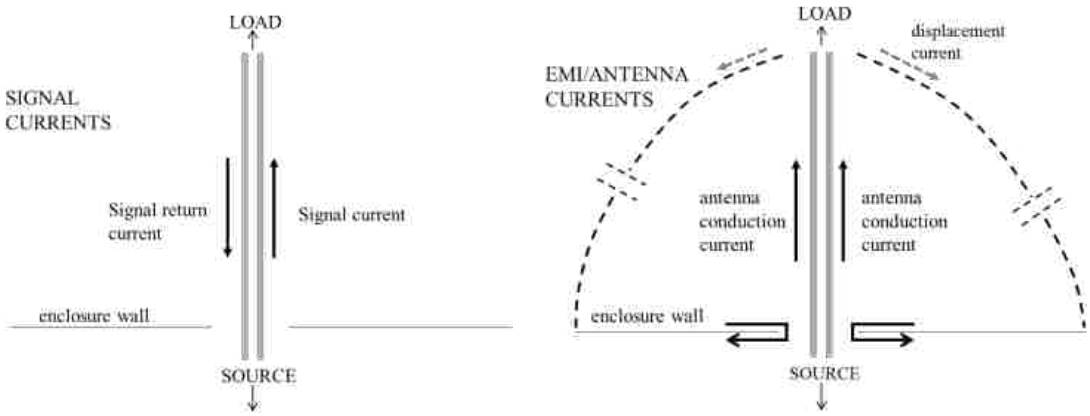

(a) (b)

Fig. 1. Differential mode and common mode signal currents on cables. (a) With differential mode current, (b) with common mode current.

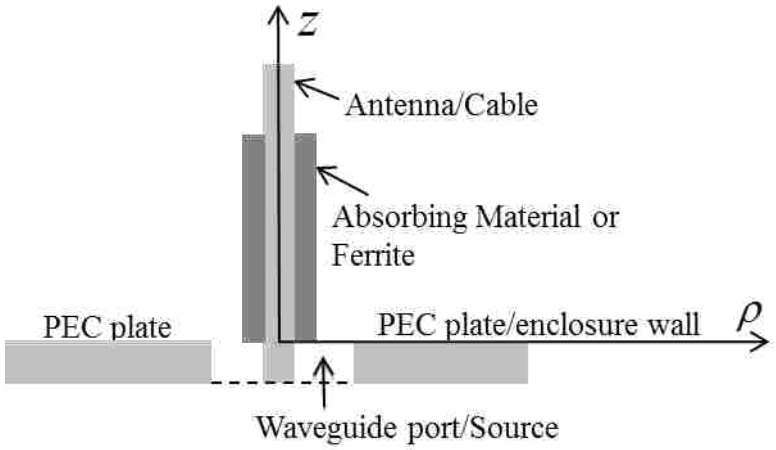

Fig. 2. A monopole antenna used to imitate the common mode current on a cable.

Some papers use the finite-difference time-domain (FDTD) method to characterize the absorption performance of magneto-dielectric layers [10]-[13]. The disadvantage of FDTD for dispersive material modeling is that relative permittivity and permeability as functions of frequencies should be represented as sums of rational-fractional functions [12]. Fitting the measured data to the sums of the Debye or Lorentzian terms with physically meaningful parameters needs special optimization procedures, e.g., genetic

algorithms, [13] or nonlinear regression analysis [14]. In contrast, as a frequency-domain solver, the finite element method (FEM) is very convenient for any dispersive materials with material parameters in a look-up table changing with frequencies.

On the other hand, the thickness of absorbing materials applied to cables is usually less than 1 mm, or the gap between the ferrite core and cable is less than 0.5 mm, while the cable length might be in meters. Therefore, to mesh the materials or the gap well for the long cable geometry at frequencies up to 10 GHz, it is very time- and memory-consuming for the 3D FEM to evaluate the EMI reduction from the absorbing materials. Taking the advantage of the axially symmetric structure, as in Fig. 2, a 2D FEM method was developed to calculate the radiated power reduction due to the coating materials around a cable.

The main objective of this paper is to provide an efficient approach to estimate the EMI suppression performance with absorbing materials along cables based on 2D FEM, and to give insightful guidelines to engineers for using absorbing materials as mitigation approaches on different cables. The algorithms and formulations of 2D FEM to calculate radiation power and input impedance are detailed in Section II. The verification of 2D FEM is demonstrated in Section III with comparison to commercial numerical software (CST Microwave Studio) and the measurement results. The EMI reduction with different absorbing materials on cables were evaluated with 2D FEM in Section IV, and the structures with different cable diameters, cable lengths and source impedances were also studied.

2 2DFEM ALGORITHMS AND FORMULATION

Because of the azimuthal symmetry of the monopole antenna model with infinite large ground plane, only half of the calculation domain in two dimensions needs to be considered. Fig. 3 shows the 2D FEM set-up of a cross section of a monopole antenna coated by absorbing materials with relative permittivity and permeability of ε_r, μ_r in region 2. The light grey region stands for a perfect electrical conductor (PEC). Regions 3, 4 and 5 are air, and perfectly matched layers (PML) are in regions 6, 7 and 8, which are terminated by PEC boundary conditions. PML is used to absorb the energy reaching the boundaries of the calculation domain to mimic the free space. Note that the perfectly magnetic conductor (PMC) boundary is set to the edge of $L < Z < L + A_z + t_z$, $\rho = 0$. This is because the structure is azimuthally symmetric, and there is no normal electric field crossing the edge for the rotationally symmetric structure. Waveguide port is set in region 1 with known H field on the boundary to model the feeding coaxial connector, and $\varepsilon_1 = 2.1$ for 50 Ω source impedance.

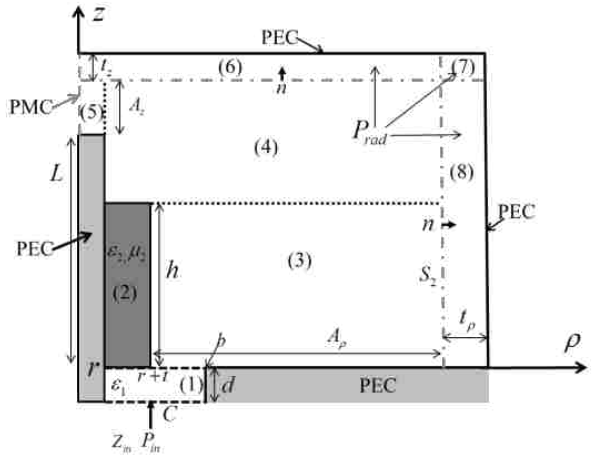

Fig. 3. The 2D FEM solution domain for a monopole antenna coated by an absorbing material in a polar coordinate system.

With Galerkin's method, the weak form for the problem is shown as [15]

$$\int_S [\nabla \times \boldsymbol{W_i^e} \cdot u_r^{-1} \bar{\bar{\Lambda}}^{-1} \cdot \nabla \times \boldsymbol{E^e} - k_0^2 \varepsilon_r \boldsymbol{W_i^e} \cdot \bar{\bar{\Lambda}} \cdot \boldsymbol{E}^e] \rho dS + jk_0 \eta_0 \int_C \boldsymbol{W_i^e} \times \boldsymbol{H}^e \cdot \mathbf{n} \rho dl = 0 \tag{1}$$

where W_i^e is the trial (interpolation) function, which is also the edge basis function (detailed in appendix I), $\eta = 120\pi\,\Omega$ is the free space wave impedance, k_0 is the wave number in the free space, ρ is the radial coordinate, and $\bar{\bar{\Lambda}}$ is a unit matrix in all the regions, except for the PML regions [15]. Note that the second integral vanishes along PEC and PMC boundaries, and waveguide port is set along the boundary *C* in region 1 with known *H* field as the source exciting the structure.

E field in each element/triangle can be expressed by the *E* field on each edge with basis function as

$$\boldsymbol{E}^e(x,y,z) = \sum_{i=1}^{3} \boldsymbol{W}_i^e(x,y,z) E_i^e \tag{2}$$

Substituting (2) into (1), the element matrix equation can be derived as

$$\left[K^e\right]\left[E^e\right] = \left[b\right] \tag{3}$$

where

$$K^e{}_{ij} = \int_{S_e} [\nabla \times \mathbf{W}_i^e \cdot \mu_r^{-1} \bar{\bar{\Lambda}}^{-1} \cdot \nabla \times \mathbf{W}_j - k_0^2 \varepsilon_r \mathbf{W}_i^e \cdot \bar{\bar{\Lambda}} \cdot \mathbf{W}_j] \rho d\rho dz \tag{4}$$

$$b_i = -jk_0\eta_0 \int_C \boldsymbol{W}_i^e \times \boldsymbol{H} \cdot \mathbf{n} \rho dl = -\frac{jk_0\eta_0}{2\pi} \int_C \hat{e}_\rho \cdot \boldsymbol{W}_i^e dl \tag{5}$$

To facilitate the implementation of the method, stiffness matrix K_{ij}^e is derived analytically in appendix II. With a connectivity matrix *B* defined for the assembly of globe system equation, as

$$K_{ij}^{e} \to K\left(B(e,i), B(e,j)\right) \tag{6}$$

Then

$$[K][E] = [b] \tag{7}$$

After solving (7), electric fields in the cross section shown in Fig. 3 can be obtained.

Note that the total radiation power (TRP) is exactly the same as the dissipated energy in the PML regions 6-8. Similarly, the absorbed power by the coating layer is the dissipated energy in region 2 in Fig. 3.

Based on the definition of electric and magnetic energy density, the dissipated energy in each triangle is the real part of the energy, shown as

$$\begin{aligned} P^{e} &= \mathrm{Re}\left\{ j\omega\pi \int_{\Delta_e} \left[\mu_0 \boldsymbol{H}^{*} \cdot \mu_r \overline{\overline{\Lambda}} \boldsymbol{H} - \varepsilon_0 \boldsymbol{E}^{*} \cdot \varepsilon_r \overline{\overline{\Lambda}} \boldsymbol{E} \right] \rho d\rho dz \right\} \\ &= \frac{j\pi}{k_0 \eta_0} \begin{bmatrix} E_1^{e} & E_2^{e} & E_3^{e} \end{bmatrix}^{*} D \begin{bmatrix} E_1^{e} \\ E_2^{e} \\ E_3^{e} \end{bmatrix} \end{aligned} \tag{8}$$

where

$$D_{ij\_rad} = \int_{S_e} \left(\nabla \times \boldsymbol{W}_i^{e} \cdot \left[\mu_r \overline{\overline{\Lambda}} \right]^{-1} \cdot \nabla \times \boldsymbol{W}_j^{e} - k_0^2 \varepsilon_r \boldsymbol{W}_i^{e} \cdot \overline{\overline{\Lambda}} \cdot \boldsymbol{W}_j^{e} \right) \rho dS_e \tag{9}$$

which can be easily calculated analytically by the formula derived in Appendix II. Then the total radiated power and the absorbed power are the summation of dissipated energy of each triangle in the corresponding regions

$$P_{rad} = \mathrm{Re}\left\{ \sum_{elements \in \mathrm{PML}} P^{e} \right\} \tag{10}$$

$$P_{abs} = \mathrm{Re}\left\{ \sum_{elements \in \mathrm{Region2}} P^{e} \right\} \tag{11}$$

3 2D FEM VERIFICATION

The developed 2D FEM was used to estimate the radiation reduction from a cable carrying a common mode current, when absorbing sheet materials or a ferrite choke was applied on it. The total power from source consists of power absorbed by the absorbing materials, the mismatch loss at the port, and the radiated power, shown as

$$P_f = P_{rad} + P_{mis} + P_{abs} \tag{12}$$

where P_f is the total power input into the system; P_{abs} is the power absorbed by the absorbing materials; P_{mis} is the power reflected at the port; and P_{rad} is the power radiated from the structure. With absorbing materials on the cable, the radiated power is related to the mismatch loss and absorbed power,

$$\frac{P_{rad\_abs\_cable}}{P_f} = 1 - \left|\Gamma^m\right|^2 - \frac{P_{abs}}{P_f} \tag{13}$$

and

$$\left|\Gamma_m\right|^2 = \left|\frac{Z_{cable}^{material} - Z_0}{Z_{cable}^{material} + Z_0}\right|^2 \tag{14}$$

is the calculated reflection coefficient of the cable coated by the absorbing material. In the case of the cable without coating, the total radiated power can be obtained as

$$\frac{P_{rad\_bare\_cable}}{P_f} = 1 - \left|\Gamma^c\right|^2 \tag{15}$$

and

$$\left|\Gamma_c\right|^2 = \left|\frac{Z_{cable} - Z_0}{Z_{cable} + Z_0}\right|^2 \tag{16}$$

is the reflection coefficient for a bare cable without any coatings. $Z_{cable}^{material}$ and Z_{cable} are

the input impedances when the cable is coated with and without the absorbing materials. Therefore, input impedance and radiated power reduction were used to analyze the EMI suppression when absorbing materials were applied to cables. Radiated power reduction (TRP reduction) can be obtained by substituting (13) and (15) into (17).

$$TRP \text{ Reduction} = \frac{P_{rad\_abs\_cable}}{P_{rad\_bare\_cable}} \tag{17}$$

The 2D FEM simulation results are compared with the CST Microwave Studio results for a 1 m cable with 3/8 in diameter and fully coated with 0.25 mm absorbing material. The frequency dependence of the magnitude of the input impedance is shown in Fig. 4 (a), and the radiated power reduction by the absorbing material is depicted in Fig. 4 (b). The comparison indicates that the 2D FEM can achieve similar results as those obtained by the 3D full-wave solvers. The main advantage of the 2D FEM solver is that it is much more efficient from the point of CPU time and memory consumption because it uses less unknowns on a 2D cross section as compared to 3D solvers with volume meshes.

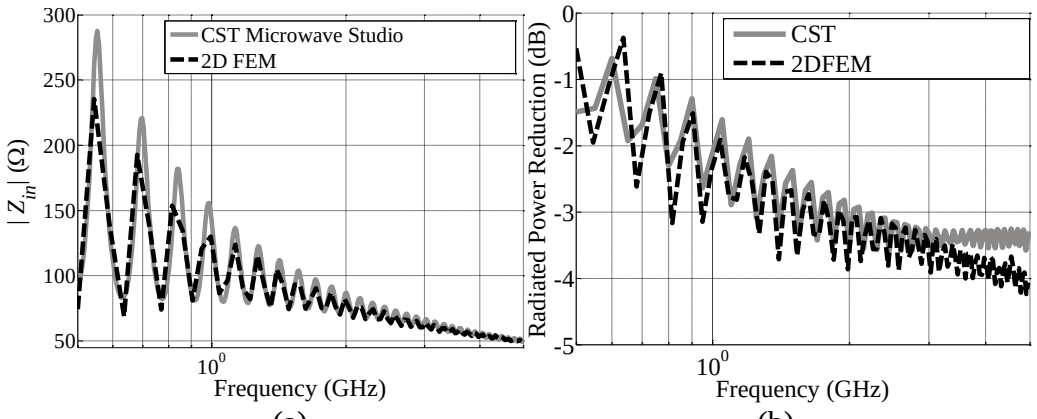

(a) (b)

Fig. 4. Comparison between the 2D FEM and CST Microwave Studio. (a) Input impedance magnitude, (b) radiated power reduction.

Measurements of input impedance in an anechoic chamber were also performed to validate the 2D FEM formulation. The input impedance values of a monopole antenna coated with the absorbing material and the same antenna, but with a ferrite choke, were measured. The measurement set-up is shown in Fig. 5. The length of the monopole antenna was 915 mm, the length of the absorbing material coating was 915 mm, and its thickness was 0.15 mm. The length of the ferrite hollow cylindrical choke placed on the antenna rod was 30 mm, and the thickness of the ferrite core was 3.72 mm. The geometry parameters are shown in Fig. 6.

2D FEM can be used to evaluate the EMI reduction when a specific material is applied to a cable, if its permittivity and permeability are known, as shown in Fig. 7, for example, measured using the NWR technique [16]. “High frequency (HF) ferrite” is a ferrite core with working frequency up to hundreds of MHz. “Absorbing sheet material” is a flexible, absorbing magnetic material with working frequency approximately from 1 to 5 GHz. “High frequency (HF) absorbing sheet material” is a flexible absorbing magnetic material with working frequency approximately above 5 GHz. HF ferrite was applied to the cable, and the measured input impedance was compared with simulation results in Fig. 8 (a). The results are compared in Fig. 8 (b) with the absorbing sheet material applied to the cable. The ferrite core and sheet absorbing material were from Laird Technology. There is a bigger difference between the measurement and simulation results by 2D FEM at higher frequencies. A probable reason of discrepancy is related to the fact that the coating condition of the material on the actual cable is not exactly the same as in 2D FEM. Another possible reason is that the permittivity measured by the NRW technique may not be accurate enough, since the material contains conducting ferromagnetic particles, and the

composite has high real permittivity and dielectric loss. In such materials, the gap between the washer and the center conductor of the coaxial air-line might affect the accuracy of dielectric measurements; it is very difficult to control the size of such a gap to introduce the proper gap correction [17-18].

(a) (b) (c)

Fig. 5. Measurement set-up. (a) The bare monopole antenna rod, (b) monopole with a ferrite core, (c) monopole antenna coated with a magneto-dielectric absorbing material.

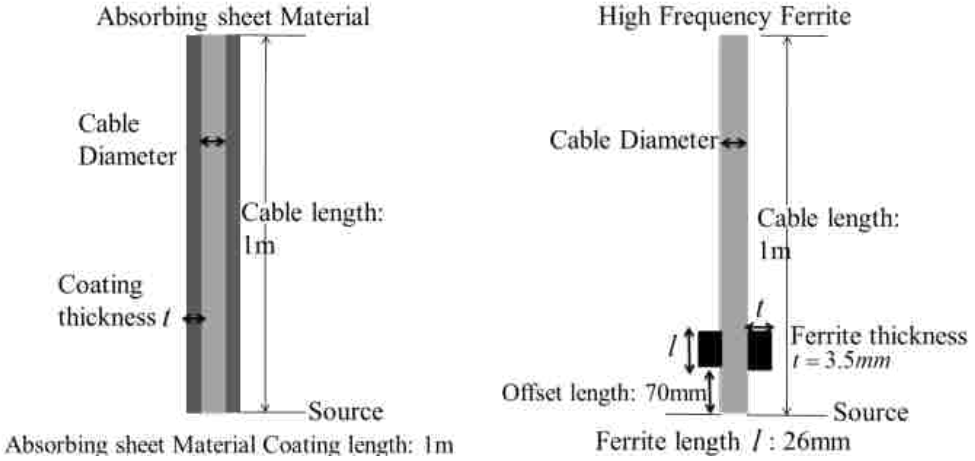

(a) (b)

Fig. 6. A monopole antenna diagram imitating a cable with absorbing materials. (a) Monopole fully coated with an absorbing sheet material, (b) monopole with the ferrite choke.

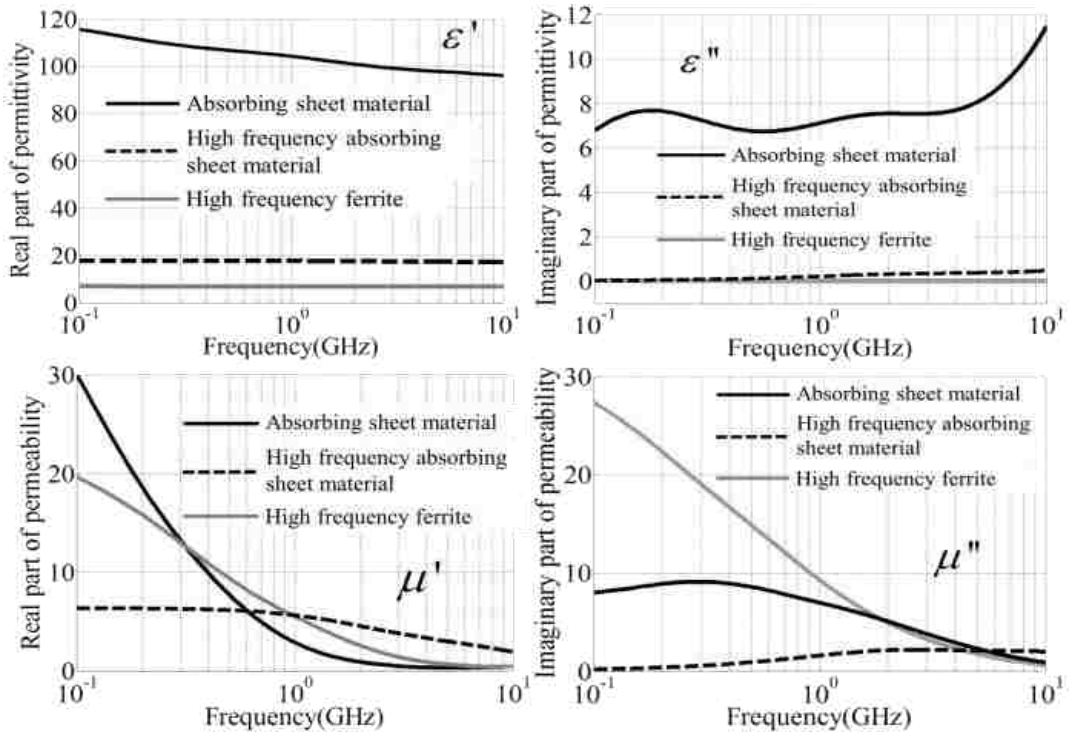

Fig. 7. Material parameters for the ferrite core and absorbing sheet materials.

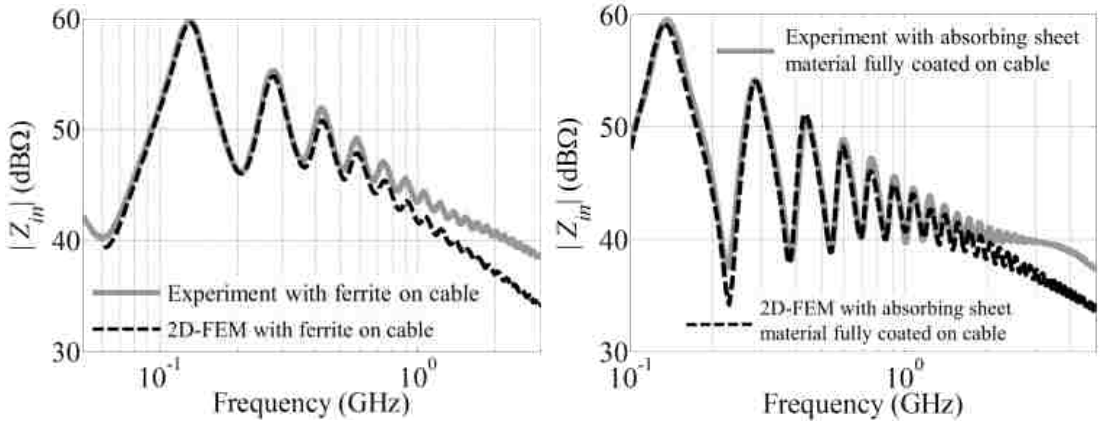

(a) (b)

Fig. 8. Input impedance comparison between the 2D FEM and measurement results. (a) With ferrite core on the cable, (b) with absorbing sheet material on the cable.

4 CABLE APPLICATION OF ABSORBING MATERIALS

With the developed 2D FEM, the EMI reduction from a cable with absorbing sheet materials or a ferrite core was evaluated over several typical scenarios to give insightful guidelines for suppressing EMI from cables with absorbing materials.

In this section, radiation power reduction from the cable was evaluated over different materials in the frequency range of 0.2 GHz to 10 GHz. The material parameters of three evaluated materials are shown in Fig. 7. The HF ferrite was set 80 mm away from the source of the cable. As shown in Table 1, the length was 30 mm, the thickness was 4.255 mm, and the air gap between the inner portion of the ferrite core and the cable was 0.3175 mm. The absorbing sheet material and HF absorbing sheet material were coated tightly on the cable, the length of the sheet material was the same as the cable length, which was 1 or 2 m, and the thicknesses were 0.25 mm and 0.5 mm. Three cable diameters were studied: 1/8 in is similar to the diameter of a USB cable, 3/8 in is similar to the diameter of a HDMI cable, and 5/8 in is close to the diameter of a power cable. Source impedance was 50 Ω, and the radiated power and input impedance were compared to the cases with 10 Ω and 25 Ω source impedance in the last subsection.

Table I. Dimensions of Absorber Materials and a Ferrite Core Used in 2D FEM Simulation Model

Absorbing materials	HF Ferrite	Absorbing sheet Material/ HF Absorbing sheet Material
Cable length	1000 mm, 2000 mm	
Cable Diameters	1/8 inch, 3/8 inch, 5/8 inch	
Absorbing length	30 mm	1000 mm, 2000 mm
Absorber Thickness	4.255 mm	0.25 mm, 0.5 mm
Absorber offset	80 mm	0 mm
Air Gap Thickness	0.3175 mm	0 mm

4.1 **Comparison of Different Absorbing Materials and a Ferrite Core**

The radiated power reduction from the cable was evaluated over three different materials, and the material parameters are shown in Fig. 7. Cable diameter was 3/8 in, cable length was 1 m, and source impedance was 50 Ω. The dimension of the ferrite core is shown in Table 1, and the thicknesses of sheet materials were 0.25 mm and 0.5 mm.

Because of standing waves along the monopole antenna mimicking the cable and related to the length of antenna, there are resonances of input impedance. As shown in Fig. 9, the resonant frequencies of input impedance shift and the magnitude varies when absorbing materials are applied to cables; therefore, the mismatch loss increases at some frequencies, particularly at the resonances where radiation dominates. At higher frequencies, the resonance in impedance is not obvious with absorbing sheet materials because the absorption contributes significantly to EMI reduction. Resonances were also observed in radiated power reduction as shown in Fig. 10 (a) for the same reasons. Since the resonances are the nature of the standing waves along the cable, averaged radiated power reduction is proposed to evaluate the EMI performance, as shown in Fig. 10 (b). The

averaged value in Fig. 10 (b) is calculated from the upper and lower bound of the original radiated power reduction values with resonances, as shown in Fig. 10 (a). Averaged radiated power reduction from three materials (with the material parameters shown in Fig. 7) is compared in Fig. 10 (b). For the suppression of the EMI, the HF ferrite core is effective below 500 MHz where EMI decreased approximately 2 to 4 dB. The absorbing sheet material is effective in the whole frequency range from 200 MHz to 10 GHz, where EMI decreased approximately 4 to 6 dB with a 0.25 mm thick absorber. The HF absorbing sheet material is effective above 2 GHz, where EMI decreased approximately 4 to 7 dB with a 0.25 mm thick absorber. The EMI reduction increases approximately 2 dB when the thickness of the sheet materials increases from 0.25 mm to 0.5 mm in the effective frequency range. Therefore, the ferrite core brings in 3 to 5 dB EMI reduction in the MHz range. With absorbing sheet material fully coated on the cable, EMI can be reduced 3 to 9 dB in a broadband frequency range from several MHz to GHz. At several GHz, the HF absorbing sheet material with 0.25 to 0.5 mm thick could bring in 5 to 9 dB radiation reduction from cables.

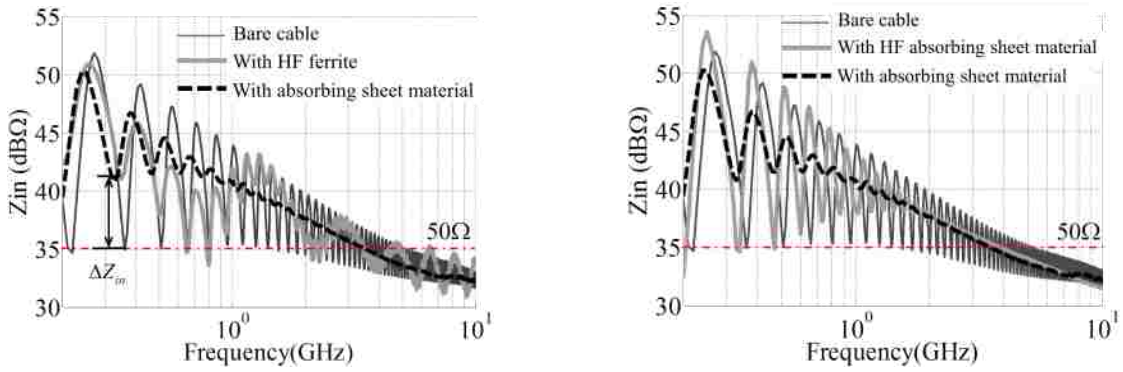

Fig. 9. Input impedance comparison. (a) Bare cable compared to cables with HF ferrite and absorbing sheet material, (b) bare cable compared to cables with absorbing sheet material and HF absorbing sheet material.

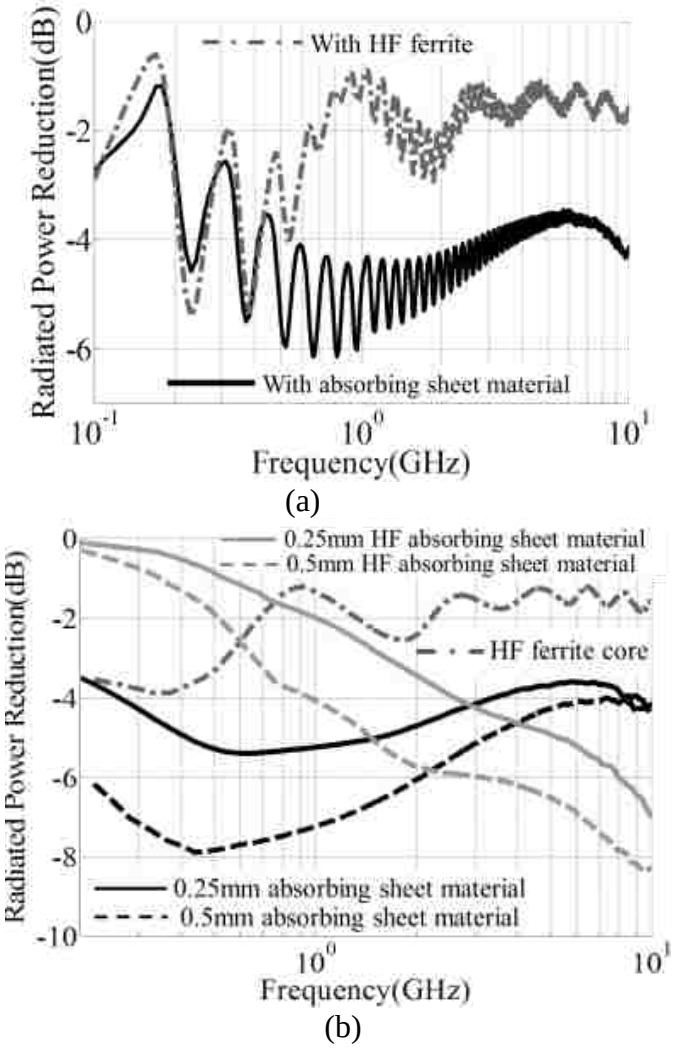

Fig. 10. Radiated power reduction comparison. (a) Radiated power reduction of cables with a HF ferrite core and absorbing sheet material with 0.25 mm thickness, (b) averaged radiated power reduction of ferrite core and different absorbing sheet materials.

4.2 **Comparison with Different Cable Diameters**

Cables with different diameters were considered because of different cable applications. Source impedance was 50 Ω, and the dielectric constant at waveguide port was 2.1. Cable length was 1 m. Radiated power reduction with 0.25 mm thick absorbing sheet material is compared in Fig. 11 (a). The radiated power reduction decreased as the

diameter of the cable increased until 3 GHz. This is because the absorbed power is larger when the cable diameter is smaller, as shown in Fig. 12 (a). The same conclusion can be drawn when the ferrite core was applied to the cables. The dimension of the ferrite core is shown in Table 1, and the radiated power reduction is compared in Fig. 11 (b), the absorbed power is compared in Fig. 12 (b).

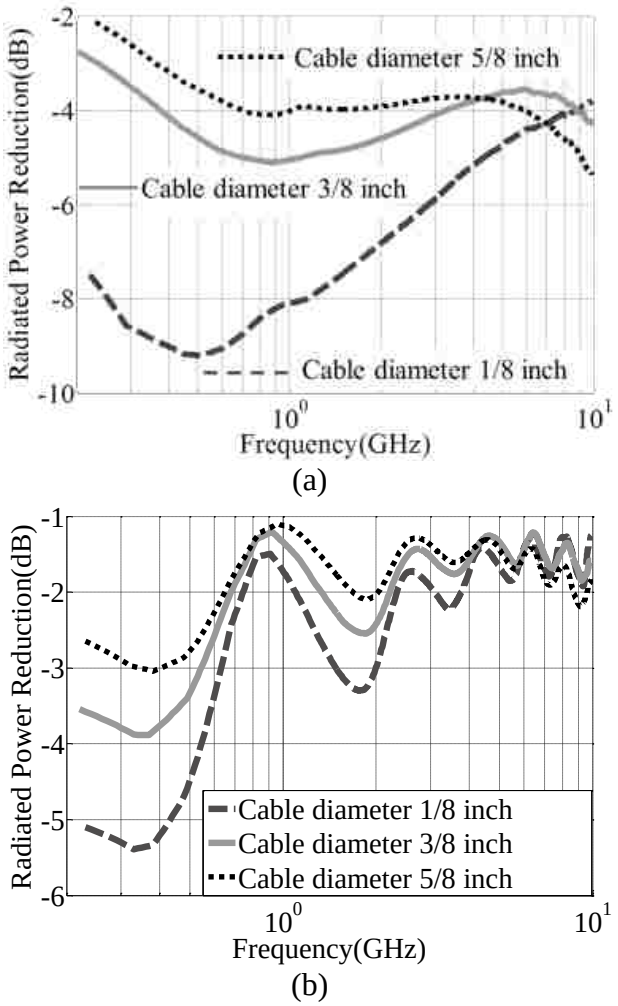

Fig. 11. Averaged radiated power reduction comparison with different cable diameters. (a) Cables with 0.25 mm thick absorbing sheet material, (b) cables with ferrite.

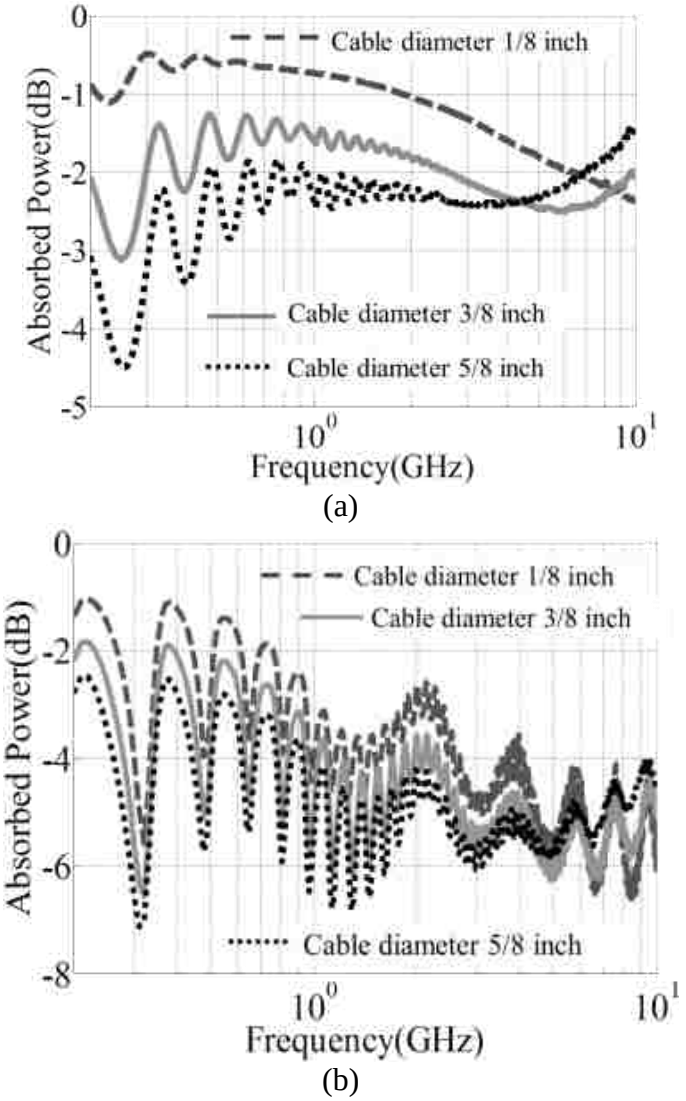

Fig. 12. Absorbed power comparison with different cable diameters. (a) Cables with 0.25 mm thick absorbing sheet material, (b) cables with ferrite.

4.3 **Comparison with Different Cable Lengths**

Cables causing EMI problems in reality might have different lengths. Absorbing materials on cables with 1 m and 2 m length were analyzed. Cable diameter was 3/8 in. Without absorbing material, the radiation from a bare cable is almost the same for 1 m and 2 m length cables, as shown in Fig. 13, and the resonant frequencies were related to the

cable length. When the HF ferrite core with dimensions in Table 1 was on 1 m and 2 m cables, the radiated power reduction is almost the same, as shown in Fig. 14. With a 0.25 mm thick absorbing sheet material fully coated on 2 m cables, the radiated power reduction is larger than when it was coated on a 1 m cable below a couple GHz. This is because when the absorbing materials are fully coated on the cables, more power is absorbed with longer cables in the frequency range where the cable length is comparable to the wavelength, as shown in Fig. 15.

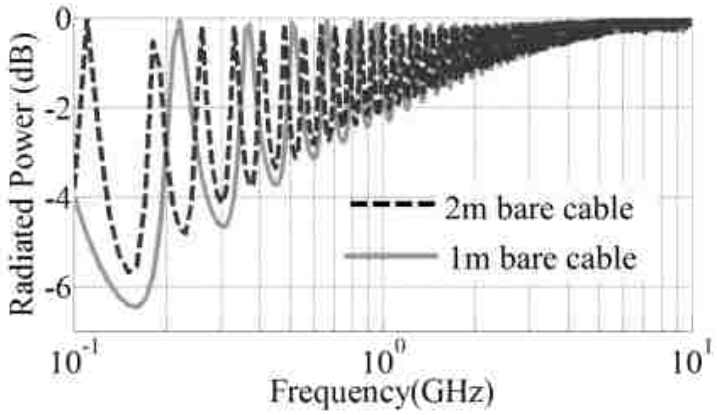

Fig. 13. Radiated power comparison of bare cables with different lengths.

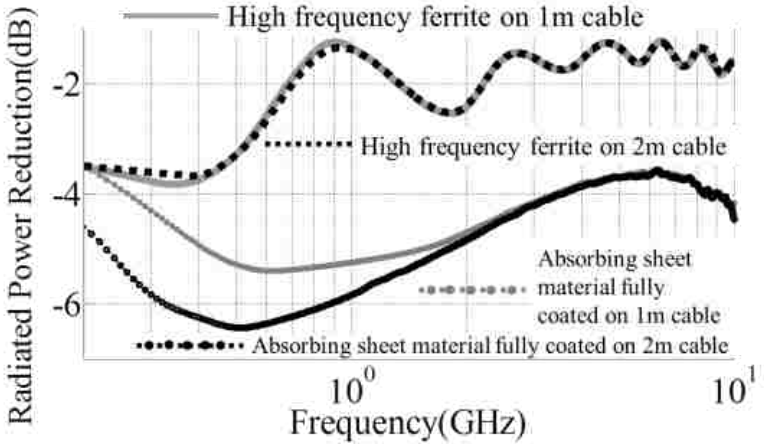

Fig. 14. Averaged radiated power reduction comparison of absorbing sheet material and HF ferrite core applied on the cables with different lengths.

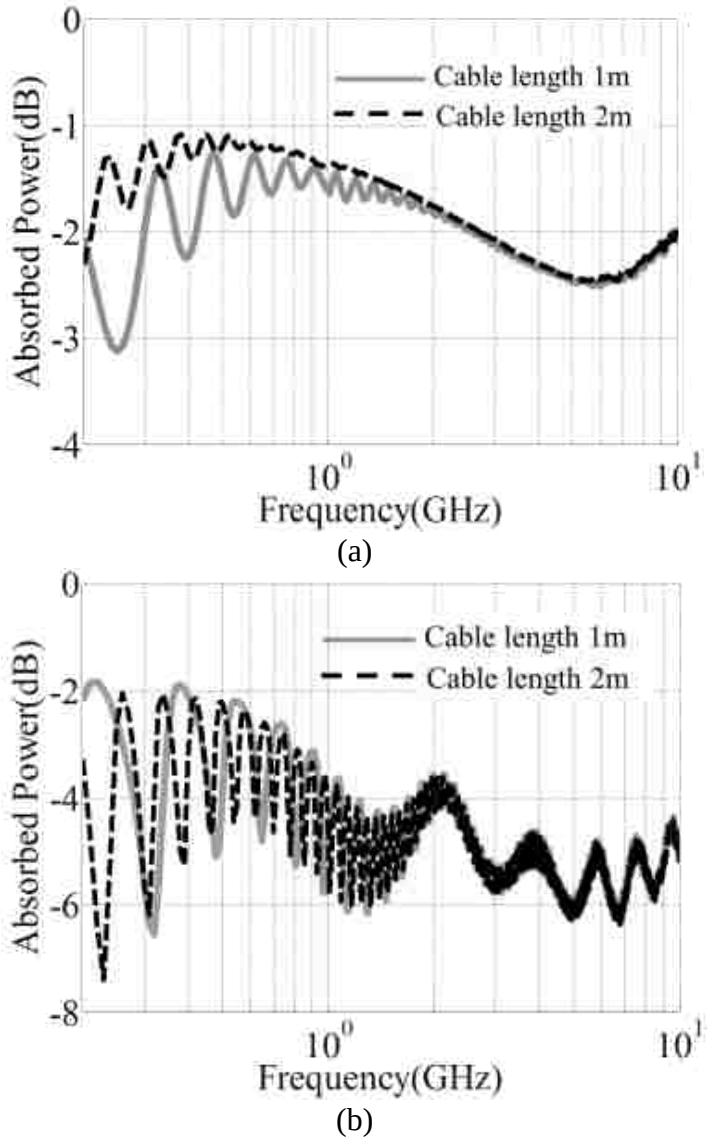

Fig. 15. Absorbed power comparison with different lengths. (a) Cables with 0.25 mm thick absorbing sheet material fully coated on the cables, (b) cables with ferrite.

4.4 **Comparison with Different Source Impedances**

Source impedance was set to 50 Ω in the previous analysis. However, in reality the noise source may be much lower than 50 Ω. 10 Ω source impedance was also studied. Cable length was 1 m and cable diameter was 3/8 in. The source impedance was changed through the dielectric constant of the coaxial connector connecting to the waveguide port.

Therefore, the input impedance of the structure did not change whether with absorbing materials on the cables or not, as shown in Fig. 16. Based on (14) and (16), the mismatch loss is different with different source impedances. With lower source impedance, the mismatch loss increased, as shown in Fig. 17 (a), because the input impedance is higher than 35 Ω, especially at low frequencies. With absorbing materials on the cables, the absorbed power decreased with a 10 Ω source impedance because of the larger mismatch between source impedance and input impedance. However, the decreased absorbed power was less than the increased reflected power, as shown in Fig. 17; so the radiated power was less than it was with 50 Ω source impedance, as the curves without markers show in Fig. 18. For the cable without absorbing materials, the radiated power decreased with 10 Ω source, due to the increased mismatch loss, as the curves with markers shown in Fig. 18. The radiated power reduction with different source impedances is compared in Fig. 19, and it illustrates that the difference of the average power reduction values is less than 1 dB, while the uncertainty caused by the resonances of the bare cable is different with different source impedances. When ferrite cores were applied on the cables, the same conclusion can be drawn as shown in Fig. 20.

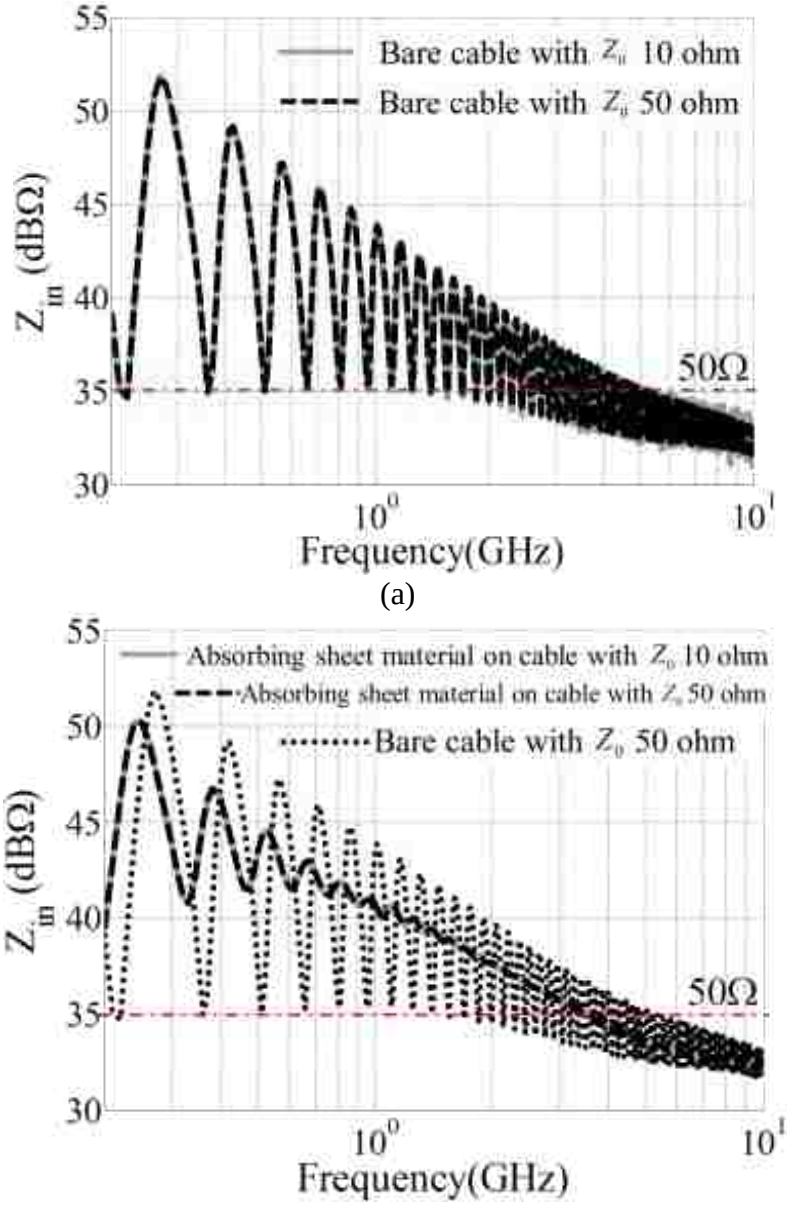

(a)

(b)

Fig. 16. Input impedance comparison with different source impedances (10 Ω and 50 Ω). (a) Bare cables, (b) cables with 0.25 mm thick absorbing sheet material.

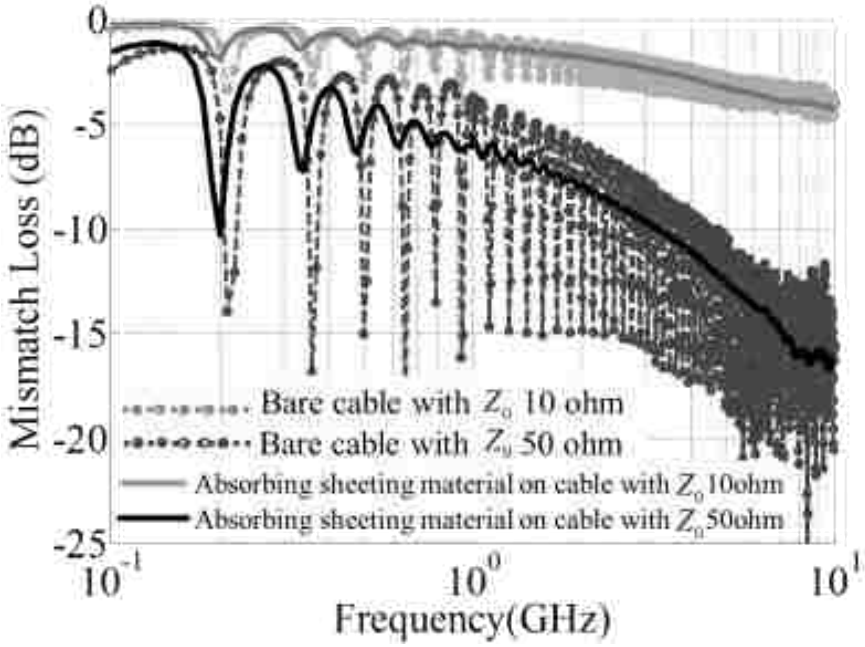

(a)

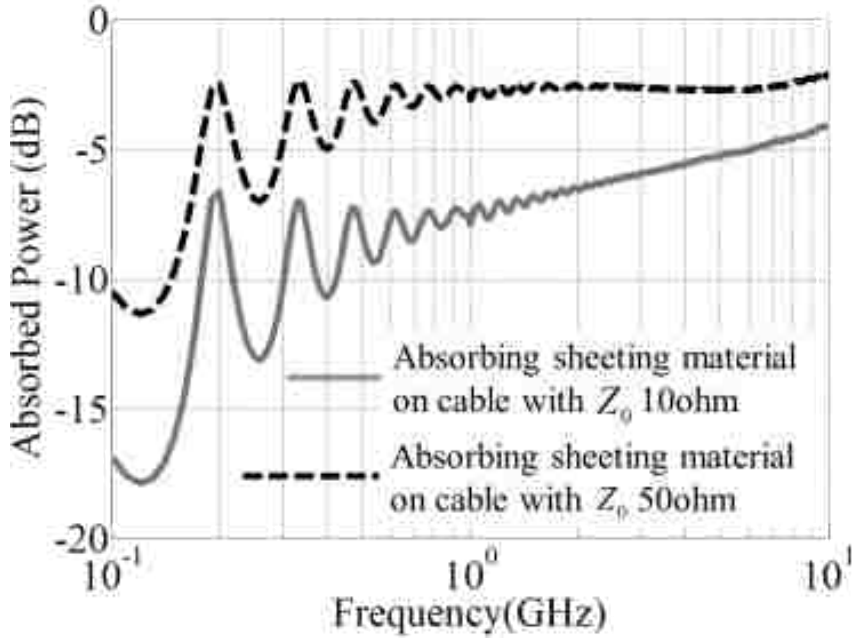

(b)

Fig. 17. Power comparison with different source impedances (10 Ω and 50 Ω). (a) Mismatch loss (reflected power) for bare cables and cables with absorbing sheet material, (b) absorbed power for cables with absorbing sheet material.

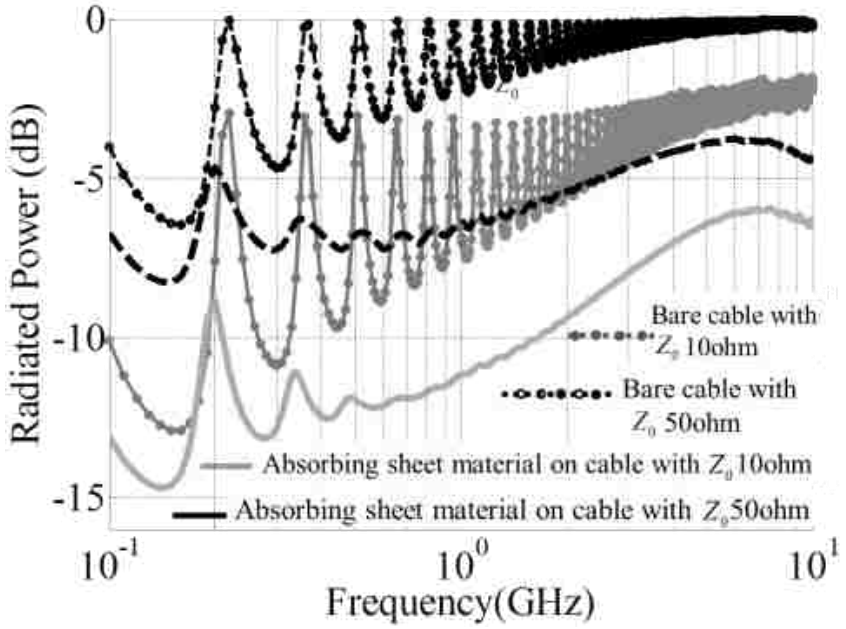

Fig. 18. Radiated power comparison with different source impedances (10 Ω and 50 Ω) for bare cables and cables with absorbing sheet material.

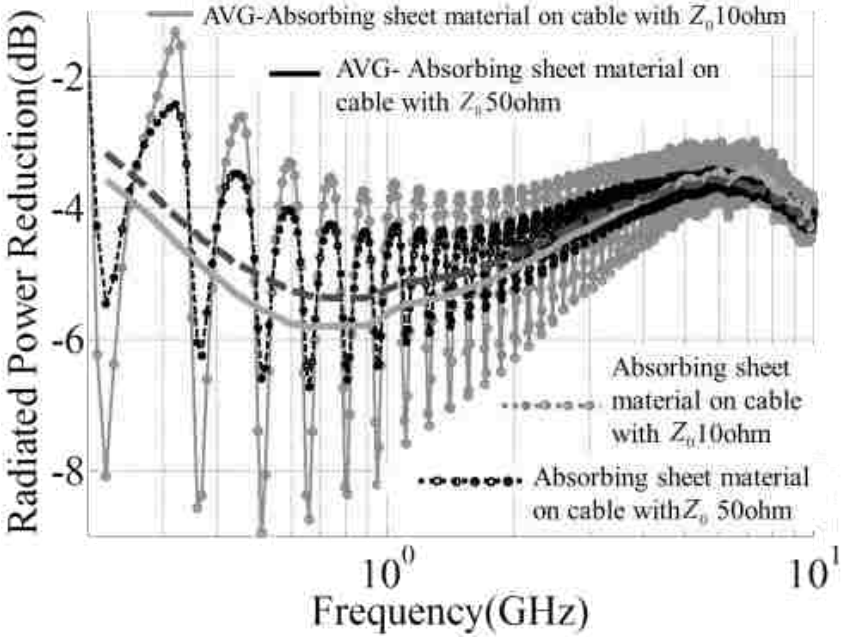

Fig. 19. Radiated power reduction comparison with different source impedances (10 Ω and 50 Ω) for cables with absorbing sheet material.

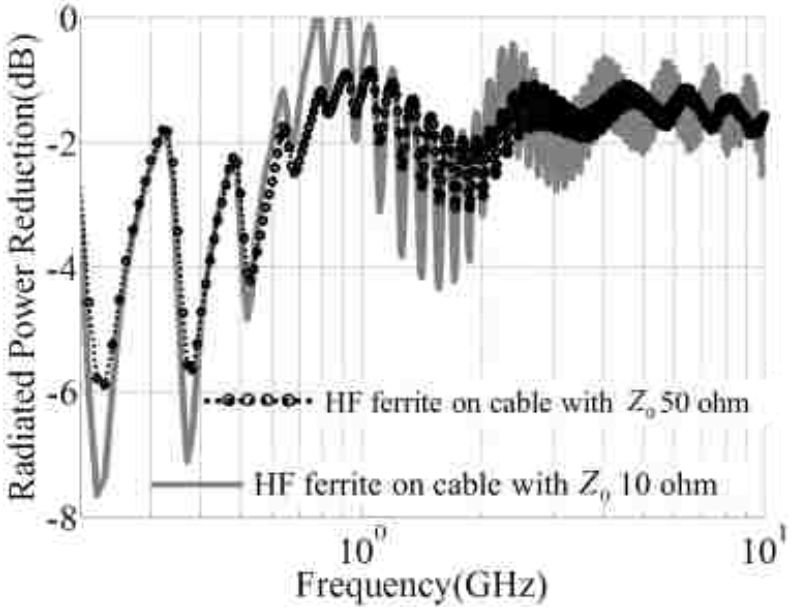

(a)

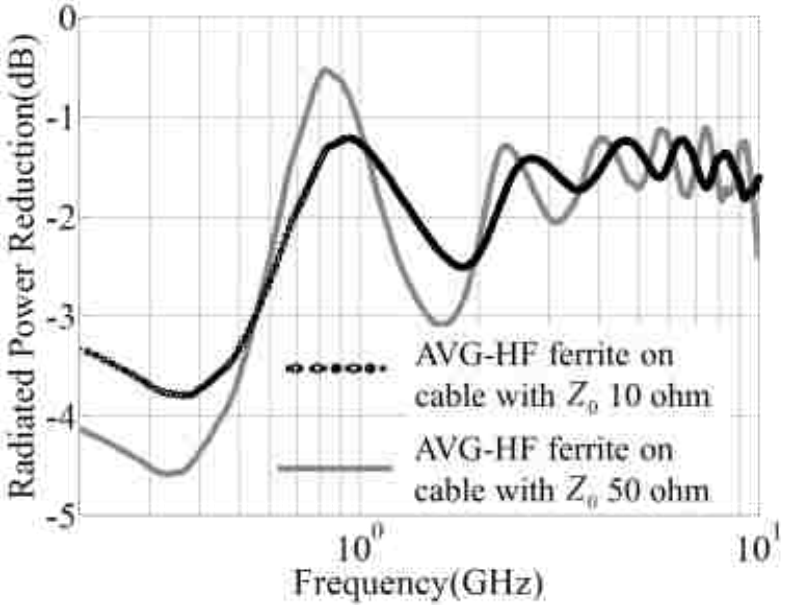

(b)

Fig. 20. Radiated power reduction comparison with different source impedances (10 Ω and 50 Ω) for cables with the ferrite core. (a) Radiated power reduction, (b) averaged radiated power reduction.

5 CONCLUSIONS

To model the axially symmetric 3D structures with less time and memory consumption, an edge-based 2D FEM formulation was derived to evaluate EMI suppression with the absorbing materials applied to cables. Input impedance was calculated from the electric field at the waveguide port to analyze the reflected power, and the radiated power was calculated from the electric field in the PML layers to quantify the radiation from the structure. Both the input impedance and the EMI reduction on cables coated with absorbing materials calculated by the 2D FEM were compared with commercial simulation software, and the input impedance from 2D FEM was compared with the experiment results. With the developed 2D FEM, the EMI reduction of different absorbing materials applied to cables was evaluated. To suppress EMI from cables in the MHz range, a ferrite core is a convenient choice for 3 to 5 dB reduction. For a broadband EMI suppression from several MHz to GHz frequency range, 3 to 9 dB radiated power reduction could be achieved with absorbing sheet material fully coated on the cable. In the frequency range above several GHz, the absorbing sheet material with high permeability in high frequency could bring in 5 to 9 dB radiation reduction from cables. The thickness of absorbing sheet material was chosen to be 0.25 mm and 0.5 mm. For cables with different diameters, the smaller the diameter, the EMI reduction was larger with ferrite core or absorbing materials below several GHz. For the cable with different lengths, EMI reduction was almost the same with the same dimension ferrite cores. With absorbing materials fully coated on the cables with different lengths, the longer cable radiated less at low frequency. Different source impedances brought in different mismatch losses in the cable radiation structure, whether with or without absorbing materials. The difference of

the average radiated power reduction with different source impedance was less than 1 dB when the cable was coated with absorbing sheet material or ferrite cores, while the uncertainty of the radiated power reduction caused by the resonances of the bare cable was different with different source impedances.

APPENDIX I

Edge element basis W_i^e is defined as [15],

$$\mathbf{W}_i^e = \left(L_i \nabla L_{i+1} - L_{i+1} \nabla L_i\right) l_i, \quad L_i = \frac{\Delta_i(\rho, z)}{\Delta} \tag{18}$$

where $i = 1, 2, 3$, L_i is the basis function for nodal element, and Δ is the area of triangle/element *e*, as shown in Fig. 21.

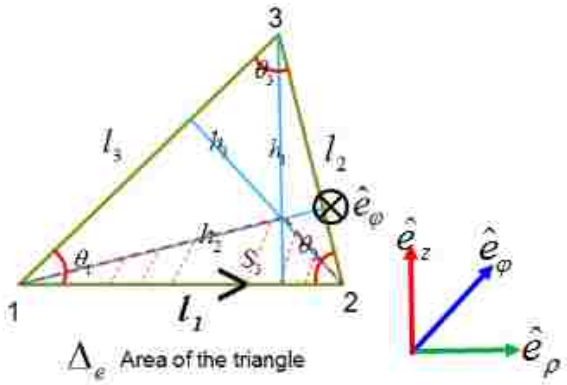

Fig. 21. Triangle element for edge elements in cylindrical system.

The vector basis function has following properties: W_i^e has a constant tangential component along edge *i*, but no tangential component along edge $i+1$ and edge $i+2$. Also, it has the relationship as shown in (19), (20).

$$\nabla \cdot (L_1 \nabla L_2 - L_2 \nabla L_1) = 0 \tag{19}$$

$$\nabla \times (L_i \nabla L_{i+1} - L_{i+1} \nabla L_i) = 2 \nabla L_i \times \nabla L_{i+1} \tag{20}$$

APPENDIX II

Stiffness matrix K_{ij}^{e} was derived as follows.

First, substitute $\bar{\bar{\Lambda}}$ into (4) to get:

$$\begin{aligned} K_{ij}^{e} &= \int_{Se} \left\{ (\nabla \times \mathbf{W}_i^e \cdot \nabla \times \mathbf{W}_j^e) \mu_r^{-1} \Lambda_{\varphi\varphi}^{-1} \right\} \rho d\rho dz \\ &- \int_{Se} \left\{ k_0^2 \varepsilon_r \mathbf{W}_i^e \cdot [\Lambda_{\rho\rho} \hat{e}_\rho \hat{e}_\rho + \Lambda_{zz} \hat{e}_z \hat{e}_z] \cdot \mathbf{W}_j^e \right\} \rho d\rho dz \end{aligned} \tag{21}$$

With the properties of edge element basis W_i^e (appendix I), (22) was obtained:

$$\nabla \times \boldsymbol{W}_i^e = 2 l_i \left(\nabla L_i \times \nabla L_{i+1} \right) = -l_i \frac{\hat{e}_\varphi}{\Delta_e} \tag{22}$$

where l_i was the length of the triangle edge as shown in Fig. 21 and defined in (23). $\boldsymbol{\Delta_e}$ was the area of a triangle element, as shown in Fig. 21.

$$\vec{l}_1 = \vec{r}_2 - \vec{r}_1 \ , \ \vec{l}_2 = \vec{r}_3 - \vec{r}_2 \ , \ \vec{l}_3 = \vec{r}_1 - \vec{r}_3 \tag{23}$$

Then, the first term in (20) was derived:

$$\int_{Se} \left\{ (\nabla \times \mathbf{W}_i^e \cdot \nabla \times \mathbf{W}_j^e) \mu_r^{-1} \Lambda_{\varphi\varphi}^{-1} \right\} \rho d\rho dz = \frac{l_i l_j (\rho_1 + \rho_2 + \rho_3)}{3\Delta_e} u_r^{-1} \Lambda_{\varphi\varphi}^{-1} \tag{24}$$

With (18) and (25), (26) was obtained.

$$\nabla L_i = \frac{h_{i+1}}{h_{i+1}} = \frac{\hat{l}_{i+1} \times \hat{e}_\varphi l_{i+1}}{h_{i+1} l_{i+1}} = \frac{\boldsymbol{l}_{i+1} \times \hat{e}_\varphi}{2\Delta_e} \tag{25}$$

$$\boldsymbol{W}_i^e \cdot \hat{e}_\rho = \frac{l_i}{2\Delta_e} \left[L_i \boldsymbol{l}_{i+2} - L_{i+1} \boldsymbol{l}_{i+1} \right] \cdot \left(-\hat{e}_z \right) \tag{26}$$

where h_i was the distance from edge *i* to the node it is facing in each triangle element, as shown in Fig. 21.

With (26) and (27), the second term in (21) was formulated as in (28).

$$\alpha_i = -\vec{l}_i \cdot \hat{e}_z = -\left(z_{i+1} - z_i\right), \beta_i = \vec{l}_i \cdot \hat{e}_\rho = \rho_{i+1} - \rho_i \tag{27}$$

$$\begin{aligned}
&\int_{Se} \left\{ k_0^2 \varepsilon_r \mathbf{W}_i^e \cdot [\Lambda_{\rho\rho} \hat{e}_\rho \hat{e}_\rho + \Lambda_{zz} \hat{e}_z \hat{e}_z] \cdot \mathbf{W}_j^e \right\} \rho d\rho dz \\
&= k_0^2 \varepsilon_r \frac{l_i l_j}{4\left(\Delta^e\right)^2} \begin{pmatrix} \alpha_{i+2} & -\alpha_{i+1} \end{pmatrix} \begin{pmatrix} \int_{Se} L_i L_j \rho ds_e & \int_{Se} L_i L_{j+1} \rho ds_e \\ \int_{Se} L_{i+1} L_j \rho ds_e & \int_{Se} L_{i+1} L_{j+1} \rho ds_e \end{pmatrix} \begin{pmatrix} \alpha_{j+2} \\ -\alpha_{j+2} \end{pmatrix} \\
&+ k_0^2 \varepsilon_r \frac{l_i l_j}{4\left(\Delta^e\right)^2} \begin{pmatrix} \beta_{i+2} & -\beta_{i+1} \end{pmatrix} \begin{pmatrix} \int_{Se} L_i L_j \rho ds_e & \int_{Se} L_i L_{j+1} \rho ds_e \\ \int_{Se} L_{i+1} L_j \rho ds_e & \int_{Se} L_{i+1} L_{j+1} \rho ds_e \end{pmatrix} \begin{pmatrix} \beta_{j+2} \\ -\beta_{j+2} \end{pmatrix}
\end{aligned} \tag{28}$$

The integral in (28) can be calculated analytically with the coordinates of each node of the triangle element. With (24) and (28), stiffness matrix K_{ij}^e was implemented with Matlab.

REFERENCES

[1] Fujio Amemiya,; Takagi, K.; Mori, Toshinori; Kuwabara, N.; Hamada, S.; Iwamoto, Y., "Investigation of emission reduction effect from interface cables using amorphous magnetic-alloy film," IEEE International Symposium on Electromagnetic Compatibility, vol.1, pp.155,160 vol.1, 19-23 Aug. 2002.
[2] J. Nadolny, "Correlation between measured and simulated parameters of a proposed transfer standard," in EMUEMC Metrology Challenges for Industry, A Workshop on Measurements, Standards, Calibration and Accreditation, NIST, Boulder, CO, Jan. 1995.
[3] Tavzarashvili, K.N., Ghvedashvili, G.N., Kakulia, D.G., Karkashadze, D.D., Zaridze, R.S., "The method of auxiliary sources and eigen-function series representation for modeling of the open cable radiation problem," proceedings of the 9th International Seminar/Workshop on Direct and Inverse Problems of Electromagnetic and Acoustic Wave Theory, pp.73,76, 11-14 Oct. 2004.
[4] Harms, P.; Mittra, R.; Nadolny, J., "Simulating measurements for a cable radiation study," IEEE Transactions on Electromagnetic Compatibility, vol.38, no.1, pp.25,30, Feb 1996.
[5] D.J. Williams, C.J. Railton, D.J. Edwards, "A mathematical model of concentrically loaded coaxial structures and its EMC applications," 17th International Conference on Electromag. Compat., York, UK, pp. 91-98, 28-31 Aug. 1990.
[6] Jianqing Wang; Fujiwara, O.; Sasabe, K., "A simple method for predicting common-mode radiation from a cable attached to a conducting enclosure," Microwave Conference, 2001 Asia-Pacific, vol.3, pp.1119,1122, 2001.
[7] Hockanson, D.M.; Drewniak, J.L.; Hubing, T.H.; Van Doren, T.P., "FDTD modeling of common-mode radiation from cables," IEEE Transactions on Electromagnetic Compatibility, vol.38, no.3, pp.376,387, Aug 1996.
[8] T.A. Jerse, "How to apply interconnect cables without creating electromagnetic interference problems", Proc. IEEE Conf. Southeastcon-1997, 'Engineering New Century', Apr. 12-14, 1997, p. 347.
[9] P. Delogne, "Leaky Feeders and Subsurface Radio Communications," Peter Peregrinus Ltd. for the IEE, 1982.
[10] M.-S. Tong, A.Boriskin, R. Sauleau, and T.–G. Chang, "Study on wave propagation and boundary absorption performance using a body-of-revolution finite-difference time-domain (BOR-FDTD) method", Proc. 36th Eur. Microw. Conf., Sept 10-15, 2006, Manchester, UK, pp. 1327-1330.
[11] M.Y. Koledintseva, J.L. Drewniak, .J. Zhang, J. Lenn, and M. Thoms, "Modeling of ferrite-based materials for shielding enclosures", *Journal of Magnetism and Magnetic Materials*, vol. 321, pp. 730-733, March 2009.
[12] M.Y. Koledintseva, J. Wu, J. Zhang, J.L. Drewniak, and K.N. Rozanov, "Representation of permittivity for multiphase dielectric mixtures in FDTD modeling", *Proc. Int. IEEE Symp. Electromag. Compat.*, 9-13 Aug. 2004, Santa Clara, CA, vol. 1, pp.309-314.

[13] J. Xu, M. Y. Koledintseva, S. De, A. Radchenko, R. E. DuBroff, J.L. Drewniak, Y. He, and R. Johnson, "FDTD modeling of absorbing materials for EMI applications", 2010 Asia-Pacific International Symposium on Electromagnetic Compatibility, Beijing, China, Apr. 2010.
[14] M.Y. Koledintseva, J. Xu, S.De, J.L. Drewniak, Y. He, and R. Johnson, "Systematic analysis and engineering of absorbing materials containing magnetic inclusions for EMC applications", IEEE Trans. Magn., vol. 47, no. 2, Feb. 2011, pp. 317-323.
[15] J.-M. Jin, Finite Element Analysis of Antennas and Arrays, Wiley, 2009, Ch. 8 & 9.
[16] Jing Li, Yao-Jiang Zhang, Gafarov, A., De, S., Koledintseva, M.Y., Marchand, J., Hess, D., Durant, T., Nickerson, E., Drewniak, J.L., Jun Fan, "EMI reduction evaluation with flexible absorbing materials and ferrite cores applied on cables," 2012 IEEE International Symposium on Electromagnetic Compatibility (EMC), pp.646,651, Aug. 2012.
[17] Agilent Basics of Measuring the Dielectric Properties of Materials, Application Note 5989-2589EN, Agilent Technologies, Inc. 2005, 2006, available: http://www3.imperial.ac.uk/pls/portallive/docs/1/11949698.PDF.
[18] L.F. Chen, C.K. Ong, C.P. Neo, V.V. Varadan, and V.K. Varadan, Microwave Electronics – Measurement and Material Characterization, Wiley, 2004, chapter 4, pp. 182-184.

SECTION

2. CONCLUSION

In the first paper, the EMI physics of the optical cage connector was analyzed with full-wave simulation from 4GHz to 28GHZ. Below approximately 18GHz, the radiated power was caused by the currents on the ground pins in the connector structure. The partial U-channel ground conductor connection piece connecting the ground conductors adjacent to the differential signal pair conductors, reduced the radiation at half-wavelength resonances. Above 18GHz, the radiation from differential signals on the signal conductors was significant, and was related to the separation distance between the signal conductors, frequency, and conductor length. One approach for EMI mitigation of the coupling from the connector was an absorbing material partially covering the connector. Coupling paths of optical cage connector in the optical link was verified in simulation and measurement together with the optical cage and module enclosure.

In the second paper, the radiation from the high-speed connector with TL-mode current was analyzed in detail. The possible radiation mechanisms of a two-wire transmission line were analyzed with the Green's function method, the steepest decent method, and EMC studio (MoM). The radiation from a straight two-wire transmission line is due to the finite length, which brings in the four discontinuities at two ends of the wires. The increased radiated power from bent wires is because of the location change of the current discontinuities at the bends in reference to the straight wires, while the contribution from the small variance in the current distribution caused by the reflection at

bends can be neglected. Due to via transitions and discontinuities at two ends of the transmission line, the radiation contributed by mismatch effect was analyzed at harmonics of quarter-wavelengths. The steepest descent method revealed the radiation physics, and it is an efficient way to calculate radiation from two-wire transmission line with any type of current distribution, since it only sums up the radiated fields from the discontinuities in the structure. To suppress the radiation from antenna mode current and TL-mode current on the structure, EMI design guidelines for high-speed connectors were proposed, based on the analyzed radiation physics.

In the third paper, an edge-based 2D FEM formulation was derived to evaluate EMI suppression with the absorbing materials applied to cables. The radiated power was calculated from the electric field in the PML layers to quantify the radiation from the structure. The results from 2D FEM were compared with the results from 3D commercial simulation software. Design guidelines were proposed with the developed 2D FEM to evaluate the EMI reduction when absorbing materials applied to cables for EMI mitigation. The EMI reduction with different absorbing materials on cables, different cable diameters, different cable lengths, and different source impedances was evaluated from 0.1 to 10GHz.

VITA

Jing Li was born in Suzhou, Anhui Province, P. R. China. She received the Bachelor of Physics (2005) from Anhui Normal University, Wuhu, Anhui, P.R. China. In 2008, he received the Master of Science degree in Electrical Engineering in Beijing Jiaotong University. She then worked as an RF electrical verification engineer at Beijing Sony Ericsson Potevio Mobile Communications Co., Ltd in Beijing, China till 2010. She took a one-year internship at Cisco Systems, San Jose, CA, from 2012 to 2013. In August 2015, she received her Ph.D. in Electrical Engineering from Missouri University of Science and Technology.